KWANSEI GAKUIN UNIVERSITY

DOCTORAL THESIS

Theoretical Studies of Higher Order Topological States in Three-Dimensional Photonic Crystals

Author:
Huyen Thanh PHAN

Student ID: 67020202

Supervisor:
Katsunori WAKABAYASHI

A thesis submitted in fulfillment of the requirements for the degree of Doctor of Philosophy

in the

Department of Nanotechnology for Sustainable Energy
Graduate School of Science and Technology

August 7, 2023

Declaration of Authorship

I, Huyen Thanh PHAN, declare that this thesis titled, "Theoretical Studies of Higher Order Topological States in Three-Dimensional Photonic Crystals" and the work presented in it are my own. I confirm that:

- This work was done wholly or mainly while in candidature for a research degree at this University.
- Where any part of this thesis has previously been submitted for a degree or any other qualification at this University or any other institution, this has been clearly stated.
- Where I have consulted the published work of others, this is always clearly attributed.
- Where I have quoted from the work of others, the source is always given. With the exception of such quotations, this thesis is entirely my own work.
- I have acknowledged all main sources of help.
- Where the thesis is based on work done by myself jointly with others, I have made clear exactly what was done by others and what I have contributed myself.

Signed: _____

Date: _____

"It stands to the everlasting credit of science that by acting on the human mind it has overcome man's insecurity before himself and before nature."

Albert Einstein

KWANSEI GAKUIN UNIVERSITY

Abstract

Department of Nanotechnology for Sustainable Energy
Graduate School of Science and Technology

Doctor of Philosophy

Theoretical Studies of Higher Order Topological States in Three-Dimensional Photonic Crystals

by Huyen Thanh PHAN

The topological properties of photonic crystals (PhCs) have been experimentally realized in many photonic systems. To explain for these robust properties, topological invariants such as Chern number, Berry curvature are successfully theoretically determined for two-dimensional (2D) PhCs. Besides, Zak phase is also a good quantum number to explain for the existence of topological states in these systems. Zak phase is defined as one-dimensional (1D) integral of Berry connection over the first Brillouin zone (BZ). While in 1D systems, Zak phase is determined for each individual band, in 2D systems, it is determined for each in-plane direction.

In this thesis, we will numerically study the higher order topological states in PhC systems by calculating Zak phase for each systems. We start with a 2D PhC which exhibit topological edges and corner states. Then, we extend the study of topological PhCs to three-dimensional (3D) systems. The topological surface states are understood as the first order topology in 3D systems. To explain for these surface states, we generalize the notation of Zak phase to 3D systems then numerically calculate Zak phase for two types of 3D PhC structures. The structure with inversion symmetry has quantized Zak phase (0 or π value). On the other hand, the PhC without inversion symmetry will exhibit the winding of Zak phase in the first BZ. We will also examine the higher order topological states (the second order as hinge states) in these two PhCs. The numerical results of Zak phase can also be used to explain for these higher order topological states. Our description of Zak phase calculation in 3D systems is a priori not only restricted for photonic systems, but it is also applicable for other 3D systems.

Acknowledgements

First and foremost, I would like to send my sincere gratitude to my research supervisor Prof. Katsunori Wakabayashi for the continuous support of my research, for valuable discussions and helpful comments, and for his motivation and immense knowledge. His guidance helped me complete my thesis successfully.

Besides my supervisor, I am very grateful to all teachers and staffs in School of Science and Technology, Kwansei Gakuin University for enthusiastic education and insightful encouragement.

Last but not least, I also wish to appreciate useful suggestions and precious discussions with my colleagues.

Due to the limitation of time and knowledge, shortcomings and mistakes are inevitable. I would be hopeful for further advices and suggestions from teachers and colleagues.

Once again, I would like to express my sincerely thanks!

Huyen Thanh PHAN

Contents

Chapter 1

Introduction to Photonic Crystals

In this chapter, I will give a brief introduction to PhCs and the mathematical descriptions of PhCs. Then, I make a review of Maxwell's equations and how the electromagnetic (EM) waves propagate in periodic media. The photonic band structure and origin of photonic band gap will also be discussed in this chapter. At the end, I will explain about numerical methods usually used for evaluating properties of PhCs.

1.1 From Conventional Crystals to Photonic Crystals

A conventional unit cell is known as atoms or molecules are arranged periodically in a lattice [1, 2]. This arrangement causes periodic potential, which affect the transportation of electrons. For more detail, the periodic potential will cause band gaps in the energy band structure, where electrons with the energy at the gap region can not propagate into the crystals. Thinking in the same way as crystals act on electrons, the optical analog of conventional crystals are introduced as PhCs [3–5]. The periodicity in PhCs is the periodic arrangement of dielectric materials. This periodic dielectric "potential" will make photons behave in the same way as electrons do in the conventional crystals. It means that the energy band gap of photons is the result of periodic dielectric materials. According to the periodicity in real space, PhCs are divided into three types, which are one-, two-, and three-dimensional PhCs.

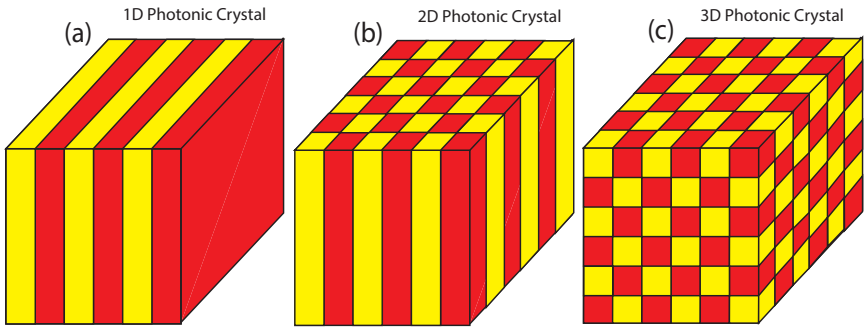

FIGURE 1.1: Schematic of three types of PhCs. (a) 1D PhC, which is periodic along one direction. (b) 2D PhC, which is periodic along two directions. (c) 3D PhC, which is periodic along three directions. Different colors indicate different dielectric materials.

Figure 1.1(a) is the schematic of 1D PhC, which is periodic along one direction. It is often known as multi-layer structures and was first time studied from hundred years ago [6]. These 1D PhCs have many applications such as reflecting mirror, and reflection waveguide. Most of the recent semiconductor lasers are also the applications of 1D PhCs. The schematic of 2D and 3D PhCs are shown in Fig. 1.1(b) and (c),

which is periodic along two and three directions, respectively. The serious studies of 2D and 3D PhCs are really occur in 1987, when people were caring about the localization of photons. A few years latter, following the experimental demonstration, a 3D PhC with complete band gap is successfully fabricated by Yablonovitch and his team [7].

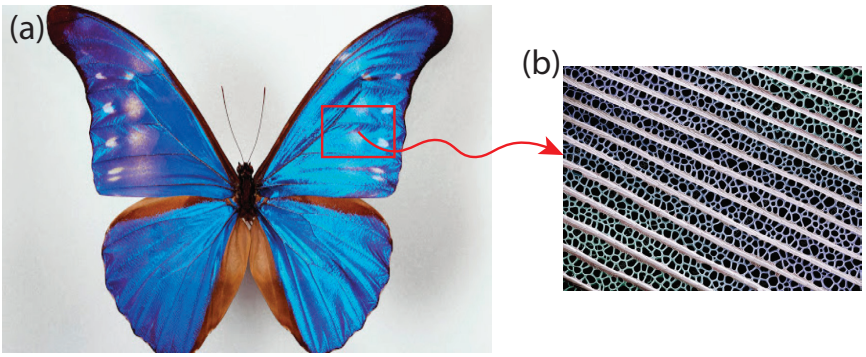

FIGURE 1.2: (a) Periodic micro structure of wings surface make color for a butterfly. (b) SEM image from a wing showing 1D PhC structure. (Source from: P. Vukusic, Phys. World (2015))

PhCs were firstly known as artificial materials. However, it is found that PhCs are already "fabricated" by nature. Figure 1.2 shows an image of a blue butterfly and SEM image of its wing surface. It is easy to realize the 1D PhC structure in the SEM image. The biological researches show that there is no pigment in the butterfly's wings. Therefore, the colors come from periodic micro structure of the wings. The PhC structures are also found in many other objects in our nature. The main characteristic of these objects is the beautiful colors due to the complete reflection of light.

1.2 Mathematical Demonstration of Photonic Crystals

Generally, the periodicity of a PhC is represented mathematically by a 3D vector Λ, called lattice vector or Bravais lattice vector [8], as follow

$$\Lambda = l_1\mathbf{a}_1 + l_2\mathbf{a}_2 + l_3\mathbf{a}_3, \tag{1.1}$$

where $\mathbf{a}_1, \mathbf{a}_2, \mathbf{a}_3$ are three primitive lattice vectors, which are linearly independent vectors. l_1, l_2, l_3 are arbitrary integers. This lattice vector Λ can be understood that one point in the space is copied and placed along the lattice vector infinite times. Therefore, the whole space can be obtained by repeating one certain shape, called "unit cell", over all the possible lattice vectors. Unit cell of a lattice is not uniquely defined. The smallest one is called "primitive unit cell" is often defined as the parallelepiped formed by three primitive lattice vectors.

Now we consider a plane wave

$$E(\mathbf{r}, t) = E(\mathbf{r})e^{-i\omega t} = E_0 e^{i\mathbf{k}\mathbf{r} - i\omega t}, \tag{1.2}$$

propagating into this periodic lattice Λ, with amplitude E_0 and wave vector $\mathbf{k}$. Since the wave vector $\mathbf{k}$ can be chosen specifically to make wave function have the same periodicity as lattice vector Λ, so here we choose a wave vector $\mathbf{k} = \mathbf{G}$ satisfy the

equation below

$$e^{i\mathbf{G}\mathbf{r}} = e^{i\mathbf{G}(\mathbf{r}+\mathbf{R})}, \tag{1.3}$$

where $\mathbf{R}$ is the linear combination of three primitive lattice vectors $\mathbf{R} = l_1\mathbf{a}_1 + l_2\mathbf{a}_2 + l_3\mathbf{a}_3$. The Eq. (1.3) indicates that the value of plane wave at vector $\mathbf{r}$ is equal to the value of plane wave at vector $\mathbf{r} + \mathbf{R}$ in real space. Also from Eq. (1.3), we can see the condition below

$$e^{i\mathbf{G}\mathbf{R}} = 1, \tag{1.4}$$

All the vector $\mathbf{G}$ satisfying Eq. (1.4) will give rise to a new lattice corresponding to the Bravais lattice, called "reciprocal lattice". In general, reciprocal lattice is defined by three vectors $\mathbf{b}_1, \mathbf{b}_2, \mathbf{b}_3$, which have the relationship with $\mathbf{a}_1, \mathbf{a}_2, \mathbf{a}_3$ as follow

$$\mathbf{a}_i\mathbf{b}_j = 2\pi\delta_{ij}, \tag{1.5}$$

where δ_{ij} is Kronecker delta, $i, j = 1, 2, 3$. Then, lattice vector of reciprocal lattice is the linear combination of $\mathbf{b}_1, \mathbf{b}_2, \mathbf{b}_3$.

$$\mathbf{G} = n_1\mathbf{b}_1 + n_2\mathbf{b}_2 + n_3\mathbf{b}_3, \tag{1.6}$$

where n_1, n_2, n_3 are integers. It is easy to realize that vector $\mathbf{G}$ in the above equation satisfy the condition in Eq. (1.4). In analog to the Bravais lattice, reciprocal lattice also have a "primitive unit cell", which is called the first Brillouin zone (BZ) [8]. This first BZ is the parallelepiped formed by three vectors $\mathbf{b}_1, \mathbf{b}_2, \mathbf{b}_3$.

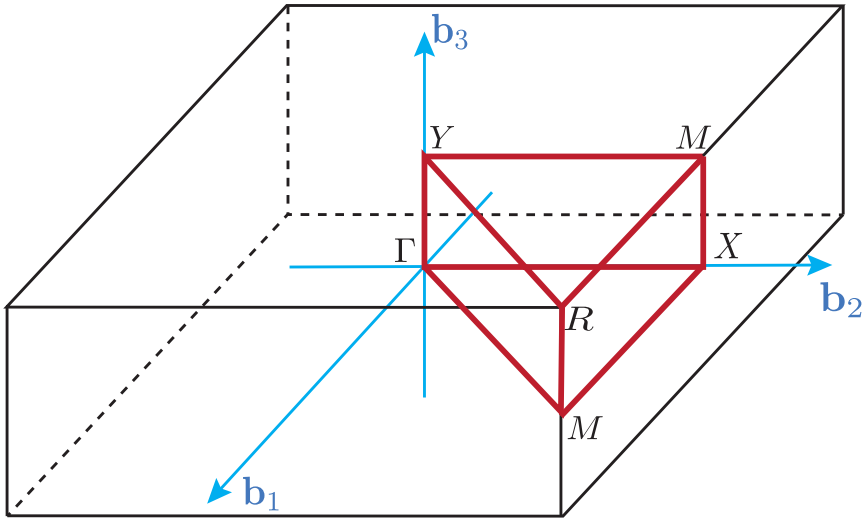

FIGURE 1.3: The first BZ of an rectangular parallelepiped with high symmetric points labeled by capital letters. Γ is the origin of the first BZ. Three primitive vectors in reciprocal space are drawn by blue color. The edges of irreducible BZ is drawn by red lines.

For each type of lattice, the first BZ has its own symmetries. For example, Fig. 1.3 presents the first BZ of an rectangular parallelepiped. It has 3 mirror symmetry planes go across two in three vectors $\mathbf{b}_1, \mathbf{b}_2, \mathbf{b}_3$. Therefore, the first BZ can be reduce to irreducible BZ labeled by red lines. These lines connect high symmetric points together, forming a path, called high symmetric path. The shape of BZ, irreducible BZ and position of high symmetric points are depend on each type of lattice.

1.3 Maxwell's Equations and Wave Equations

We start with the four Maxwell's equations, which describe the behaviour of light [5, 9]. Since we focus on the eigenfrequency of EM wave, we assume that electric current and free charge are absent. Maxwell's equations are now shown as below

$$\begin{aligned}
\nabla \cdot \mathbf{B}(\mathbf{r},t) &= 0, \\
\nabla \cdot \mathbf{D}(\mathbf{r},t) &= 0, \\
\nabla \times \mathbf{E}(\mathbf{r},t) &= -\frac{\partial}{\partial t}\mathbf{B}(\mathbf{r},t), \\
\nabla \times \mathbf{H}(\mathbf{r},t) &= \frac{\partial}{\partial t}\mathbf{D}(\mathbf{r},t),
\end{aligned} \tag{1.7}$$

where $\mathbf{B}$ is magnetic induction, $\mathbf{D}$ is electric field displacement, $\boldsymbol{E}$ is electric field, $\mathbf{H}$ is magnetic field. To derive wave equations, we need to know the relationship between $\mathbf{B}$ and $\mathbf{H}$, $\mathbf{D}$ and $\mathbf{E}$. Constitutive equations:

$$\begin{aligned}
\mathbf{B}(\mathbf{r},t) &= \mu_0 \mathbf{H}(\mathbf{r},t), \\
\mathbf{D}(\mathbf{r},t) &= \varepsilon_0 \varepsilon(\mathbf{r})\mathbf{E}(\mathbf{r},t),
\end{aligned} \tag{1.8}$$

here, ϵ_0 and μ_0 are electric permittivity and magnetic permeability in vacuum, respectively. $\epsilon(\mathbf{r})$ is relative permittivity or relative dielectric constant of material. In this thesis, we assume that dielectric constant $\varepsilon(\mathbf{r})$ is real, isotropic, perfectly periodic with respect to the spatial coordinate $\boldsymbol{r}$ and does not depend on frequency.

The above Maxwell's equations are time-dependent equations. Since they are linear equations, the time-dependent term can be eliminated by writing field function in the form of time-harmonic field as follow

$$\begin{aligned}
\mathbf{H}(\mathbf{r},t) &= \mathbf{H}(\mathbf{r})e^{-i\omega t}, \\
\mathbf{E}(\mathbf{r},t) &= \mathbf{E}(\mathbf{r})e^{-i\omega t},
\end{aligned} \tag{1.9}$$

Substituting Eq. (1.9) and also Eq. (1.8) into Eq. (1.7) we obtain

$$\nabla \cdot \mathbf{B}(\mathbf{r}) = 0, \tag{1.10a}$$
$$\nabla \cdot \mathbf{D}(\mathbf{r}) = 0, \tag{1.10b}$$
$$\nabla \times \mathbf{E}(\mathbf{r}) = i\omega\mu_0 \mathbf{H}(\mathbf{r}), \tag{1.10c}$$
$$\nabla \times \mathbf{H}(\mathbf{r}) = -i\omega\varepsilon_0 \varepsilon(\mathbf{r})\mathbf{E}(\mathbf{r}), \tag{1.10d}$$

Equation (1.10) still contain both electric field $\mathbf{E}$ and magnetic field $\mathbf{H}$. To decouple these two components, we take rotation of Eq. (1.10c) then substitute Eq. (1.10d) into it to obtain wave equation for electric field $\mathbf{E}$. Detail is as follow

$$\begin{aligned}
\nabla \times \nabla \times \mathbf{E}(\mathbf{r}) &= i\omega\mu_0 \nabla \times \mathbf{H}(\mathbf{r}) \\
\Rightarrow \nabla \times \nabla \times \mathbf{E}(\mathbf{r}) &= i\omega\mu_0 \left[-i\omega\varepsilon_0 \varepsilon(\mathbf{r})\mathbf{E}(\mathbf{r})\right] \\
\Rightarrow \nabla \times \nabla \times \mathbf{E}(\mathbf{r}) &= \omega^2 \mu_0 \varepsilon_0 \varepsilon(\mathbf{r})\mathbf{E}(\mathbf{r}) \\
\Rightarrow \frac{1}{\varepsilon(\mathbf{r})}\nabla \times \nabla \times \mathbf{E}(\mathbf{r}) &= \frac{\omega^2}{c^2}\mathbf{E}(\mathbf{r}).
\end{aligned} \tag{1.11}$$

here we put $c = \dfrac{1}{\sqrt{\mu_0\varepsilon_0}}$ is speed of light in vacuum.

Similarly, we take rotation of Eq. (1.10d) then substitute Eq. (1.10c) into it to obtain wave equation for magnetic field $\mathbf{H}$. From Eq. (1.10d) we have

$$\begin{aligned}
&\frac{1}{\varepsilon(\mathbf{r})}\nabla\times\mathbf{H}(\mathbf{r}) = -i\omega\varepsilon_0\mathbf{E}(\mathbf{r})\\
\Rightarrow\ &\nabla\times\frac{1}{\varepsilon(\mathbf{r})}\nabla\times\mathbf{H}(\mathbf{r}) = -i\omega\varepsilon_0\nabla\times\mathbf{E}(\mathbf{r})\\
\Rightarrow\ &\nabla\times\frac{1}{\varepsilon(\mathbf{r})}\nabla\times\mathbf{H}(\mathbf{r}) = -i\omega\varepsilon_0\left[i\omega\mu_0\mathbf{H}(\mathbf{r})\right]\\
\Rightarrow\ &\nabla\times\frac{1}{\varepsilon(\mathbf{r})}\nabla\times\mathbf{H}(\mathbf{r}) = \frac{\omega^2}{c^2}\mathbf{H}(\mathbf{r}).
\end{aligned} \tag{1.12}$$

To find electric and magnetic components of EM wave propagating in a PhC, we need to solve eigenvalue equations (1.11) and (1.12), separately. However, since these two components always couple to each other, only one of two wave equations is needed, then the remain component can be obtain by the following relation

$$\mathbf{E}(\mathbf{r}) = \frac{i}{\omega\varepsilon_0\varepsilon(\mathbf{r})}\nabla\times\mathbf{H}(\mathbf{r}), \tag{1.13a}$$

$$\mathbf{H}(\mathbf{r}) = \frac{-i}{\omega\mu_0}\nabla\times\mathbf{E}(\mathbf{r}). \tag{1.13b}$$

Equations. (1.11) or (1.12) are standard differential equations, called Master equations, used to describe behaviour of EM wave in PhC. Depending on each numerical environment, one of these two equation have more benefits than the other one. All the results in this thesis is obtained by solving one of these two equations.

1.4 Photonic Band Structure and Photonic Band Gap

To obtain the eigenmodes of PhCs, according to Bloch theorem [10], electric and magnetic wave function should be written in term of plane waves and modulated by a periodic function

$$\mathbf{H}(\mathbf{r}) = u_{\mathbf{k}}(\mathbf{r})\, e^{i\mathbf{k}\mathbf{r}}, \tag{1.14a}$$

$$\mathbf{E}(\mathbf{r}) = v_{\mathbf{k}}(\mathbf{r})\, e^{i\mathbf{k}\mathbf{r}}, \tag{1.14b}$$

where $u_{\mathbf{k}}(\mathbf{r})$ and $v_{\mathbf{k}}(\mathbf{r})$ are periodic function, which satisfy the periodicity of the lattice

$$u_{\mathbf{k}}(\mathbf{r}) = u_{\mathbf{k}}(\mathbf{r}+\mathbf{R}), \tag{1.15a}$$

$$v_{\mathbf{k}}(\mathbf{r}) = v_{\mathbf{k}}(\mathbf{r}+\mathbf{R}). \tag{1.15b}$$

Because of the periodic boundary condition, the eigenvalue problem of PhCs can be restricted to one unit cell. Solving the Master equations, the eigenvalues $\omega(\mathbf{k})$ and eigenvectors as wave functions can be obtained. The relation of ω and wave vectors $\mathbf{k}$ are called dispersion relation. In a homogeneous media with dielectric constant ε, this dispersion relation is

$$\omega(\mathbf{k}) = \frac{c}{\sqrt{\varepsilon}}\mathbf{k}. \tag{1.16}$$

The wave vectors **k** is belonged to the reciprocal space. Because of the periodicity of reciprocal lattice as discussed in section 1.2, value of **k** is restricted to within the first BZ. Other value beyond the first BZ will represent the repetition of both eigenvalues and eigenvectors. The dispersion relation is separated into lines, called photonic

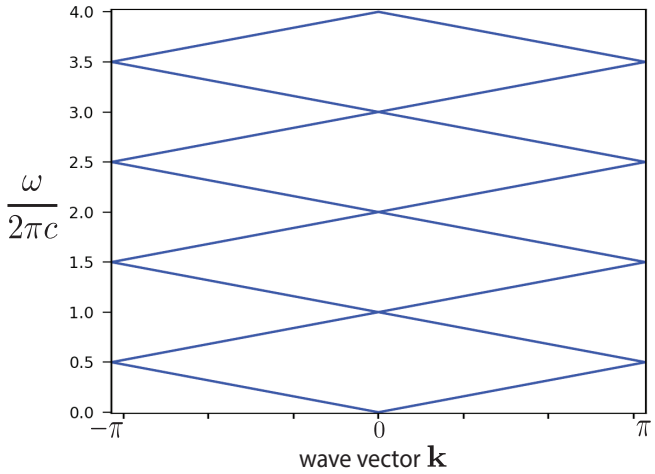

FIGURE 1.4: Frequency dispersion of light in vacuum $\varepsilon = 1$.

bands. The set of these bands are called photonic band structure. In Fig. 1.4, we plot the photonic band structure of EM wave propagating in vacuum. The horizontal axis represent wave vector **k**. In one dimension it is from $-\pi$ to π.

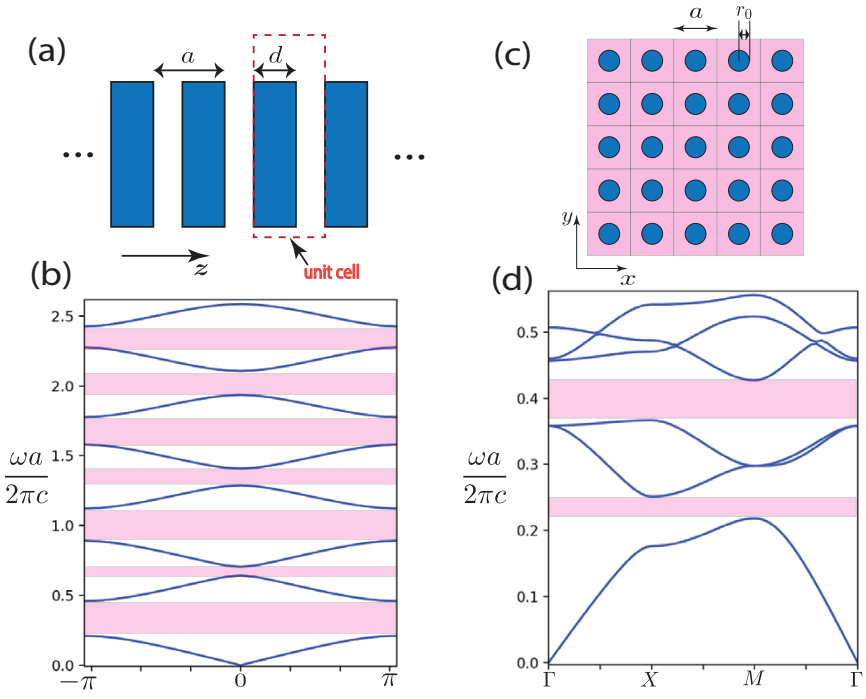

FIGURE 1.5: PhCs and their corresponding photonic band structures. (a) 1D PhC, where dielectric slabs are arranged periodically in z direction. (b) Photonic band structure for 1D PhC in (a). (c) 2D PhC, where dielectric rods are arranged periodically in x and y directions. (d) Photonic band structure for 2D PhC in (c).

For PhC structures, where dielectric functions are not constants but periodic functions, photonic band structures are obtained by solving Master equations. For

example, here we present photonic band structures for two simple PhCs. In Fig. 1.5(a), many dielectric slabs, whose thickness and dielectric constant is d and ε, are arranged periodically in z direction, which formed an 1D PhC. Unit cell is labeled by the red dash line. Lattice constant for this 1D PhC is a. Photonic band structure for $d/a = 0.8$ and $\varepsilon = 12.25$ is shown in Fig. 1.5(b). Photonic bands and band gaps appear alternately for this 1D PhC. The band gaps is a forbidden region where EM wave in this frequency range can not propagate into the crystals. Fig. 1.5(c) is the schematic of 2D PhC, where dielectric rods, whose radii are r and dielectric constant is $\varepsilon\prime$, are arranged periodically in air and in both x and y directions. The photonic band structure with $r/a = 0.38$, $\varepsilon\prime = 11.7$ is shown in Fig. 1.5(d). For this 2D PhC, photonic band structure still consists of bands and band gaps, which is more complicated than 1D PhC due to the inhomogeneous in two directions. The above results is obtained by solving Master equations of electric field 1.11.

Photonic band gap is the most important characteristic of PhC. The origin of photonic band gap is due to the total reflection of EM wave at many interface between two materials. For example, in a semi-infinite 1D PhC as shown in Fig. 1.6, the incident light $e^{i\mathbf{k}z}$ is reflected when it meet the interfaces between dielectric material and air. Assuming that the reflectivity is r, the reflection light amplitude is $re^{-i\mathbf{k}z}$. No matter how small the reflectivity r is, the total refection R from semi-infinite 1D PhC is

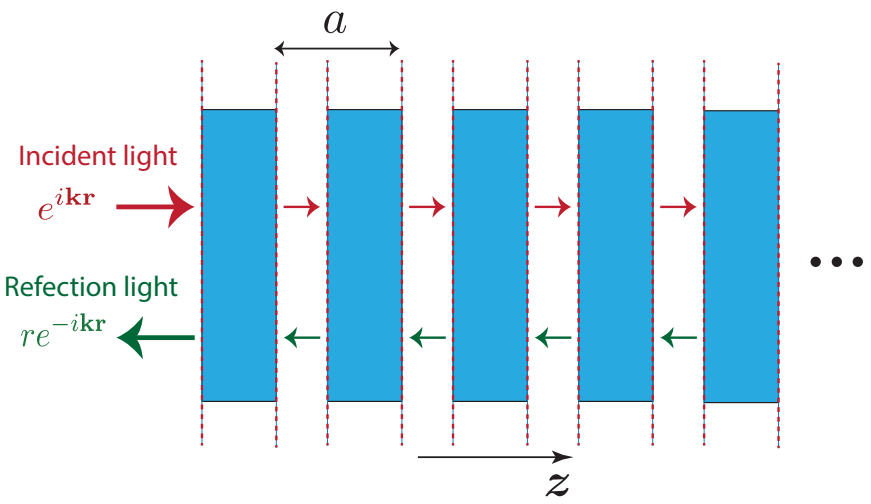

FIGURE 1.6: Multi-reflection of light at the interface between two materials in 1D PhC.

$$\begin{aligned} R =& re^{-i\mathbf{k}z} + re^{-i\mathbf{k}z}e^{-i\mathbf{k}2a} + re^{-i\mathbf{k}z}e^{-i\mathbf{k}4a} + \dots \\ \approx& re^{-i\mathbf{k}z}\frac{1}{1-e^{-i\mathbf{k}2a}} \end{aligned} \tag{1.17}$$

The above formula will diverge if

$$\begin{aligned} e^{-i\mathbf{k}2a} &= 1 \\ \Rightarrow \mathbf{k} &= \frac{n\pi}{a}. \end{aligned} \tag{1.18}$$

where n is integers. The above condition of wave vector is called Bragg condition. Light with frequency satisfy condition 1.18 can not propagate into PhC, which cause photonic band gaps. In the experimental point of view, the wider the band gap is,

the more interesting it is. In almost the results in this thesis, we try to examine the novel properties of PhCs inside the band gap.

1.5 Numerical Calculation Methods

Almost things in the world around us and their characteristics can be represented by mathematical equations, PhCs are not an exception. However, solving the mathematical equations analytically is not an easy task. It is possible for some very simple cases, almost cases are very complicated. That is why numerical calculation methods come to play. These methods are based on discrete calculations, where the parameters are divided in to finite set of small segments. Then solutions are obtained for each small segment. The key factor for numerical methods is that the numerical solutions must converge to the real solutions. The difference between numerical and real solution can be made arbitrarily small by dividing parameters into more small segments. These methods can solve the problem directly by writing code in computers.

There are many numerical methods that can be used to model the flow of light in PhCs. Here we explain three numerical methods, which are mostly used in solving problems of PhCs. The first one is plane wave expansion (PWE) method. This method is the most popular method in the PhC community to solve the photonic band structure. As its name is, this method uses time-harmonic form and expand wave function to numbers of plane wave by Fourier series along reciprocal space. Similarly, the dielectric function is also expand to Fourier series. PWE method is highly efficient for solving eigenmodes of PhCs. However, it suffers from the Gibbs phenomena, which make dielectric function converges very slowly when the dielectric contrast are very high. Moreover, this method is also time-consuming.

The next method we will mention is finite different method (FDM). This method solves the differential equation by approximating derivatives with finite differences. The spatial domain is discretized and the solution at each grid point is obtained by the solution of nearby points and the finite differences. The main advantage of FDM is that it is easy to understand and implement. This method is often used for rectangular or cubic shape objects. Compared with PWE method, FDM is less time-consuming.

The third method is finite element method (FEM). To solve the problem, FEM divides the large domain in to smaller and simpler parts, called finite elements. For example, real space is discretized by space dimension. Each small mesh is called a numerical domain for obtaining solution. The feature which makes this method become attractive is that it can handle complicated geometries with relatively ease. While other methods are restricted for some types of geometry, FEM can be applied for all structures. The quality of approximation of FEM is often higher than FDM because of the flexible mesh of FEM.

There are many commercial and open software using above methods to solve the eigenvalue problem of PhCs, such as COMSOL Multiphysics [11] using FEM and MIT Photonic Band (MPB) [12] using FDM. In this thesis, we used above three methods alternately depending on the convenience and the accuracy of each method.

1.6 The Organization of this Thesis

In this doctoral thesis, we theoretically study topological properties of 3D PhCs. We pay more attention to the boundary states inside the photonic band gap, which

are derived from topological transitions of bulk states. The numerical calculation methods for topological invariants (Zak phase and Wilson Loop) of 3D PhCs is also introduced and explained.

Before going to the main part of the thesis about higher order topological states of 3D PhCs, in chapter 2, we briefly review about topological PhCs and examine a new 2D topological PhCs. Starting from the definition of "topology" and the often-used topological invariants, we introduce a new PhC structure following Biphenylene (BPN) network. We numerically calculate Zak phase and examine several types of ribbon structure by FDM and PWE methods. Our findings show that the first order topological states as edge states are found in the photonic band gap due to the total π Zak phase. The second order topological states as corner states are also obtained as a results of non-zero product of Zak phase in two ribbon directions.

Chapter 3 is used for present the studies of simple cubic PhC. In this 3D PhC, the inversion symmetry is preserved. Therefore, Zak phase is theoretically predicted to be quantized to 0 or π values. We explain the calculation method then numerically calculate Zak phase for the two lowest photonic bands of this structure. The results are consistent with the prediction based on the parity of field distribution at high symmetric points. Because of the π difference of Zak phase, the first order topology as 2D interface states are numerically observed. Topological hinge states are also numerically obtained by using FEM.

In chapter 4, we extend the studies to a 3D PhC structure which is in absence of inversion symmetry, called Woodpile PhC. Due to this symmetry absence, Zak phase does not have quantized values as in simple cubic PhC. It takes the value from $-\pi$ to π depending on each points. Therefore, we call it Wilson Loop instead of Zak phase. Due to the geometry of lattice, the numerical calculation method need to be slightly changed. The topological contrast are seen in this structure when the origin of the unit cell is shifted, resulting in the emergence of boundary states between two kinds of unit cell. In this woodpile structure, there is a selection rule for topological hinge states since they do not exist at all positions of hinge. This selection rules will be discussed at the end of this chapter.

We conclude in chapter 5 by summarizing all results of this thesis and providing the suggestion for experiments and future researches.

Chapter 2

Topological Photonic Crystals

In this chapter, we will explain about the concept of "topology" and the application of topology to PhCs. Then, we explain about the topological invariants which are often used in examining topological PhCs. A new PhC structure following Biphenylene (BPN) network and its topological properties will be introduced and determined.

2.1 What is Topology?

"Topology" is a mathematical concept, which describes the a quantity of a geometric object that is preserved under a continuous deformation [13] such as shrinking, stretching, bending and twisting. This can be understood as the number of hole on the body of the object is remained unchanged during the deformation. Figure 2.1 is

FIGURE 2.1: An example of topological equivalent in objects. A soccer ball and an egg have no hole on the body. A coffee cup and a donut have one hole on the body.

an example of topological equivalent in objects. A soccer ball and an egg have no hole on the body. By shrinking the shape of the soccer ball, shape of the egg can be obtained. Therefore, they are topological equivalent. These two objects are topologically different from a coffee cup and a donuts since the coffee cup and the donut have one hole on the body. Without creating a hole, a soccer ball and an egg can not transform to a coffee cup or a donut. The number of hole is a factor to distinguish topological properties of objects.

How to apply "topology" to the band theory? It was first applied to solid-state physics [14–17] and has resulted in topological band theory. Figure 2.2 is the schematic of band inversion in topological band theory. A trivial band gap is created by two bands labeled in red and blue. These two bands touch each other at critical point after a continuous deformation in (b), which close the trivial band gap. Then, by cutting two bands at some points, the band gap is reopen with the inverted bands. This is called discontinuous transformation.

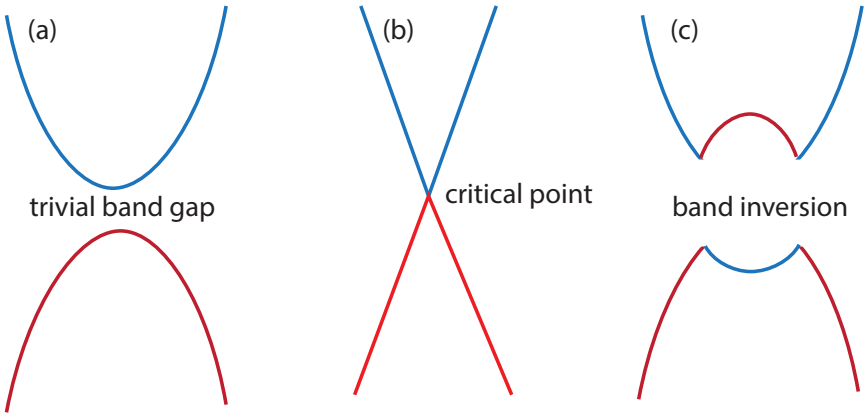

FIGURE 2.2: The schematic of band inversion between two bands. The trivial band gap in (a) is closed at the critical point in (b) then reopened and inverted in (c).

In topological band theory, band inversion is an important feature to distinguish topological properties of electronic systems. Together with band structure, the corresponding Bloch states will also be inverted leading to many novel physical properties that do not exist in the trivial systems. Similarly, in photonic systems, band inversion is also an remarkable signal of topological properties. Topological PhCs were first-time theoretically studied by Raghu and Haldane [18], and experimentally observed by Wang et al [19, 20]. These initial works has stimulated many researches of topological PhCs [21–25].

2.2 Topological Invariants

To classify characteristics of topological systems, we used the topological invariants which is remained unchanged during the electronic/photonic band evolution. In the example in Fig. 2.1, topological invariant is the number of hole on each object. In topological band theory, what is corresponding to the number of hole? It will be explained in this section.

2.2.1 Berry Phase and Zak Phase

As mentioned in section 1.4, the frequency dispersion of PhC systems is separated into lines called photonic band structure. This photonic band structure is defined in the wave vector space. For continuous media or systems, it is infinite momentum space, for periodic systems, it is restricted to the first BZ. Corresponding to each point of photonic band structure, there is one or more eigenmodes. Here we present Berry phase in PhC systems, means periodic systems. Berry phase is defined as geometric phase that the eigenmode of the n-th band acquired during an adiabatic evolution along a closed path in a momentum space. Because of the periodicity of the crystals, the closed path we mentioned here is the first BZ. Berry phase is mathematically defined as the integral of Berry connection over the first BZ. For example, Berry phase in a PhC systems is written as follow

$$\gamma^n = \oint_{1^{st}BZ} \mathbf{A}^n(\mathbf{k}) d\mathbf{k}, \tag{2.1}$$

where n is band index, $\mathbf{A}^n(\mathbf{k})$ is Berry connection, known as

$$\mathbf{A}^n(\mathbf{k}) = i\langle U^n_{\mathbf{k}}(\mathbf{r})|\nabla|U^n_{\mathbf{k}}(\mathbf{r})\rangle, \tag{2.2}$$

Here $U^n_{\mathbf{k}}(\mathbf{r})$ is the periodic Bloch function of EM wave $U^n_{\mathbf{k}}(\mathbf{r}) = \left[u^n_{\mathbf{k}}(\mathbf{r}), v^n_{\mathbf{k}}(\mathbf{r})\right]^\top$. Throughout this thesis, the integral over $\mathbf{k}$ is taken within the first BZ. Spatial parameter $\mathbf{r}$ is performed within the unit cell.

Since electric and magnetic fields of EM wave can be determined from each other via Eq. (1.13). One of them is enough for Berry phase calculation. In other words, Berry phase can be calculated by using periodic Bloch function of either electric field or magnetic field. Eq. (2.2) is simplified to one in the following two equations

$$\mathbf{A}^n(\mathbf{k}) = i\langle u^n_{\mathbf{k}}(\mathbf{r})|\nabla|u^n_{\mathbf{k}}(\mathbf{r})\rangle, \tag{2.3a}$$
$$\mathbf{A}^n(\mathbf{k}) = i\langle v^n_{\mathbf{k}}(\mathbf{r})|\nabla|v^n_{\mathbf{k}}(\mathbf{r})\rangle. \tag{2.3b}$$

This Berry connection is gauge-dependent. However, Berry phase is gauge invariant in the unit of 2π because of the first and the last points of the integral are coincided.

In the situation of 1D systems, Berry phase is denoted as Zak phase [26]. Making the relation to electronic systems, Zak phase represents charge polarization in real space. In 2D systems, Zak phase is determined for any in-plane directions [27–30]. For example, in a 2D squared lattice system, Zak phase on x-direction will depend on k_x and calculated by taking the integral over k_y, $-\pi \leq k_x, k_y \leq \pi$. Similarly, in a 3D system, Zak phase is determined as an integral of Berry connection over one direction and depending on other two directions. In the presence of inversion symmetry, Zak phase is quantized to π (nontrivial) and 0 (trivial) [26].

2.2.2 Berry Curvature and Chern number

Berry curvature is also an important gauge-invariant quantity when considering topological properties of a system. In photonic systems, Berry curvature is known as the local expression of geometric phase of wavefunction in the momentum space. It is mathematically defined as

$$\mathbf{\Omega}^n(\mathbf{k}) = \nabla \times \mathbf{A}^n(\mathbf{k}), \tag{2.4}$$

Berry phase is also expressed depending on Berry curvature $\mathbf{\Omega}^n(\mathbf{k})$ by using Stoke's theorem

$$\gamma^n = \oint_{1^{st}BZ} \mathbf{A}^n(\mathbf{k}) d\mathbf{k} = \iint_{\mathbf{S}} \left(\nabla \times \mathbf{A}^n(\mathbf{k})\right) d\mathbf{S} = \iint_{\mathbf{S}} \mathbf{\Omega}^n(\mathbf{k})\, d\mathbf{S}. \tag{2.5}$$

where $\mathbf{S}$ is the surface area surrounded by the closed path of Berry phase integral. Because $\mathbf{S}$ is a closed manifold surface, the integral of Berry curvature over $\mathbf{S}$ is quantized in the unit of 2π according to Chern theorem [31]. This number is called Chern number, which is essential for analyzing quantum effects in the broken time-reversal symmetry (TRS) [32] or valley effects [33, 34]. In 2D systems, Chern number of the n-th band is

$$C^n = \frac{1}{2\pi} \iint_{1^{st}BZ} \mathbf{\Omega}^n(\mathbf{k})\, dk^2. \tag{2.6}$$

In the presence or absence of TRS, Chern number is zero or non-zero, respectively. However, in the systems with valley degree of freedom, Chern number can be calculated for a part of the first BZ to see the contribution of each valley [33, 34] to

the total Chern number. Therefore, the term "valley Chern number" appears. When TRS is preseved, valley Chern number can be different from zero, but the total valley Chern number in the first BZ is always zero, which equal to Chern number.

2.3 Topological States of Biphenylene Photonic Crystal

In this section, we study the topological properties of PhC system following BPN network, so-call BPN PhC. Both FDM and FEM are used to evaluate photonic band structure and topological invariants. The first order and second order topological states of BPN PhC will be pointed out in this section. In the end, we will point out the condition for the emergence of topological corner states.

2.3.1 Biphenylene Photonic Crystal

Following the successful applications of graphene and other nano-electronic materials, the searching of 2D carbon allotropes other than graphene, such as BPN or graphenylene network, has stimulated and brought a new insight for electronic transport properties in nanoscale materials. In recent research, Fan et al. has successfully synthesized the 2D BPN network [35]. Motivated from this experimental results, A. Bafekry et al. has performed the detailed of density functional theory-based first-principles calculations to deeply study the electronic and optical properties of this material [36].

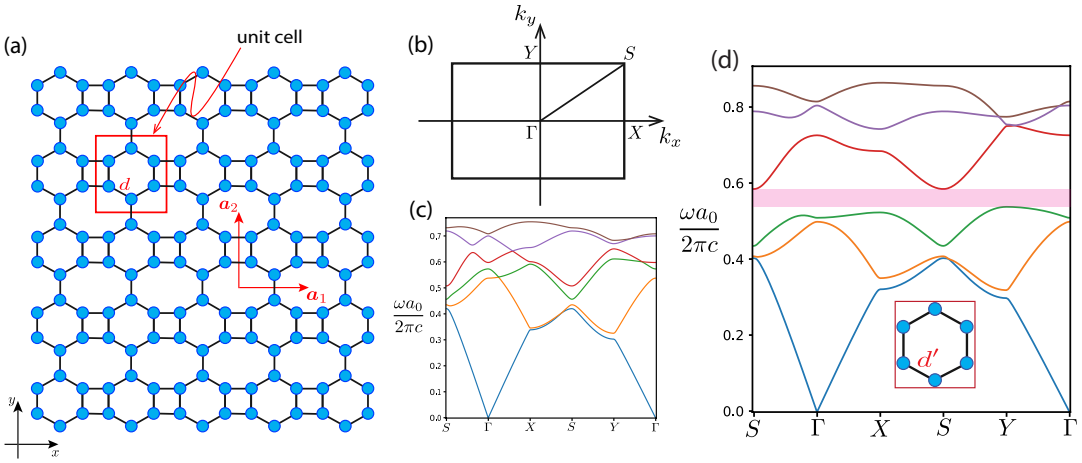

FIGURE 2.3: (a) Schematic of 2D BPN PhC. $\mathbf{a_1} = (a_0, 0)$ and $\mathbf{a_2} = (0, a_T) = (0, \frac{3a_0}{\sqrt{3}+1})$ are primitive vectors. Here, a_0 and a_T are the lattice constants in x- and y-direction, respectively. Red rectangle indicates the primitive unit cell, which contains six equivalent dielectric rods, colored with cyan. The radii for these rods are r_0, distance between each rod to the center of unit cell is d. (b) The corresponding first Brillouin zone of 2D BPN lattice with high symmetric points. (c) Photonic band structure for 2D BPN PhC with $d = \frac{a_0}{\sqrt{3}+1}$, $r_0 = 0.2d$. (d) Photonic band structure for modified BPN PhC with $d = \frac{1.3a_0}{\sqrt{3}+1}$, $r_0 = 0.2d$. The inset shows the schematic of one unit cell of modified BPN PhC.

Inspired from the study of 2D BPN network, we introduce BPN PhC following the BPN network structure. Our PhC consist of one type of circular dielectric rod,

which are periodically arranged in 2D array. Figure 2.3(a) shows the lattice structure of BPN PhC, where the red rectangle indicates primitive unit cell. There are six equivalent dielectric rods in one unit cell, colored by cyan. Radius for each rod is r_0. In this study, we assume that all the dielectric rods are made of silicon, with dielectric constant are $\varepsilon = 11.7$. These rods are arranged periodically in BPN lattice with periodic constant in x- and y-directions are a_0 and $a_T = \frac{3a_0}{\sqrt{3}+1}$, respectively. Distance between two nearest dielectric rods is d, it equals to distance between each rod to the center of unit cell. $\mathbf{a_1} = (a_0, 0)$ and $\mathbf{a_2} = (0, a_T) = (0, \frac{3a_0}{\sqrt{3}+1})$ are two primitive lattice vectors. All the calculation for this BPN PhC will be done for transverse magnetic modes where magnetic field is in the xy plane, electric field is perpendicular to xy plane. Eigenvalue equation is given as Eq. (1.11). Figure 2.3(b) shows the corresponding first Brillouin zone for 2D BPN lattice with high symmetric points.

The photonic band structure for $d = \frac{a_0}{\sqrt{3}+1}$ and $r_0 = 0.2d$ are shown in Fig. 2.3(c). As can be seen that, there is no band gap in this PhC structure, all bands connect to others by linear dispersion at degenerate points. To examine topological properties in BPN PhC, we need to open a complete band gap in photonic band structure. Therefore, we slightly modify the lattice structure by increasing the distance d between each rod and the center of unit cell. From here, the distance d will become $d' = 1.3d$ and size of rods and of the unit cell is kept the same as original structure, which can be seen in the inset of Fig. 2.3(d).

The new photonic band structure is shown in Fig. 2.3(d). A complete band gap, labeled by shaded pink color, is found around normalized frequency 0.55 and it is between the third and the fourth band. Band 1 and band 2 are still connected by a degenerate point in $S - Y$ line. Band 3 is now isolated from others. From here, we will examine the modified BPN PhC and we only focus on three lowest photonic band below the band gap.

2.3.2 Zak Phase and Topological Edge States

In this section, firstly, we explain about numerical calculation method used to evaluate Zak phase for any in-plane directions. Then, we discuss about the localization of EM wave at the edges of several ribbon structures. Since Zak phase of a ribbon is defined by Zak phase on the direction paralleled to the ribbon. Therefore, we may mix the words "Zak phase of ribbon" and "Zak phase on the direction" in the remaining part of this section.

Here we assume that the ribbon structure is periodic under translation vector $\mathbf{T} = \mathbf{T}(m, n) = m\mathbf{a}_1 + n\mathbf{a}_2$, where $\mathbf{a}_1$ and $\mathbf{a}_2$ are two primitive lattice vectors, m and n are coprime integers. If they are not coprime, the two vectors defined below do not form the basis set in reciprocal space. Normally, the 2D BZ that is used to calculated Zak phase is the 1st BZ. In general cases, the 2D BZ is chosen as a rectangular momentum area formed by two orthogonal vectors $\mathbf{\Gamma}_{\parallel}$ and $\mathbf{\Gamma}_{\perp}$. These two vectors are defined as follows

$$\mathbf{\Gamma}_{\parallel} = \frac{2\pi\mathbf{T}}{|\mathbf{T}|^2}, \tag{2.7}$$

This $\mathbf{\Gamma}_{\parallel}$ is parallel to ribbon orientation (parallel to $\mathbf{T}$). It is also defined for the one-dimensional first BZ of the ribbon structure. The second vector $\mathbf{\Gamma}_{\perp}$ is perpendicular to $\mathbf{\Gamma}_{\parallel}$ and relates to $\mathbf{\Gamma}_{\parallel}$ by the following formula

$$\mathbf{\Gamma}_{\parallel} \times \mathbf{\Gamma}_{\perp} = \mathbf{b}_1 \times \mathbf{b}_2, \tag{2.8}$$

where $\mathbf{b}_1$ and $\mathbf{b}_2$ are two primitive vectors in reciprocal space and defined by $\mathbf{a}_i\mathbf{b}_j = 2\pi\delta_{ij}$ $(i,j=1,2)$. Eq. (2.8) indicates that the area of the new BZ formed by $\mathbf{\Gamma}_\parallel$ and $\mathbf{\Gamma}_\perp$ equals to the area of the 1st BZ.

For the ribbon in any direction characterized by vector $\mathbf{T}$, Zak phase of n-th band is computed by integrating Berry connection over $\mathbf{\Gamma}_\perp$ as follow

$$Z^n\left(k_\parallel\right) = \oint_{\mathbf{\Gamma}_\perp} \langle u^n_{\mathbf{k}}\left(\mathbf{r}\right)|i\partial_{\mathbf{k}}|u^n_{\mathbf{k}}\left(\mathbf{r}\right)\rangle dk_\perp, \tag{2.9}$$

where $u^n_{\mathbf{k}}\left(\mathbf{r}\right)$ is the periodic part of Bloch wave function $\mathbf{E}^n_{\mathbf{k}}\left(\mathbf{r}\right) = u^n_{\mathbf{k}}\left(\mathbf{r}\right)e^{i\mathbf{kr}}$, $\mathbf{k}_\parallel$ and $\mathbf{k}_\perp$ are momentum components that are parallel to $\mathbf{\Gamma}_\parallel$ and $\mathbf{\Gamma}_\perp$. For numerical calculation, we do an approximation for Eq. (2.9) by dividing $\mathbf{\Gamma}_\parallel$ and $\mathbf{\Gamma}_\perp$ into N_0 segments then taking sum of contribution of each segment. Then we obtain the discrete formula as shown below

$$Z^n\left(k_i\right) = -\operatorname{Im}\left(\log\prod_{k_j}\langle u^n_{k_i,k_j}\left(\mathbf{r}\right)|u^n_{k_i,k_{j+1}}\left(\mathbf{r}\right)\rangle\right), \tag{2.10}$$

where k_i is discrete k-point of $\mathbf{\Gamma}_\parallel$ and k_j is discrete k-point of $\mathbf{\Gamma}_\perp$, $(i,j=1,...,N_0)$. The Eq. (2.10) indicates that Zak phase can be calculated for each k_i point in $\mathbf{\Gamma}_\parallel$ direction. Equation (2.10) is used for single band. For a group of degenerate bands, the scalar products is replaced by overlap matrices. The overlap matrix S for group of N degenerate bands between two k-point $\mathbf{k}_1$ and $\mathbf{k}_2$ is

$$S_{\mathbf{k}_1\mathbf{k}_2} = \begin{bmatrix} \langle u^1_{\mathbf{k}_1}\left(\mathbf{r}\right)|u^1_{\mathbf{k}_2}\left(\mathbf{r}\right)\rangle & \langle u^1_{\mathbf{k}_1}\left(\mathbf{r}\right)|u^2_{\mathbf{k}_2}\left(\mathbf{r}\right)\rangle & ... & \langle u^1_{\mathbf{k}_1}\left(\mathbf{r}\right)|u^N_{\mathbf{k}_2}\left(\mathbf{r}\right)\rangle \\ \langle u^2_{\mathbf{k}_1}\left(\mathbf{r}\right)|u^1_{\mathbf{k}_2}\left(\mathbf{r}\right)\rangle & \langle u^2_{\mathbf{k}_1}\left(\mathbf{r}\right)|u^2_{\mathbf{k}_2}\left(\mathbf{r}\right)\rangle & ... & \langle u^2_{\mathbf{k}_1}\left(\mathbf{r}\right)|u^N_{\mathbf{k}_2}\left(\mathbf{r}\right)\rangle \\ ... & ... & ... & ... \\ \langle u^N_{\mathbf{k}_1}\left(\mathbf{r}\right)|u^1_{\mathbf{k}_2}\left(\mathbf{r}\right)\rangle & \langle u^N_{\mathbf{k}_1}\left(\mathbf{r}\right)|u^2_{\mathbf{k}_2}\left(\mathbf{r}\right)\rangle & ... & \langle u^N_{\mathbf{k}_1}\left(\mathbf{r}\right)|u^N_{\mathbf{k}_2}\left(\mathbf{r}\right)\rangle \end{bmatrix}, \tag{2.11}$$

where the index l of $u^l_{\mathbf{k}}$ indicates band index.

Total Berry connection in matrix form is shown below

$$\hat{S}\left(k_i\right) = -\operatorname{Im}\left(\log\prod_{k_j} S_{k_ik_j,k_ik_{j+1}}\right), \tag{2.12}$$

To evaluate Zak phase for n-th band, we need the n-th eigenvalues s^n of the Berry connection matrix $\hat{S}\left(k_i\right)$. Then Zak phase for n-th subband is given by

$$Z^n\left(k_i\right) = -\operatorname{Im}\log\left(s^n\right). \tag{2.13}$$

Now we apply the above method to calculate Zak phase of several type of BPN PhC ribbons. Figure 2.4(a) is the schematic of three types of ribbon that we will examine in this paper. The red line indicates zigzag ribbon. This kind of ribbon is periodic under the translation vector $\mathbf{T}_1 = \mathbf{T}\left(1,0\right) = \mathbf{a}_1$. The green line denotes armchair ribbon which is periodic under translation vector $\mathbf{T}_2 = \mathbf{T}\left(0,1\right) = \mathbf{a}_2$. The orange line shows the ribbon structure being periodic under translation vector $\mathbf{T}_3 = \mathbf{T}\left(1,1\right) = \mathbf{a}_1 + \mathbf{a}_2$, so-call cross ribbon. In Fig. 2.4(b), we plot the momentum areas, which are used to calculate Zak phase. Blue rectangle is momentum area for calculating Zak phase of zigzag and armchair ribbons, which is overlapped with the 1st BZ. Red and green bold lines are the first Brillouin zones for zigzag and armchair

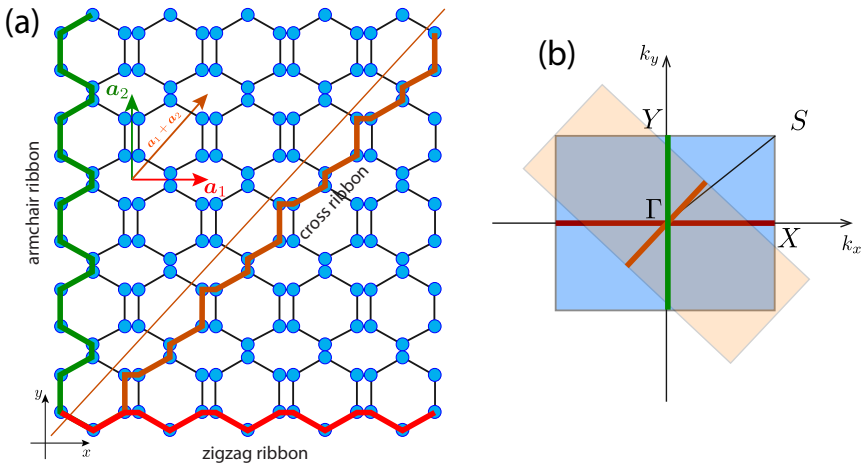

FIGURE 2.4: (a) Schematic of investigated BPN PhC ribbon structures. Red line indicates zigzag ribbon, which is periodic under translation vector $\mathbf{T}_1 = \mathbf{a}_1$. Armchair ribbon is expressed as green line with translation vector $\mathbf{T}_2 = \mathbf{a}_2$. Orange line denotes the cross ribbon being periodic under vector $\mathbf{T}_3 = \mathbf{a}_1 + \mathbf{a}_2$. (b) The momentum areas used for calculate Zak phase of each type of ribbon. Blue rectangle is momentum area for Zak phase calculation of zigzag and armchair ribbon. Orange rectangle is momentum area for Zak phase calculation of cross ribbon. Red, green and orange lines are the first Brillouin zones for zigzag, armchair and cross ribbons, respectively.

ribbons, respectively. Orange rectangle is momentum area for computing Zak phase of cross ribbon, orange bold line denotes the first Brillouin zone for cross ribbon.

As can be seen in photonic band structure in Fig. 2.3(d), the first and the second band are connected by one degenerate point, the third band is isolated. To calculate Zak phase for each type of ribbon, we use Eq. (2.12) for the first and second bands, Eq. (2.10) for band 3.

For the zigzag ribbon structure which is parallel to x-axis, $\mathbf{\Gamma}_{\parallel} = \left(\frac{2\pi}{a_0}, 0\right)$, $\mathbf{\Gamma}_{\perp} = \left(0, \frac{2\pi}{a_T}\right)$, then we choose $k_{\parallel} = \left(-\frac{\pi}{a_0}, 0\right) \rightarrow \left(\frac{\pi}{a_0}, 0\right)$, $k_{\perp} = \left(0, -\frac{\pi}{a_T}\right) \rightarrow \left(0, \frac{\pi}{a_T}\right)$. Figure 2.5(a) is schematic of zigzag ribbon, which is periodic along x-direction and finite in y-direction. Therefore, in numerical calculation, x-direction is applied periodic boundary condition and y-direction is applied perfect magnetic conductor (PMC) boundary condition. Zak phase in x-direction for the first three bands and the zigzag ribbon photonic band structure are shown in Fig. 2.5(b) and (c), respectively. The 1st and the 2nd bands have k-dependent Zak phase due to the degenerate point in $S - Y$ line. Total Zak phase for these two bands is π leading to the topological edge states in between the 2nd and the 3rd band as denoted by the red lines in Fig. 2.5(c). Edge states should appear at all k points in the 1st BZ, but in this structure, the band gap between band 2 and 3 is not a complete band gap, edge states in the center of the 1st BZ are mixed with bulk states, they are somewhere in the bulk region that can not be detected by numerical calculation. Zak phase for band 3 is 0. So, the complete band gap becomes topologically-nontrivial because total Zak phase is π. The isolated edge states in between band 3 and band 4 should appear at all k points. However, it emerge only at the center of the first BZ because of the PMC boundary condition. To realize the topological edge states in the whole first BZ, later we will change the boundary condition by creating the interface between zigzag ribbon and a trivial PhC.

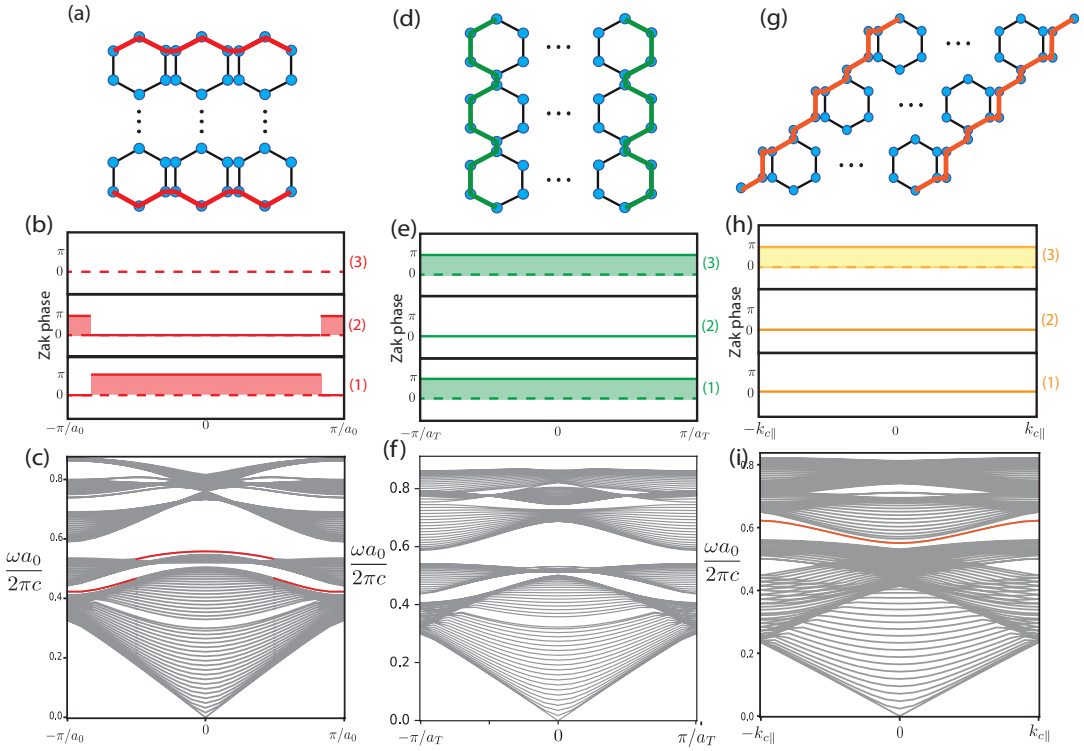

FIGURE 2.5: (a) The schematic of supercell used for determining zigzag edge states, which is periodic along x-direction and finite in y-direction. (b) Zak phase of the first three band of BPN PhC in zigzag direction. (c) Photonic band structure for the zigzag ribbon. The red lines indicate topological edge states. (d) The schematic of supercell used for determining armchair edge states, which is periodic along y-direction and finite in x-direction. (e) Zak phase of the first three band of BPN PhC in armchair direction. (f) Photonic band structure for the armchair ribbon. (g) The schematic of supercell used for determining cross edge states, which is periodic along $\mathbf{T}_3$-direction and finite in x-direction. (h) Zak phase of the first three band of BPN PhC in $\mathbf{T}_3$-direction. (i) Photonic band structure for the cross ribbon. The orange lines indicate topological edge states.

The armchair ribbon is parallel to y-direction with $\mathbf{\Gamma}_{\|} = \left(0, \frac{2\pi}{a_T}\right)$, $\mathbf{\Gamma}_{\perp} = \left(\frac{2\pi}{a_0}, 0\right)$, then we choose $k_{\|} = \left(0, -\frac{\pi}{a_T}\right) \rightarrow \left(0, \frac{\pi}{a_T}\right)$, $k_{\perp} = \left(-\frac{\pi}{a_0}, 0\right) \rightarrow \left(\frac{\pi}{a_0}, 0\right)$. Figure 2.5(d) is the schematic of armchair ribbon structure. Contrary to zigzag ribbon, this armchair ribbon structure is periodic along y-direction and finite in x-direction. Therefore, periodic boundary condition is applied in y-direction and PMC boundary condition is applied in x-direction. Zak phase in y-direction is shown in Fig. 2.5(e). Band 1 and 3 are topologically non-trivial because Zak phase is π. The value of Zak phase for the 2nd band is 0. Total Zak phase for the first 3 bands is 0. So, the complete band gap between the 3rd and the 4th band becomes topologically trivial. Figure 2.5(f) is photonic band structure for armchair ribbon. There is no topological edge states in the complete band gap which is consistent with Zak phase calculation. Similar to zigzag ribbon, topological edge states should appear in between the band 1 and 2. However, because of the overlapping frequency of these two bands, we can not distinguish the topological edge states by numerical calculation.

We put $a_c = \sqrt{a_0^2 + a_T^2}$, which is the periodic constant of BPN PhC in $\mathbf{T}_3$ direction.

Two orthogonal vectors which form 2D Brillouin zone are $\mathbf{\Gamma}_{\parallel} = \frac{2\pi}{a_0}\left(\frac{4+2\sqrt{3}}{13+2\sqrt{3}}, \frac{3+3\sqrt{3}}{13+2\sqrt{3}}\right)$, $\mathbf{\Gamma}_{\perp} = \frac{2\pi}{a_0}\left(1, -\frac{1+\sqrt{3}}{3}\right)$. Then we choose discrete k-points for Zak phase calculation are $k_{\parallel} = -\frac{\pi}{a_0}\left(\frac{4+2\sqrt{3}}{13+2\sqrt{3}}, \frac{3+3\sqrt{3}}{13+2\sqrt{3}}\right) \rightarrow \frac{\pi}{a_0}\left(\frac{4+2\sqrt{3}}{13+2\sqrt{3}}, \frac{3+3\sqrt{3}}{13+2\sqrt{3}}\right)$ and $k_{\perp} = -\frac{\pi}{a_0}\left(1, -\frac{1+\sqrt{3}}{3}\right) \rightarrow \frac{\pi}{a_0}\left(1, -\frac{1+\sqrt{3}}{3}\right)$. In Fig. 2.5(g), we show the cross ribbon structure, which is periodic along $\mathbf{T}_3$ direction. The two edges which are parallel to x-direction have periodic boundary condition. Two other edges is applied PMC boundary condition.

Zak phase for the first three band of BPN PhC in the cross-direction are shown in Fig. 2.5(h). Here we put $k_{c\parallel} = \frac{\pi}{a_0}\left(\frac{4+2\sqrt{3}}{13+2\sqrt{3}}\right)$. While Zak phase for the first two band is 0, it is π for the third band. The complete band gap becomes topologically non-trivial because total Zak phase of bands below it is π. Photonic band structure for cross ribbon is shown in Fig. 2.5(i). The orange line indicates topological edge states, which are consistent with Zak phase calculation in Fig. 2.5(g). This topological edge states is in a complete band gap and isolated from other states.

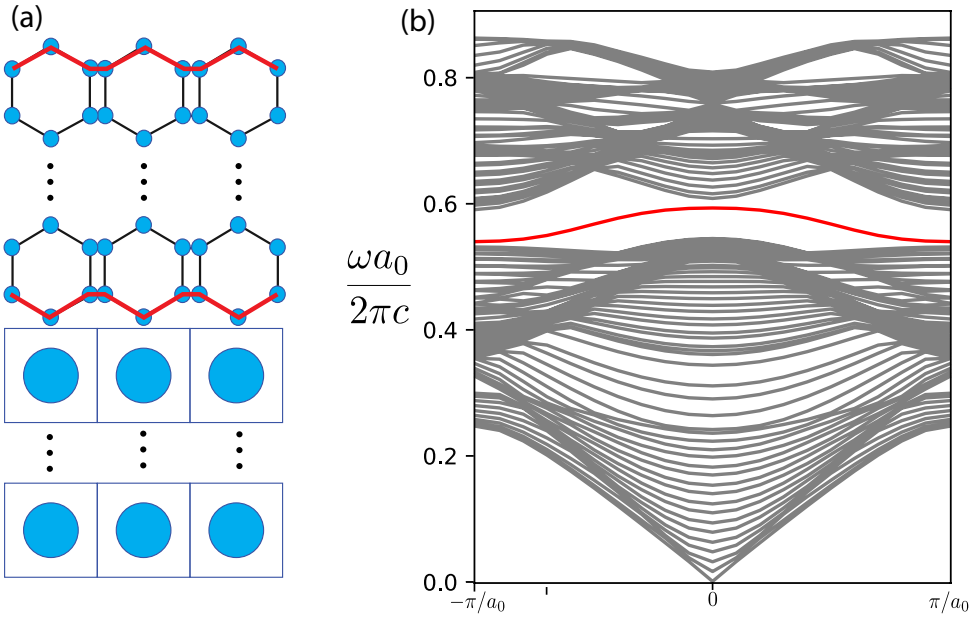

FIGURE 2.6: (a) A schematic of a supercell containing interface between zigzag ribbon and a trivial PhC. (b) Photonic band structure for the supercell in (a). Red lines denote topological edge states, where EM wave is highly localized at the interface between zigzag ribbon and the trivial PhC.

To confirm the existence of topological zigzag edge states at all k points, we create another structure containing BPN PhC and a trivial PhC. The trivial PhC has a band gap at the same frequency range as the band gap of BPN PhC. Fig. 2.6(a) is the schematic of a supercell, which has an interface between zigzag ribbon and the trivial PhC. Applying periodic boundary condition in both x and y directions, we calculate and obtain photonic band structure for the supcell as shown in Fig. 2.6(b). The red lines denote topological edge states, where EM wave is localized at the interface. These edge states emerge at all k points in the first BZ and double degenerate because the supercell contains 2 interfaces.

2.3.3 Topological Corner States

In this section, we examine the localization of EM wave at different corner structures in BPN PhC lattice.

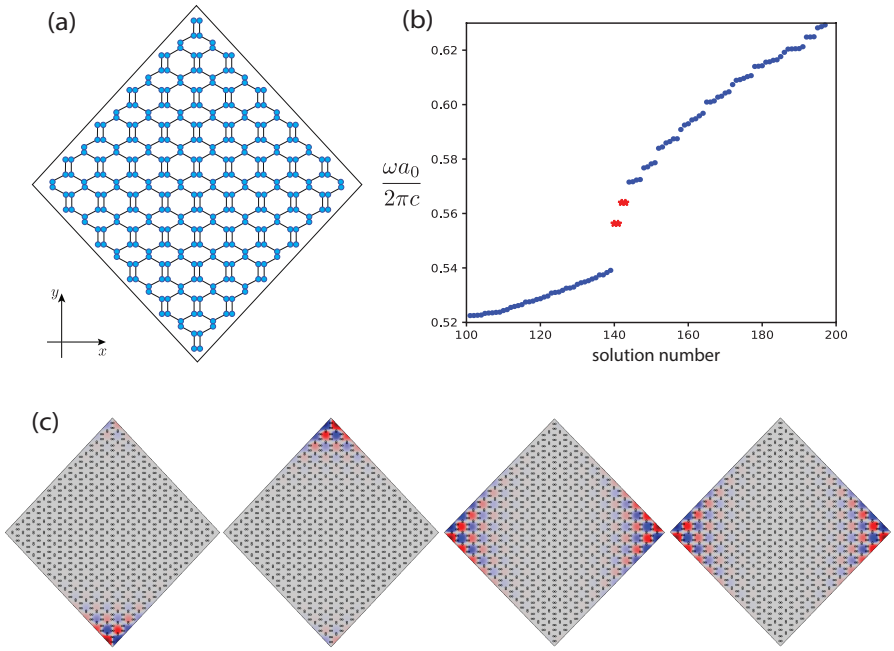

FIGURE 2.7: (a) The schematic of corner structure which are formed by cross ribbons. (b) Frequency spectrum for BPN PhC corner structure in (a). The red dots indicate topological corner states. The frequency range of corner states is in the complete gap region. (c) Field profile for four corner states from low to high frequencies. These profiles show that topological corner states is isolated from bulk and edge states.

In Fig. 2.7(a), we show a rhombus shape of BPN PhC. Four outer boundaries have cross ribbon structure. The two opposite corners have the same structure and they are different from two other ones. The PMC boundary condition is applied for all edges in this rhombus structure.

Fig. 2.7(b) is the frequency spectrum for the PhC structure in Fig. 2.7(a). In the complete band gap of BPN PhC, there are four isolated states labeled by red dots. The states are corner states where EM wave is highly localized at the corners and exponentially decay as shown in Fig. 2.7(c). Two ribbons which form the corner are topologically non-trivial because of π Zak phase. Therefore, these corner states are really topological corner states similar to the condition of topological corner states observed in other topological PhCs [28].

From this point of view, we also construct and examine another corner structure that formed by zigzag and cross ribbon as shown in Fig. 2.8. Left and right edges are cross ribbons, upper and lower edges are zigzag ribbons. Because both zigzag and cross ribbons are topologically non-trivial at the complete band gap, the topological corner states are expected in this structure. Figure 2.8(a) is photonic band structure for corner structure containing zigzag and cross ribbons. The states below band gap (labeled by red stars) are zigzag edge states, the states above band gap (labeled by green stars) are cross edge states. Their field distributions are shown in Fig. 2.8(b). From the left side to the right side, the frequencies are increasing. This is consistent with the frequency range of zigzag and cross ribbon edge states shown in Fig. 2.5(f)

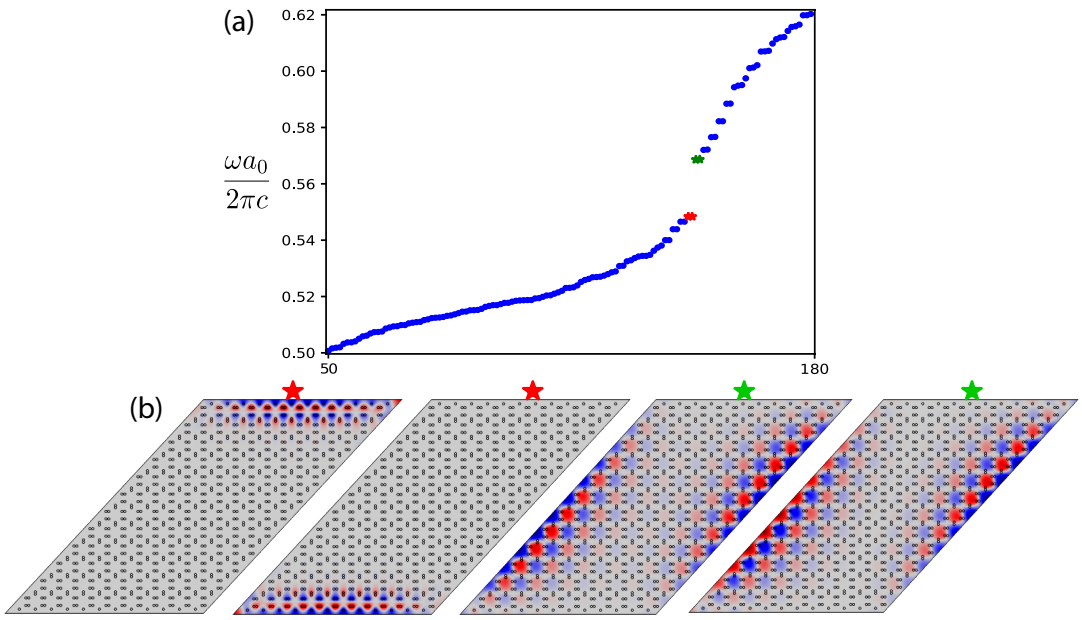

FIGURE 2.8: (a) Photonic band structure for the corner structure formed by zigzag and cross ribbons. Red stars indicate zigzag ribbon edge states, green stars denote cross ribbon edge states. (b) The field distribution for the states labeled in red and green from low to high frequencies.

and (i). Corner states do not exist in this structure. The reason for this absence is that the frequency range of armchair and cross ribbons edge states are totally different, EM wave can not be confined at the boundary between two edges.

Other corner structures involved in armchair ribbon such as corners between zigzag and armchair ribbons or corners between armchair and cross ribbons can also be constructed. However, topological corner states do not exist in these structures due to the trivial properties in the complete band gap of armchair ribbon.

2.4 Summary and Discussion

In this chapter, we have explained about the topological band theory and the topological invariants. Then, we numerically studied EM wave in BPN PhC structure by using FDM and FEM. The original photonic analog of BPN network has no band gap. Linear dispersion of frequency can be observed in this PhC. When the structure is modified by increasing the distance from each rod to the center of unit cell, a complete band gap opens in between band 3 and band 4. We examine topological properties of BPN PhC in this band gap by numerically calculating Zak phase in several directions. The topological edge states are observed in the photonic band gap due to the non-trivial Zak phase, which are localized at the edge of zigzag and cross ribbon structures. The Zak phase calculation method will work for not only photonic systems but also any other 2D systems. The higher order topology as corner states are found at the corner formed by two cross ribbons because of non-zero product of Zak phase in two directions. We also point out that the topological corner states emerge only when topological edge states of two ribbon structures which form the corner are completely overlapped to each other.

Compared with graphene-like PhCs, the topological edge states in BPN-like structure can be found without breaking the symmetry of the crystals. Similar to valley

PhCs, the Z-shape waveguide, resulted from topological edge states of cross ribbons, is also a potential application. Our results suggest a possible way to design in-gap topological waveguide and topological confinement of EM wave.

Chapter 3

Simple Cubic Photonic Crystal

This Chapter is spent for examining higher order topological states in a 3D PhC having complete photonic band gap by numerical method. The 3D structure follows simple cubic lattice. We calculate Zak phase of this PhC and make the relation of Zak phase to the topological surface states observed in the gap. Then, the explanation of hinge states based on Zak phase will be pointed out.

3.1 Simple Cubic Lattice

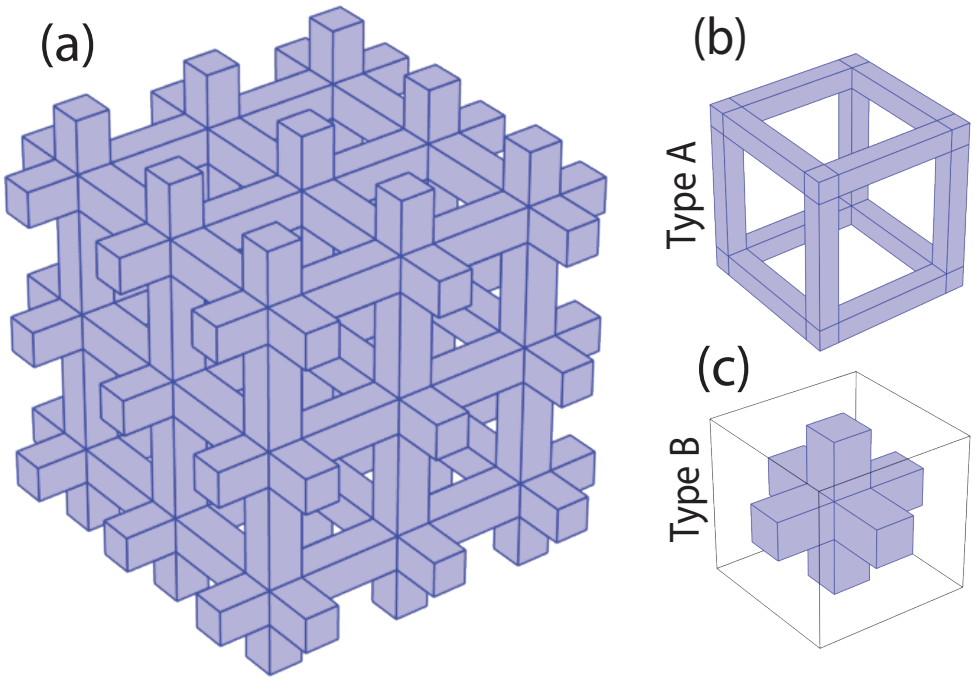

FIGURE 3.1: (a) A schematic of simple cubic lattice, which consists of dielectric blocks (blue color) and air. (b) Unit cell type A. (c) Unit cell type B, obtained by shifting unit cell type A one half of a period in all three directions.

We start from a simple cubic structure as shown in Fig. 3.1(a), which consists of dielectric blocks and air. Lattice constant is a_0 in all three directions. The cross section size of each dielectric blocks is $0.25a_0 \times 0.25a_0$. Refractive index of blocks is 3.5. There are many ways to define unit cell for this structure. Here we point out two types of unit cell which are highly symmetric: unit cell type A as shown in Fig. 3.1(b) and unit cell type B as shown in Fig. 3.1(c). One of these two unit cell can be obtained by shifting the origin of the other unit cell one half of the lattice constant.

Both inversion symmetry (IS) and time-reversal symmetry (TRS) are preserved in this simple cubic PhC.

3.2 Photonic Band Structure and Polarization

Since the two types of unit cell represent the same structure. Photonic band structure calculated by using unit cell type A and type B will be identical as shown in Fig. 3.2(b). In this photonic band structure, a complete band gap is observed in between band 2 and band 3, around the normalized frequency 0.4, which is denoted by the shaded region. Two lowest modes are colored in blue and red, respectively. These two modes are completely degenerate in $\Gamma - X$ and $\Gamma - R$ regions. In this study, we only focus on the two lowest modes and the complete band gap above these two modes.

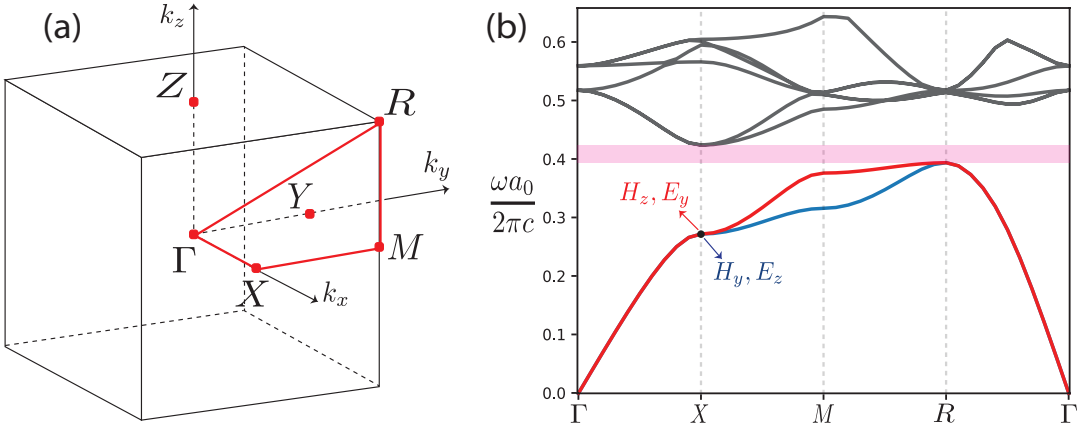

FIGURE 3.2: (a) The first BZ of simple cubic lattice with high symmetric points. The red line denotes the high symmetric path that the photonic band structure will be calculated. (b) Photonic band structure of simple cubic PhC. Two lowest modes are labeled in blue and red, respectively. A complete band gap (shaded region) is found around normalized frequency 0.4.

By checking the polarization of the two lowest modes, we found that they have orthogonal polarization at all k points in the first BZ. Especially, at the k points where $k_z = 0$, the two modes are well separated into in-plane and out-of-plane polarization. For example, At X point, the magnetic field of blue mode has only y component and the electric field has only z component. For the red mode, magnetic field has only z component and electric field has only y component. Similarly, at Y point, the blue mode has H_x and E_z components, the red mode has H_z and E_x components. At M point, the blue mode has H_x, H_y and E_z components, where Hx and H_y have almost equal amplitude. The red mode has H_z and E_x, E_y components, where amplitude of E_x and E_y is almost the same. In general, at the k points where $k_z = 0$, the lowest mode, which is colored in blue, has mainly H_x, H_y, E_z components. The second lowest mode, colored in red, has mainly H_z, E_x, E_y components. If considering for magnetic field separately, the blue mode has in-plane polarization and red mode has out-of-plane polarization. This is opposite for electric field. The polarization of bulk modes will be inherited by the surface and hinge modes in the following sections.

Figure 3.3 represents field distribution at X point of two types of unit cell. The field distribution of unit cell type A is shown on the left side. The first row is for the

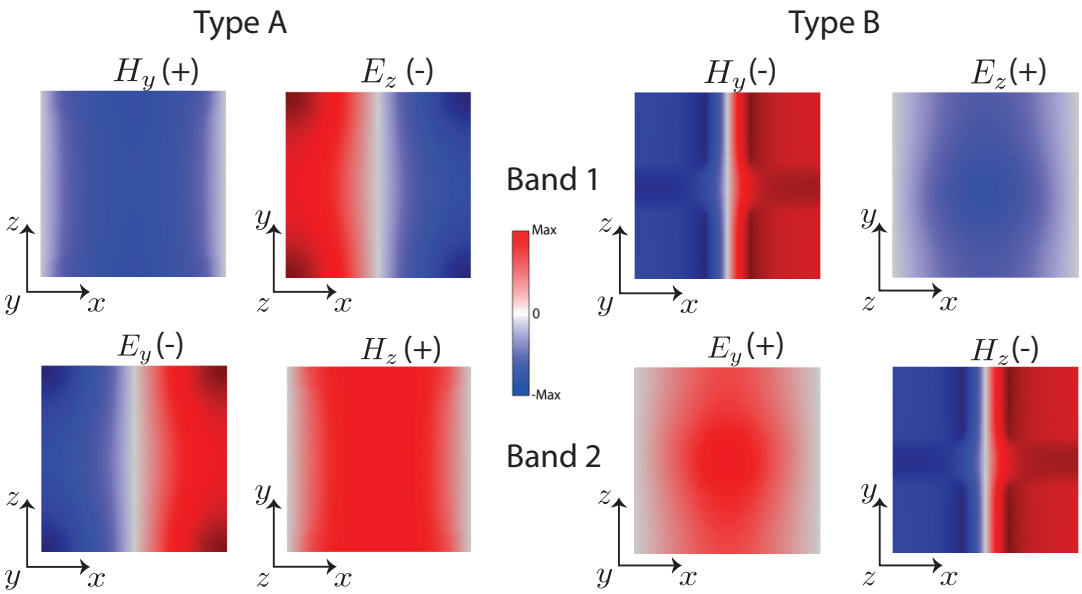

FIGURE 3.3: Field distribution at X point of unit cell type A (left side) and unit cell type B (right side). The first row present for the lowest mode (band 1). The second row present for the second lowest mode (band 2). The $+/-$ sign in the parenthesis represent for parity of each field distribution.

lowest mode (band 1), the second row is for the second lowest mode (band 2). The $+/-$ sign in the parenthesis represent for parity $+1/-1$ of each field distribution. It is easily seen that parity of magnetic field is $+1$ and that of electric field is -1. On the right side, field distribution and the corresponding parity of unit cell type B are presented. Contrary to unit cell type A, parity is -1 for magnetic field and $+1$ for electric field.

3.3 Numerical Calculation of Zak Phase

In this section, we perform the numerical calculation of Zak phase in 3D PhCs. As written in section 2.2, Berry phase of n-th band is obtained by the closed path integral

$$\gamma^n = \oint_{1^{st}BZ} \mathbf{A}^n(\mathbf{k})\, d\mathbf{k}, \tag{3.1}$$

where $\mathbf{A}^n(\mathbf{k})$ is known as Berry connection and defined as

$$\mathbf{A}^n(\mathbf{k}) = i\left\langle u^n_{\mathbf{k}}(\mathbf{r}) \middle| \nabla_{\mathbf{k}} \middle| u^n_{\mathbf{k}}(\mathbf{r}) \right\rangle. \tag{3.2}$$

Here $u^n_{\mathbf{k}}(\mathbf{r})$ is periodic part of Bloch wave function.

Since Zak phase is an 1D integral in the first Brillouin zone, in any 3D systems, it will depend on a 2D surface that is perpendicular to the integral direction. In this section, we will show the calculation for Zak phase in $k_y k_z$ surface, it means that the integral will be taken along k_x direction. The method can be applied for calculating Zak phase on other surfaces such as $k_x k_y$ and $k_x k_z$ surfaces. Equation (3.1) can be rewritten as

$$Z^n(k_y, k_z) = \int_{-\pi}^{\pi} \left\langle u^n_{k_x,k_y,k_z}(\mathbf{r}) \middle| i\partial_{k_x} \middle| u^n_{k_x,k_y,k_z}(\mathbf{r}) \right\rangle dk_x. \tag{3.3}$$

The integral of Berry connection over $-\pi \leq k_x \leq \pi$ can be obtained by dividing the first Brillouin zone into small segments then approximating the integral by summing the contributions of each segment. For example, if the k_x direction in the first Brillouin zone is divided into N_0 segments ($\delta k_x = \frac{2\pi}{N_0 a}$), in each small segment from k_i to k_{i+1} ($i = 1, ..., N_0$), the Zak phase $Z^n(k_i)$ is obtained by

$$e^{-iZ^n(k_i)} = \langle u^n_{k_i} | u^n_{k_{i+1}} \rangle , \tag{3.4}$$

In the above equation, we have used the following relation:

$$\begin{aligned} \langle u^n_{k_i} | u^n_{k_{i+1}} \rangle &= 1 + \langle u^n_{k_i} | \left(|u^n_{k_{i+1}}\rangle - |u^n_{k_i}\rangle \right) \\ &= 1 - i^2 \frac{\langle u^n_{k_i} | \left(|u^n_{k_{i+1}}\rangle - |u^n_{k_i}\rangle \right)}{\delta k_x} \delta k_x \\ &= 1 - iZ^n(k_i)\delta k_x \\ &\approx e^{-iZ^n(k_i)\delta k_x}, \end{aligned} \tag{3.5}$$

The total Zak phase is given by the summation of all $Z^n(k_i)$ with $i = 1, ..., N_0$, i.e.,

$$\begin{aligned} Z^n &= \sum_{i=1}^{N_0} Z^n(k_i) \\ &= \sum_{i=1}^{N_0} \left[- \operatorname{Im} \left(\log \langle u^n_{k_i} | u^n_{k_{i+1}} \rangle \right) \right] \\ &= - \operatorname{Im} \left(\log \prod_{i=1}^{N_0} \langle u^n_{k_i} | u^n_{k_{i+1}} \rangle \right). \end{aligned} \tag{3.6}$$

From the above expression, we can approximate Eq. (3.3) by the following discrete equation

$$Z^n \left(k_j, k_l \right) = - \operatorname{Im} \left(\log \prod_{i=1}^{N_0} \langle u^n_{k_i, k_j, k_l} (\mathbf{r}) \, | u^n_{k_{i+1}, k_j, k_l} (\mathbf{r}) \rangle \right). \tag{3.7}$$

where k_i, k_j, k_l are the discrete k-points of k_x, k_y, k_z directions, respectively. Equation (3.7) indicates that Zak phase can be calculated for each $\left(k_j, k_l \right)$ point on the $k_y k_z$ surface. It is noted that Eq. (3.7) can be used if a band is isolated.

For a group of N connected bands, the scalar products are replaced by overlap matrices as shown in Eq. (2.11), where $\mathbf{k}_1$ and $\mathbf{k}_2$ containing three components: $\mathbf{k}_1 = (k_i, k_j, k_l)$ and $\mathbf{k}_2 = (k_{i+1}, k_j, k_l)$. Total Berry connection (in matrix form) for k_x direction can be obtained by

$$\hat{S} \left(k_j, k_l \right) = \prod_{i=1}^{N_0} S_{(k_i, k_j, k_l)(k_{i+1}, k_j, k_l)}. \tag{3.8}$$

To evaluate Zak phase for each band, we need the eigenvalues of the above Berry connection matrix. Then Zak phase for n-th subband is given by

$$Z^n \left(k_j, k_l \right) = - \operatorname{Im} \log \left(s^n \right), \tag{3.9}$$

where s^n is n-th eigenvalue of matrix $\hat{S} \left(k_j, k_l \right)$.

In our simple cubic PhC, two bands below the complete gap are connected by the degeneracies in $\Gamma - X$ and $\Gamma - R$ lines. Hence, we use overlap matrices to evaluate

Zak phase for these two bands. In Fig. 3.4(a), left panel is the schematic of unit cell type 1, middle and right panels are numerical results of its Zak phase on $k_y k_z$ surface for band 1 and band 2, respectively. k_y and k_z axis are taken in the first BZ $-\pi/a \leq k_y, k_z \leq \pi/a$. Yellow and purple colors indicate the π and 0 values of Zak phase. Similarly, Fig. 3.4(b) is the schematic of unit cell type 2 (left), Zak phase on $k_y k_z$ surface of the first band (middle), Zak phase on $k_y k_z$ surface of the second band (right).

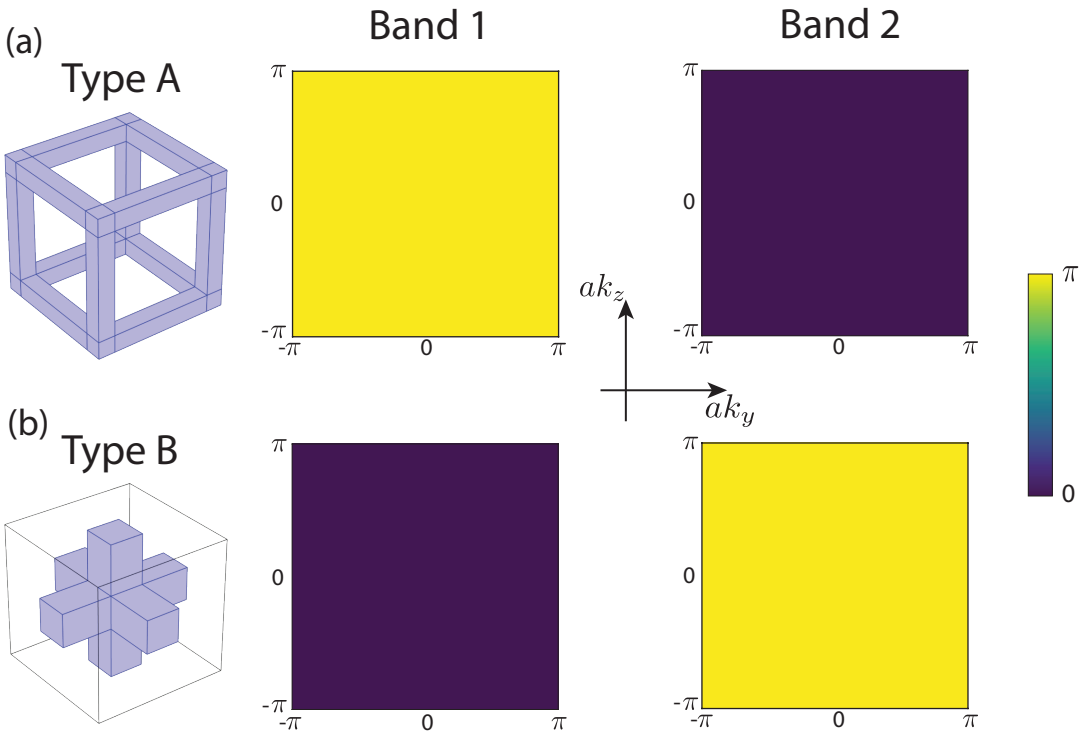

FIGURE 3.4: Numerical calculation of Zak phase on $k_y k_z$ surface of 3D simple cubic PhC. (a) Unit cell type 1 (left), Zak phase of the first band (middle), Zak phase of the second band (right). (b) Unit cell type 2 (left), Zak phase of the first band (middle), Zak phase of the second band (right). In both (a) and (b), yellow and purple colors indicate that Zak phase is π and 0, respectively.

For the unit cell type A, Zak phase is π for the first band and 0 for the second band at all points on $k_y k_z$ surface. For the unit cell type B, the value is 0 for the first and and π for the second band at all points on $k_y k_z$ surface. These results are consistent with the parity of the z component of EM waves at X point shown in the Fig. 3.3. π or 0 values of Zak phase means that the photonic band is topological or trivial, respectively. At each band, these two kinds of unit cell have opposite topological properties leading to the localization of EM field at the boundary between them.

3.4 Topological Interface States

In this section, we examine an interface structure between two types of unit cell. Figure 3.5(a) is the schematic of a supercell containing 8 unit cells type A and 8 unit cells type B. Size of this supercell is $16a_0$, a_0, a_0 in x, y and z directions, respectively. The corresponding first BZ of this super cell is shown in Fig. 3.5(b). To calculate

projected photonic band structure, FEM is used and periodic boundary condition is applied in all three direction.

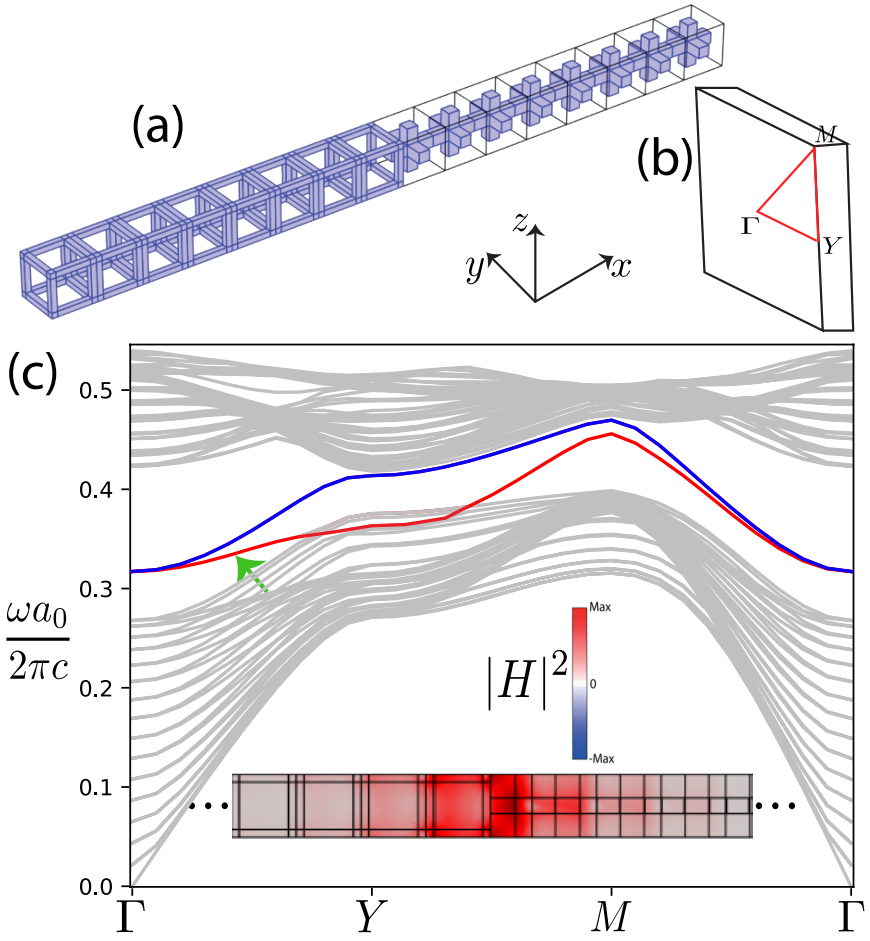

FIGURE 3.5: (a) A schematic of a supercell of interface structure. It consists of 8 unit cells type A and 8 unit cells type B. (b) The corresponding first BZ of the supercell in (a). (c) Projected photonic band structure of supercell. Grey lines denote bulk states, red lines indicate interface states. The inset shows field distribution of the interface state labeled by green arrow.

The calculation results for projected photonic band structure is shown in Fig. 3.5(c). Grey lines indicate bulk states. Red and blue lines denote topological interface states, where EM wave is highly localized at the interface and exponentially decays. They are doubly degenerate because there are two equivalent interfaces in a supercell. The inset shows magnetic field distribution of the interface state labeled by green arrow (the top view from z direction).

Now we discuss about polarization of these interface states. The magnetic field of red mode has mainly x component. It means that this modes has linear polarization in the direction perpendicular to the interface plane (out-of-plane polarization). On the other hand, the magnetic field of blue mode has mainly H_y and H_z components, which means that this mode has linear polarization in the direction paralleled to the interface (in-plane polarization).

From the calculation of Zak phase in the previous section and the discussion of polarization, we find that the red interface modes are derived from the second lowest bulk modes (red bulk modes). They are the results of π difference in Zak phase of band 2 between two types of unit cell. Similarly, the blue interface modes

are derived from the lowest bulk modes (blue bulk mode), which are also due to the π difference in Zak phase of band 1 between two types of unit cell. These topological interface states are known as the first order topological states, being robust against the defect and disorder.

3.5 Topological Hinge States

Since the x and y directions are equivalent in both unit cell type A and type B, Zak phase on k_xk_z surface are the same as Zak phase on k_yk_z surface. Therefore, the second order topological states as hinge states are expected to be formed at the boundary between two interfaces xz and yz.

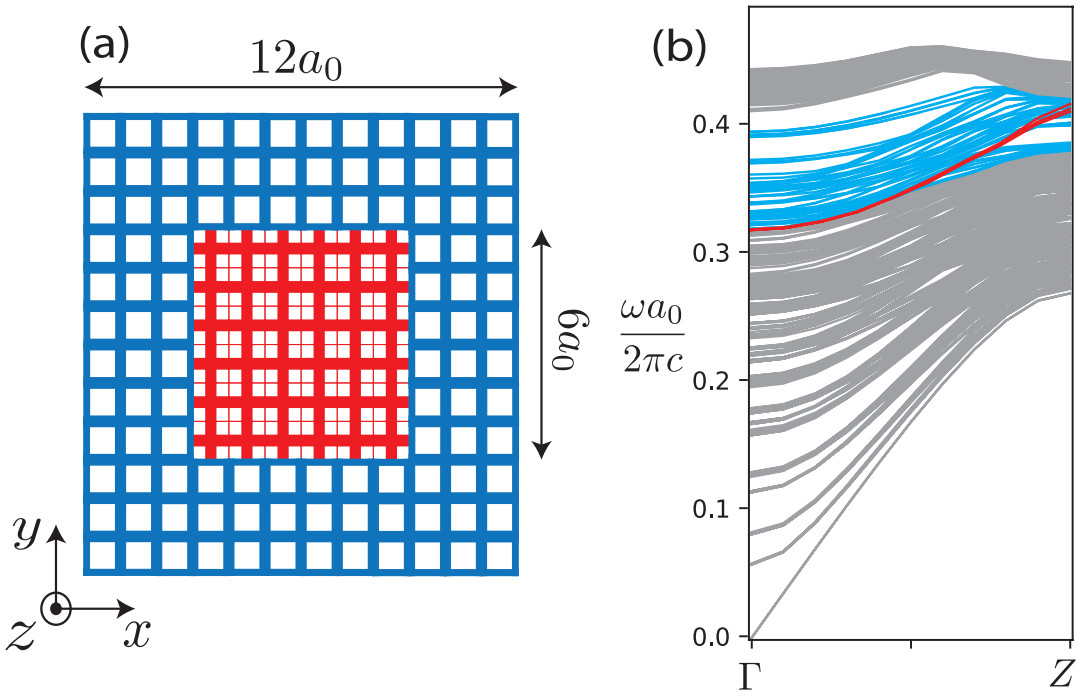

FIGURE 3.6: (a) Schematic top view of supercell containing 4 hinges. Blue color indicates unit cell A, red color indicates unit cell B. (b) Photonic band structure for supercell in (a). Bulk, interface and hinge states are colored in grey, blue and red, respectively.

To examine the dispersion of hinge states, we calculate photonic band structure for the super cell in Fig. 3.6(a) by FEM. In the center of the supercell, 6×6 unit cells type B are embedded. They are surrounded by unit cells type A. The supercell size is $12a_0$, $12a_0$, a_0 in x, y and z directions, respectively. Figure 3.6(b) is the projected photonic band structure for the supercell. We label the bulk, interface and hinge states in grey, blue and red color, respectively. The hinge states are four-times degenerate because the supercell contains 4 equivalent hinges.

Figure 3.7 is the spatial field distribution of hinge states at normalized frequency 0.32. At each state, EM wave is highly localized at the hinge and exponentially decays. However, bulk and interface states are slightly mixed with hinge states. This is because the frequency range of bulk, interface and hinge states are overlapped. These localized hinge states have mainly H_x and H_y components with approximately the same amplitude. From this numerical result, we can confirm the existence of second order topological states as hinge states in 3D simple cubic PhC.

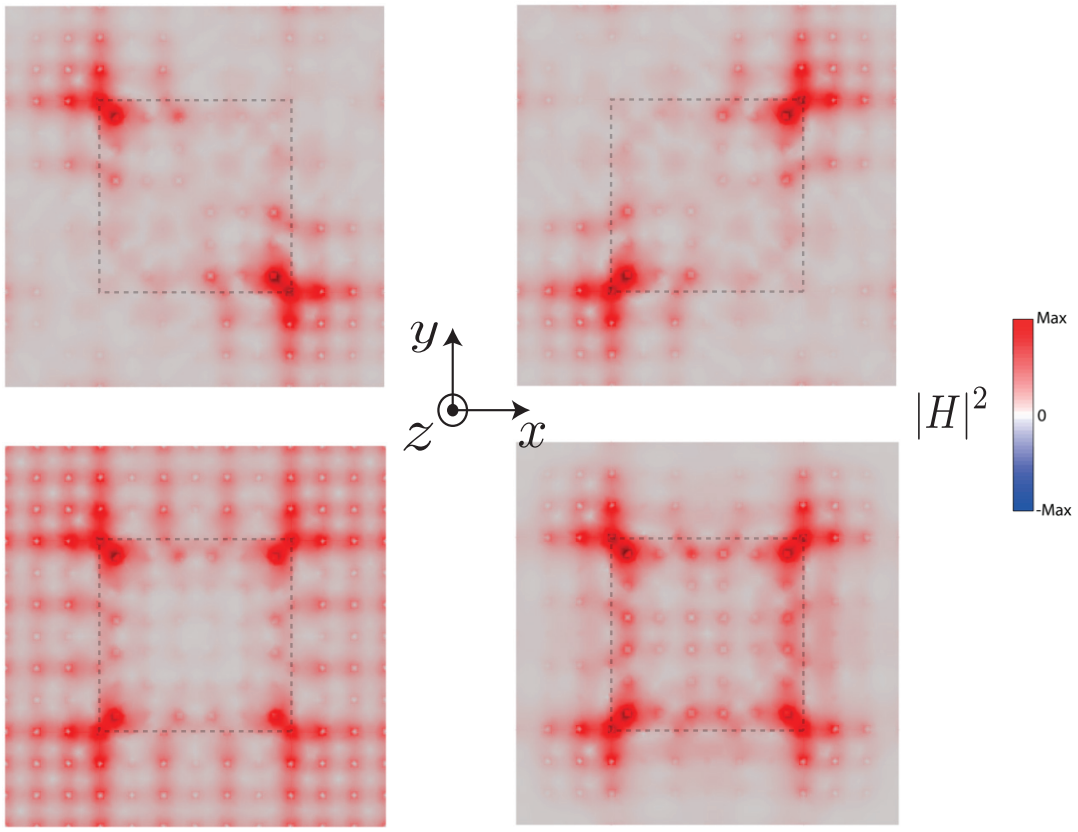

FIGURE 3.7: Magnetic field distribution of hinge states at normalized frequency 0.32. The dash lines denote the interface between two type of unit cell.

3.6 Summary and Discussion

In this Chapter, we have numerically studied EM wave states in 3D simple cubic PhC by using FEM and FDM. The system contains dielectric blocks and air. The IS and TRS are preserved in this structure. We observed a complete band gap in between the second and the third band, which is around normalized frequency 0.41. Below the complete band gap, there are two photonic bands, which are completely degenerate in $\Gamma - X$ and $\Gamma - R$ lines. These two bands have orthogonal polarization at all k points in the BZ.

We explained a numerical calculation method based on FDM to determine Zak phase for two lowest bands. Since the simple cubic PhC is a 3D structure, Zak phase is defined for each plane in the first BZ. The numerical results of Zak phase on $k_y k_z$ plane are presented. For unit cell type A, band 1 is topological due to the π value of Zak phase. The second band is trivial because Zak phase is 0. On the contrary, unit cell type B has 0 Zak phase for the first band and π Zak phase for the second band.

The topological interface states are observed in the complete band gap due to the π difference in Zak phase of each band. By checking the polarization of interface states, we found out that each interface state corresponds to a bulk state below the gap. These topological interface states are the first order topological states in 3D simple cubic PhC.

Since x and y directions are equivalent in this simple cubic structure, Zak phase on $k_x k_z$ plane and on $k_y k_z$ plane are identical. Because both planes have π difference in Zak phase at each band, topological hinge states are expected to be formed at

the boundary between xz and yz plane (means hinge states in z direction). The numerical results by FEM have confirmed this existence. These topological hinge states are called sencond order topological states in 3D simple cubic PhC.

Our description of numerical calculation method for Zak phase in 3D PhC is a priori not only restricted for photonic systems, but it is also applicable for other 3D systems. The results of topological states in 3D simple cubic could be applied to 3D control of wave propagation for communication and be essential for realizing robust 3D photonic circuits.

Chapter 4

Woodpile Photonic Crystal

In this Chapter, we study EM wave propagation in 3D woodpile PhC. This structure has a large complete band gap. The first order and second order topological states are examined in this structure. Wilson loop in a photonic system without IS will be presented. The selection rule for hinge states will also be pointed out based on Wilson loop.

4.1 Woodpile Lattice

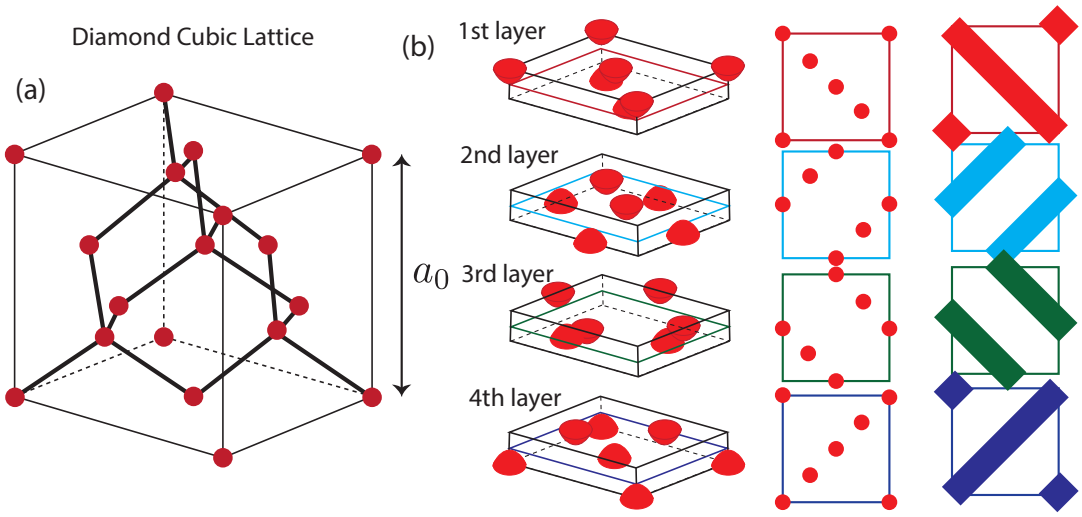

FIGURE 4.1: (a) A schematic of diamond cubic lattice. (b) Separated four layers of diamond cubic lattice which have the same thickness (left). The top view of each layer (middle). The arrangement of dielectric blocks in each layer, which follow the top view (right). Different colors indicate different layer.

Figure 4.1(a) is the schematic of a unit cell of diamond cubic lattice. Lattice size is a_0, red dots represent for atoms. Woodpile PhC is inspired from the diamond cubic lattice by dividing diamond cubic lattice into 4 layers, which have the same thickness, as shown in Fig. 4.1(b) (left panels). Then, by looking at the top view of each layer (middle panels), the dielectric blocks are arranged following the projected position of atoms onto layers (right panels). The different colors of blocks indicate different layers. The thickness of each block is $0.25a_0$, their width is $0.198a_0$. Refractive index of dielectric blocks is 3.6.

A conventional unit cell of woodpile PhC is a cubic containing 4 layers. The top view is shown in Fig. 4.2(a). By repeating this conventional unit cell infinitely in all x, y and z directions, we obtain the woodpile PhC. However, the diamond

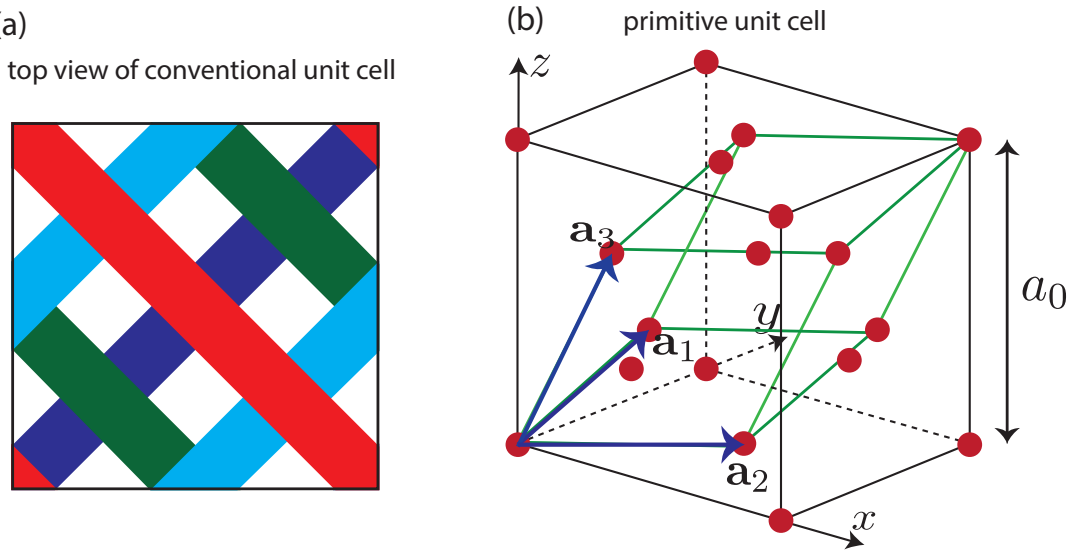

FIGURE 4.2: (a) A schematic top view of conventional unit cell of woodpile PhC. (b) A schematic of conventional unit cell (green lines). $\mathbf{a}_1$, $\mathbf{a}_2$, $\mathbf{a}_3$ are 3 primitive lattice vectors of primitive unit cell.

cubic lattice has a primitive unit cell (smallest unit cell) labeled by green lines in Fig. 4.2(b). Therefore, we can also define the primitive unit cell of woodpile PhC in the same way as primitive unit cell of diamond cubic lattice. Three primitive vectors of primitive unit cell are

$$\begin{aligned} \mathbf{a}_1 &= \left(\frac{1}{2}, 0, \frac{1}{2}\right) a_0, \\ \mathbf{a}_2 &= \left(\frac{1}{2}, \frac{1}{2}, 0\right) a_0, \\ \mathbf{a}_3 &= \left(0, \frac{1}{2}, \frac{1}{2}\right) a_0. \end{aligned} \tag{4.1}$$

In the following sections of this chapter, we will use both conventional and primitive unit cells to examine woodpile PhC.

4.2 Photonic Band Structure and the Symmetry of Lattice

Photonic band structure for woodpile PhC is calculated by using FEM. In Fig. 4.3(a), we give a schematic of the first BZ of conventional unit cell. This BZ is a cubic and similar to the BZ of simple cubic PhC. The red path indicate irreducible BZ. Photonic band structure obtained by using conventional unit cell are shown in Fig. 4.3(b). A complete band gap is observed around normalized frequency 0.38. This gap is much larger than the complete band gap in simple cubic PhC. Below the band gap, there are 8 photonic bands, which are connected by the degenerate points. Figure 4.3(c) is the first BZ of primitive unit cell. Three primitive vectors in reciprocal space of

primitive unit cell are

$$\begin{aligned}\mathbf{b}_1 &= \frac{2\pi}{a_0}(1,-1,1)\,,\\ \mathbf{b}_2 &= \frac{2\pi}{a_0}(1,1,-1)\,,\\ \mathbf{b}_3 &= \frac{2\pi}{a_0}(-1,1,1)\,.\end{aligned} \tag{4.2}$$

The red path is irreducible BZ. Photonic band structure calculated by using primitive unit cell is shown in Fig. 4.3(d). A complete band gap is also observed in the same frequency range as in Fig. 4.3(b). Below this band gap, there are only 2 photonic bands, while it has 8 bands in conventional unit cell. This is because conventional unit cell is four times bigger than primitive unit cell.

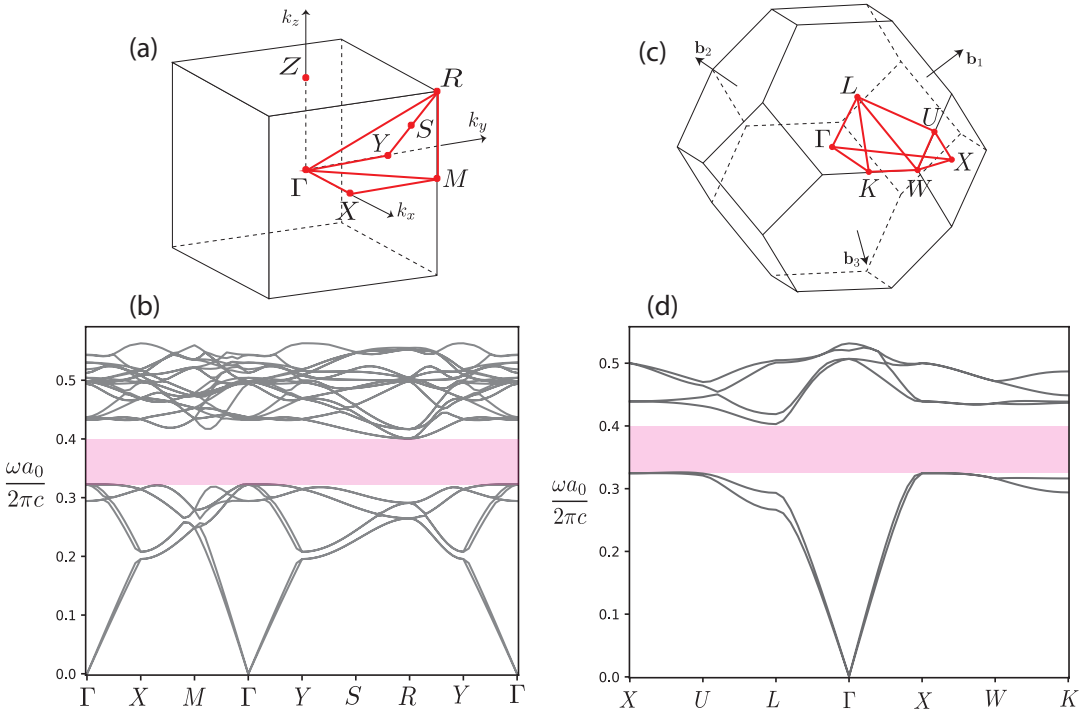

FIGURE 4.3: (a) The first BZ of conventional unit cell. The red path indicates irreducible BZ. (b) Photonic band structure of woodpile PhC, calculated by using conventional unit cell. A large complete band gap is observed around the normalized frequency 0.38. (c) The first BZ of primitive unit cell. The red path indicates irreducible BZ. (d) Photonic band structure of woodpile PhC, calculated by using primitive unit cell. A complete band gap is observed in the same frequency range as in (b).

This woodpile PhC is examine in the presence of TRS. However, even though the mirror symmetry is still preserved, the IS is broken in this structure. Therefore, Zak phase of this PhC will not be quantized to π and 0 [26]. In this case, the integral of Berry connection over one direction in the first BZ will take the value from $-\pi$ to π, the set of all values on a plane in 3D systems is called Wilson loop. By determining the evolution of Wilson loop, we can find out other topological invariants of 3D PhC.

4.3 Wilson Loop on an Arbitrary Plane

In this section, we will explain the numerical method for calculating Wilson loop on arbitrary planes in 3D Woodpile PhC. Similar to Zak phase, Wilson loop is also defined for each photonic band. For woodpile PhC, if the conventional unit cell is used to calculate Wilson loop, the situation will become similar to simple cubic lattice, where the first BZ is a cubic. However, in this case, because there are 8 connected photonic bands below the complete band gap, the overlap matrix in Eq. (2.11) will be an 8×8 matrix. The numerical code will be very time-consuming and complicated. Therefore, we will calculate Wilson loop by using primitive unit cell.

Here we note that three primitive vectors in real space are not perpendicular to each other. Three vectors in reciprocal space are also not perpendicular to each other, the first BZ is not a cubic or rectangular. Equation (3.3) can not be calculated in the normal way. To generalize the Zak phase calculation of 3D woodpile PhC to any arbitrary plane, the integral Eq. (3.3) should be taken on a volume of 3D BZ in the direction that is transverse to the definite plane. In particular, if the arbitrary 2D plane in a 3D woodpile PhC is assumed to be invariant under translation in two directions by two vectors $\mathbf{T}_1$ and $\mathbf{T}_2$. Their corresponding vectors in reciprocal space are $\mathbf{\Gamma}_1$ and $\mathbf{\Gamma}_2$, respectively. The relationship between $\mathbf{T}$ and $\mathbf{\Gamma}$ is $\mathbf{T}_i\mathbf{\Gamma}_j = 2\pi\delta_{ij}$, where $i, j = 1, 2$. The plane that Zak phase will be calculated is formed by $\mathbf{\Gamma}_1$ and $\mathbf{\Gamma}_2$. The integral direction will be defined as a vector $\mathbf{\Gamma}_3$ that is transverse to the $(\mathbf{\Gamma}_1, \mathbf{\Gamma}_2)$ plane and satisfy the following equation

$$\mathbf{\Gamma}_1 \cdot (\mathbf{\Gamma}_2 \times \mathbf{\Gamma}_3) = \mathbf{b}_1 \cdot (\mathbf{b}_2 \times \mathbf{b}_3) \tag{4.3}$$

Equation 4.3 indicates that volume of the BZ formed by three vectors $\mathbf{\Gamma}_1, \mathbf{\Gamma}_2, \mathbf{\Gamma}_3$ is equal to the volume of the original first BZ.

Now we will explain the calculation of Wilson loop on $k_y k_z$ surface of woodpile PhC by using primitive unit cell. Figure 4.4 is the side view in yz plane of woodpile

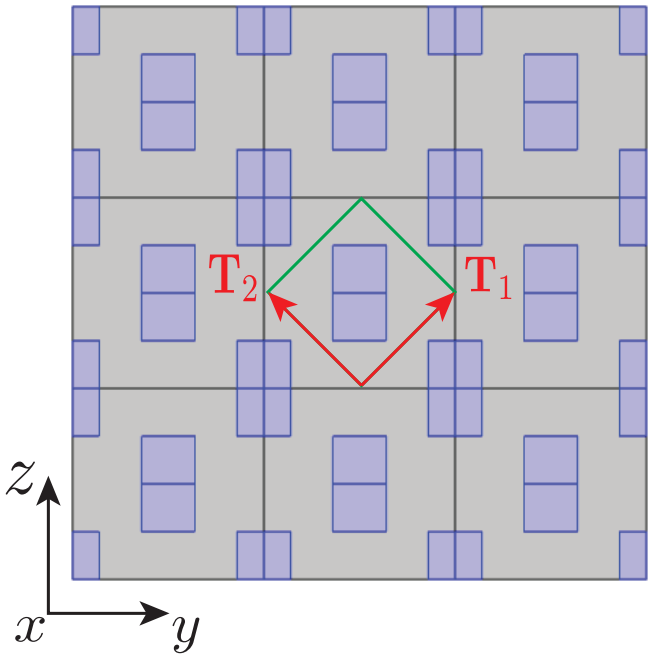

FIGURE 4.4: Side view in yz plane of woodpile PhC. $\mathbf{T}_1$ and $\mathbf{T}_2$ are two primitive vectors of yz plane (translation vectors of yz plane).

PhC. This yz plane is periodic under two translation vectors

$$\begin{aligned}\mathbf{T}_1 &= (0, \frac{1}{2}, \frac{1}{2})a_0 \\ \mathbf{T}_2 &= (0, -\frac{1}{2}, \frac{1}{2})a_0\end{aligned} \tag{4.4}$$

The corresponding vectors of $\mathbf{T}_1$ and $\mathbf{T}_2$ in reciprocal space are

$$\begin{aligned}\mathbf{\Gamma}_1 &= \frac{2\pi}{a_0}(0, 1, 1) \\ \mathbf{\Gamma}_2 &= \frac{2\pi}{a_0}(0, -1, 1)\end{aligned} \tag{4.5}$$

The third vector $\mathbf{\Gamma}_3$ is perpendicular to $\mathbf{\Gamma}_1$, $\mathbf{\Gamma}_2$ and satisfy Eq. 4.3. So $\mathbf{\Gamma}_3$ is

$$\mathbf{\Gamma}_3 = \frac{2\pi}{a_0}(2, 0, 0) \tag{4.6}$$

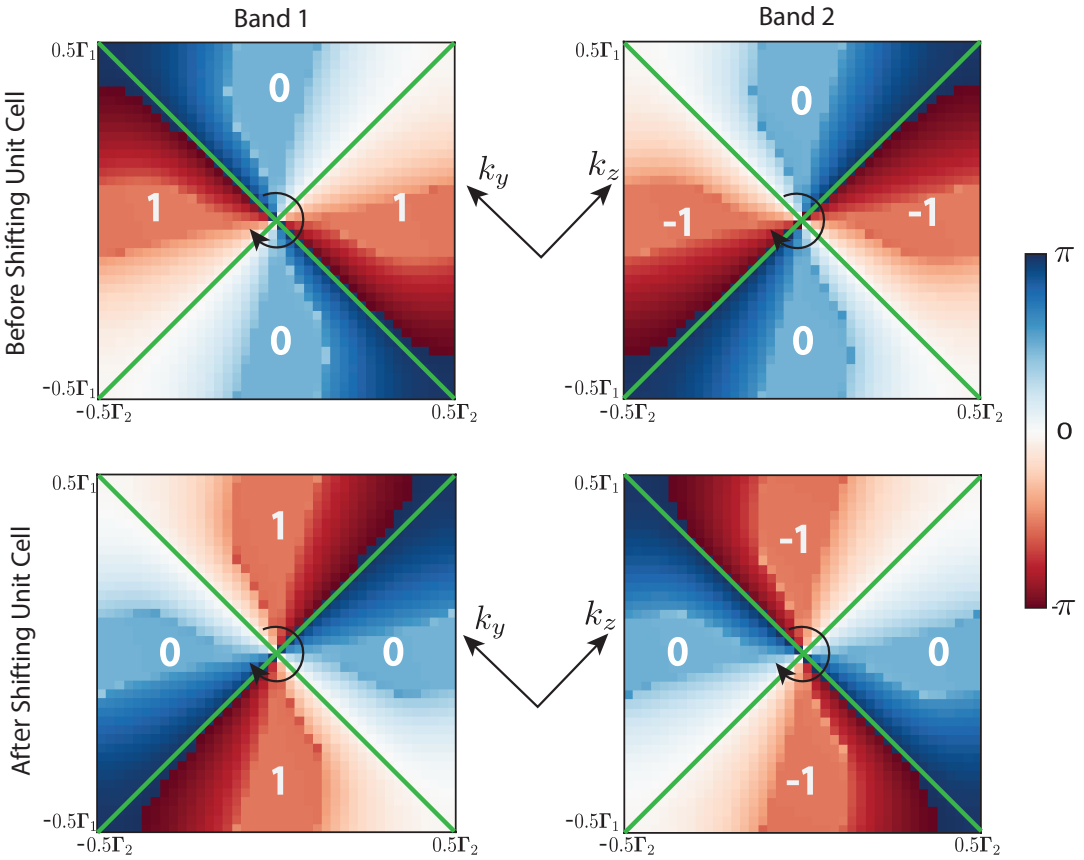

FIGURE 4.5: Wilson loop on $k_y k_z$ surface of woodpile PhC. The upper panels present for Wilson loop of before shifting unit cell. The lower panels present for Wilson loop of after shifting unit cell. The numbers on each part of Wilson loop results represent for winding number. "1" represents for the winding from $-\pi$ to π, "-1" represents for the winding from π to $-\pi$, 0 means there is no winding point.

Wilson loop in yz plane of woodpile PhC will be calculated depending on the closed surface formed by $\mathbf{\Gamma}_1$ and $\mathbf{\Gamma}_2$. The 1D integral will be taken along $\mathbf{\Gamma}_3$ direction. Beside the original primitive unit cell that is defined in Fig. 4.2(b), we will also

examine another primitive unit cell by shifting the origin of original primitive unit cell by $\frac{a_0}{4}, \frac{a_0}{4}, \frac{a_0}{2}$ in x, y and z direction, respectively. We call two types of unit cell are before shifting unit cell and after shifting unit cell.

The results for Wilson loop on $k_y k_z$ surface of two lowest bands are shown in Fig. 4.5. The upper panels present for before shifting unit cell. The lower panels present for after shifting unit cell. Band 1 is on the left side and band 2 is on the right side. Red and blue colors denotes the negative values ($-\pi$ to 0) and positive values (from 0 to π), respectively. Take the Γ point as origin, in the clock-wise direction, Wilson loop is varied from $-\pi$ to π. At some points, it jumps from $-\pi$ to π or from π to $-\pi$ which are called winding points. If the 2D BZ is devided into 4 parts as denoted by the green lines, we can count the number of winding in each part. The number 1, -1 represent for the winding from $-\pi$ to π, π to $-\pi$, respectively. 0 means that there is no winding in this region. In Fig. 4.5, we show the winding number for each band of woodpile PhC and for both before shifting and after shifting unit cell. Making the comparison between two types of unit cell, winding numbers are always opposite (zero and non-zero) in each corresponding part of 2D BZ. Therefore, if we create an interface between two types of unit cell which is parallel to yz surface, the topological interface states at the boundary can be expected.

4.4 Topological Interface States

In this section, we create the interface structure between before shifting and after shifting unit cell which is parallel to yz surface. Figure 4.6(a) is a schematic of a

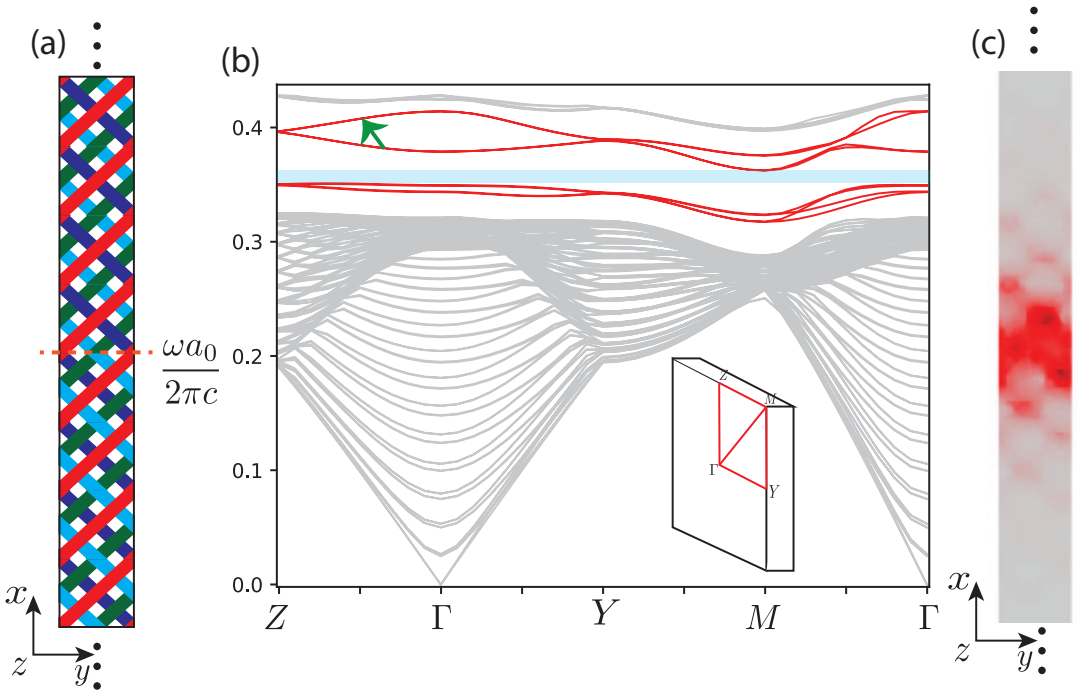

FIGURE 4.6: (a) A schematic of a supercell containing the interface parallel to yz surface. This supercell contains 8 before shifting unit cells and 8 after shifting unit cell. (b) Photonic band structure for the supercell in (a) with periodic boundary condition in three directions. The inset shows the first BZ for interface structure. Gray and red lines indicate bulks states and boundary states. (c) Field profile of the interface state denoted by green arrow.

supercell containing 8 before shifting unit cells and 8 after shifting unit cells. The interface between them is parallel to yz surface. By applying periodic boundary condition in three directions, we calculate and obtain photonic band structure for the supercell as shown in Fig. 4.6(b). Gray lines indicate bulk states, red lines present interface states where EM wave is localized at the boundary between two types of unit cell and decay exponentially. A field distribution at the interface state denoted by green arrow is shown in Fig. 4.6(c).

In the photonic band structure, we obtain 8 interface states in the complete band gap of woodpile PhC. They are doubly degenerate in almost k-points except in $\Gamma - M$ region. This is because of the broken IS in woodpile PhC. In between the interface states, we also see a complete band gap around the normalized frequency 0.36. The number of interface states can be explained by total winding number of each band as shown in Fig. 4.5. For before shifting unit cell, total winding number for band 1 is 2, for band 2 is -2. It is similar for after shifting unit cell. Winding number is proved to be equal to Chern number in ref [37]. Therefore, in both types of unit cell, Chern number for band 1 is 2 and for band 2 is -2. Because the number of interface states is equal to Chern number, each type of unit cell cause 4 interface states. That is why there are 8 interface states inside the complete band gap of woodpile PhC.

The topological interface states are confirmed to be formed in woodpile PhC due to the difference in winding numbers between two types of unit cell.

4.5 Topological Hinge States

In this section, we examine 1D hinge formed by woodpile PhC, which is parallel to z direction. Figure 4.7(a) is the schematic of investigated supercell. The supercell

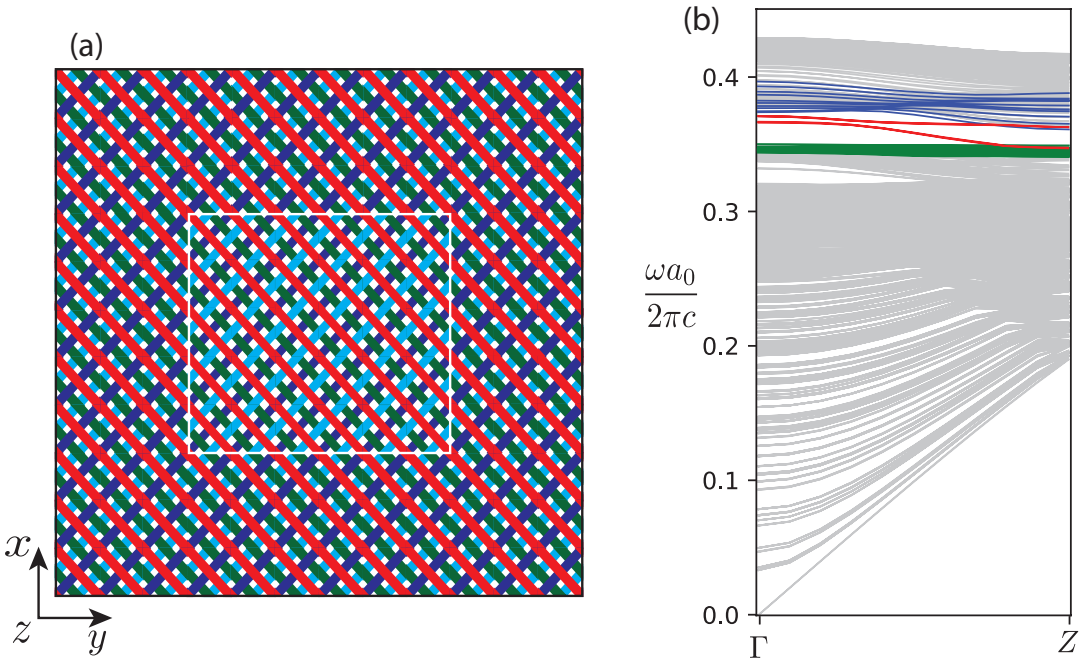

FIGURE 4.7: (a) A schematic of investigated supercell. The supercell size is $12a_0, 12a_0, a_0$ in x, y and z directions, respectively. In the center, 6×6 before shifting unit cells are embedded, which is surrounded by 3 layers of after shifting unit cell. (b) Photonic band structure of the supercell in (a). Gray lines indicate bulk states, green and blue lines are interface states, red lines denotes hinge states.

size is $12a_0, 12a_0, a_0$ in x, y and z directions, respectively. In the center, 6×6 before shifting unit cells are embedded, which is surrounded by 3 layers of after shifting unit cell. This supercell contains 4 hinges, in which 2 opposite hinges are equivalent. We calculate photonic band structure for the supercell with periodic boundary condition in 3 directions by FEM. Result is shown in Fig. 4.7(b). The gray lines are bulk states, interface states are labeled by green and blue lines. In the band gap, we obtain 2 hinge states (red lines), each state is doubly degenerate. These hinge states are in between the interface states and isolated from bulk states.

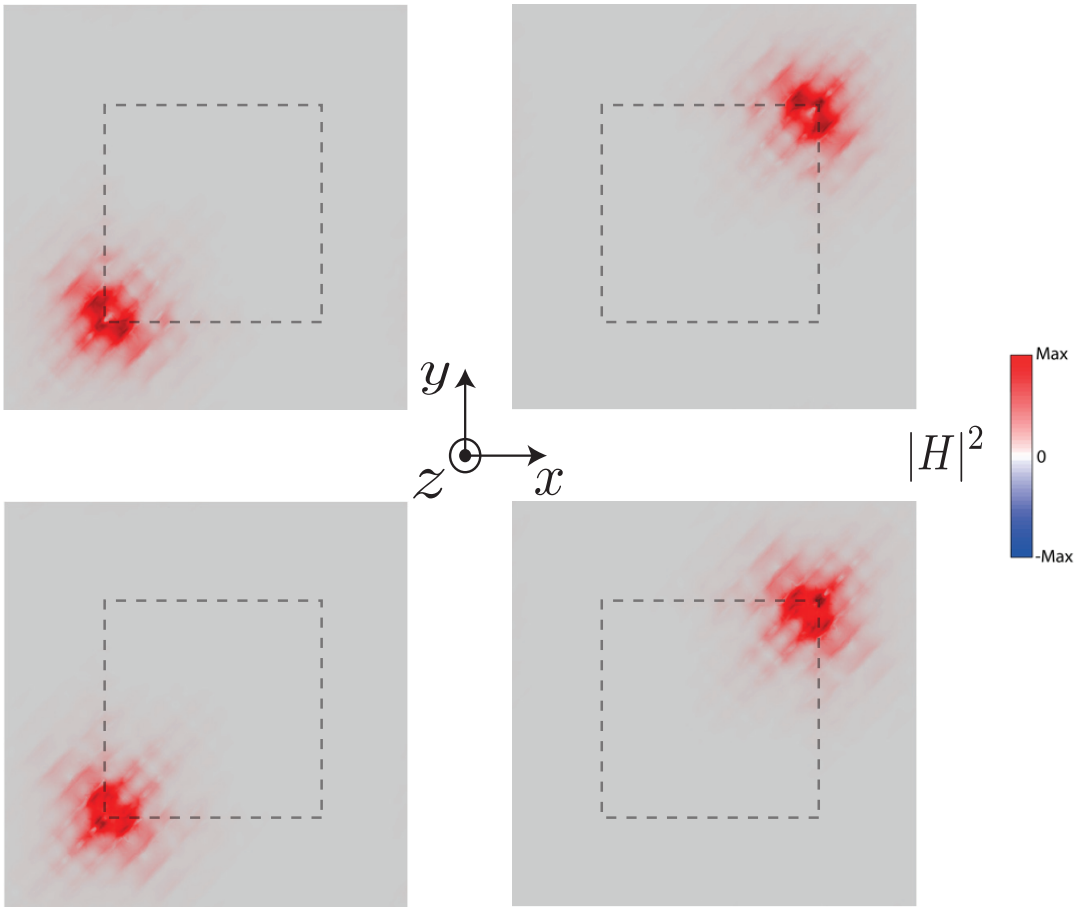

FIGURE 4.8: Magnetic field distribution of hinge states at $\mathbf{k} = (0, 0, 0.4)$. The dash lines indicate the boundary between two types of unit cell. Two upper panels are degenerate and two lower panel are degenerate.

Figure 4.8 is the magnetic field distribution of hinge states at $\mathbf{k} = (0, 0, 0.4)$. From these field profiles, we see that the double degeneracy of hinge states is because the two opposite hinges in the supercell are equivalent. However, hinge states only appear for upper right and lower left corners. There is no hinge states at other two corners. Because the hinges are formed by two interfaces parallel to yz and xz plane, this hinge states selection rule can be explained by the Wilson loop on $k_y k_z$ surface and $k_x k_z$ surface.

Similar to the calculation of Wilson loop on $k_y k_z$ surface in the previous section, we can also calculate Wilson loop on $k_x k_z$ surface and determine winding number for each part of 2D BZ by the same method for both before shifting and after shifting unit cells. The results are presented in Fig. 4.9. $\mathbf{\Gamma}_1', \mathbf{\Gamma}_2', \mathbf{\Gamma}_3'$ are three vectors in reciprocal space used to calculate Wilson loop on $k_x k_z$ surface. The values of Wilson loop have

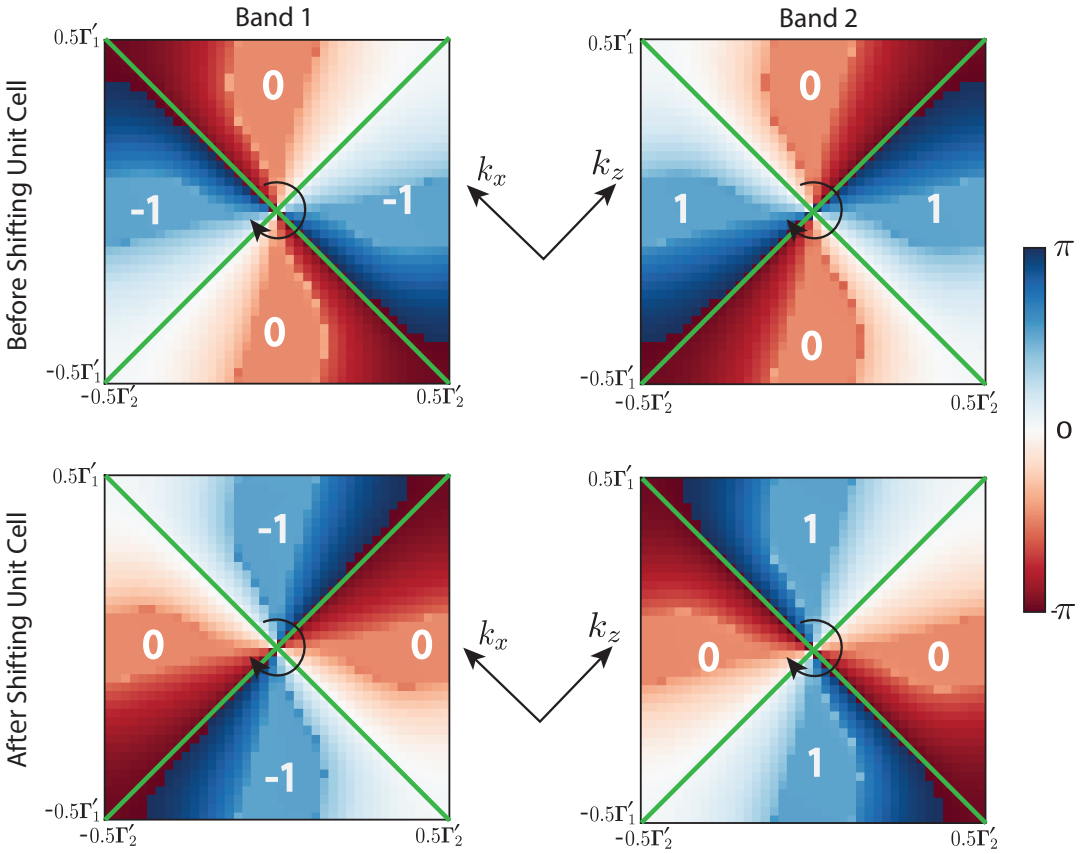

FIGURE 4.9: Wilson loop on k_xk_z surface of woodpile PhC. The upper panels present for Wilson loop of before shifting unit cell. The lower panels present for Wilson loop of after shifting unit cell. The numbers on each part of Wilson loop results represent for winding number. "1" represents for the winding from $-\pi$ to π, "-1" represents for the winding from π to $-\pi$, 0 means there is no winding point.

opposite sign at all k-points in 2D BZ compared with Wilson loop on k_yk_z surface. To explain for the hinge states selection rule, we create matrices which represent the condition of each interface between two types of unit cell. As shown in Fig. 4.7(a), 6×6 before shifting unit cells are arranged in the center of the supercell, surrounded by three layers of after shifting unit cells. The matrix represented for each interface is a 2×1 matrix $\begin{bmatrix} L \\ R \end{bmatrix}$. If we go along the propagation direction of injection light, L presents for winding number of the unit cell on the left side and R presents for winding number of the unit cell on the right side.

In Fig. 4.10(a), we assume that light propagating forward or backward x/ y directions will have positive and negative k_x/ k_y, respectively. Fig. 4.10(b) is the schematic of light propagating from interfaces to 4 hinges of the supercell with positive k vectors (blue text) and negative k vectors (red text). In band 1, the $\begin{bmatrix} L \\ R \end{bmatrix}$ matrices for each interface of the supercell when $k_z > 0$ and $k_z < 0$ are shown in Fig. 4.10(c) and (d), respectively. For both $k_z > 0$ and $k_z < 0$, we take the dot product of two $\begin{bmatrix} L \\ R \end{bmatrix}$ matrices, which form the hinges. For upper right and lower left hinges, the product are 0. For upper left and lower right hinges, the products are non-zero. Therefore, the condition for the emergence of topological hinge states in this woodpile PhC is

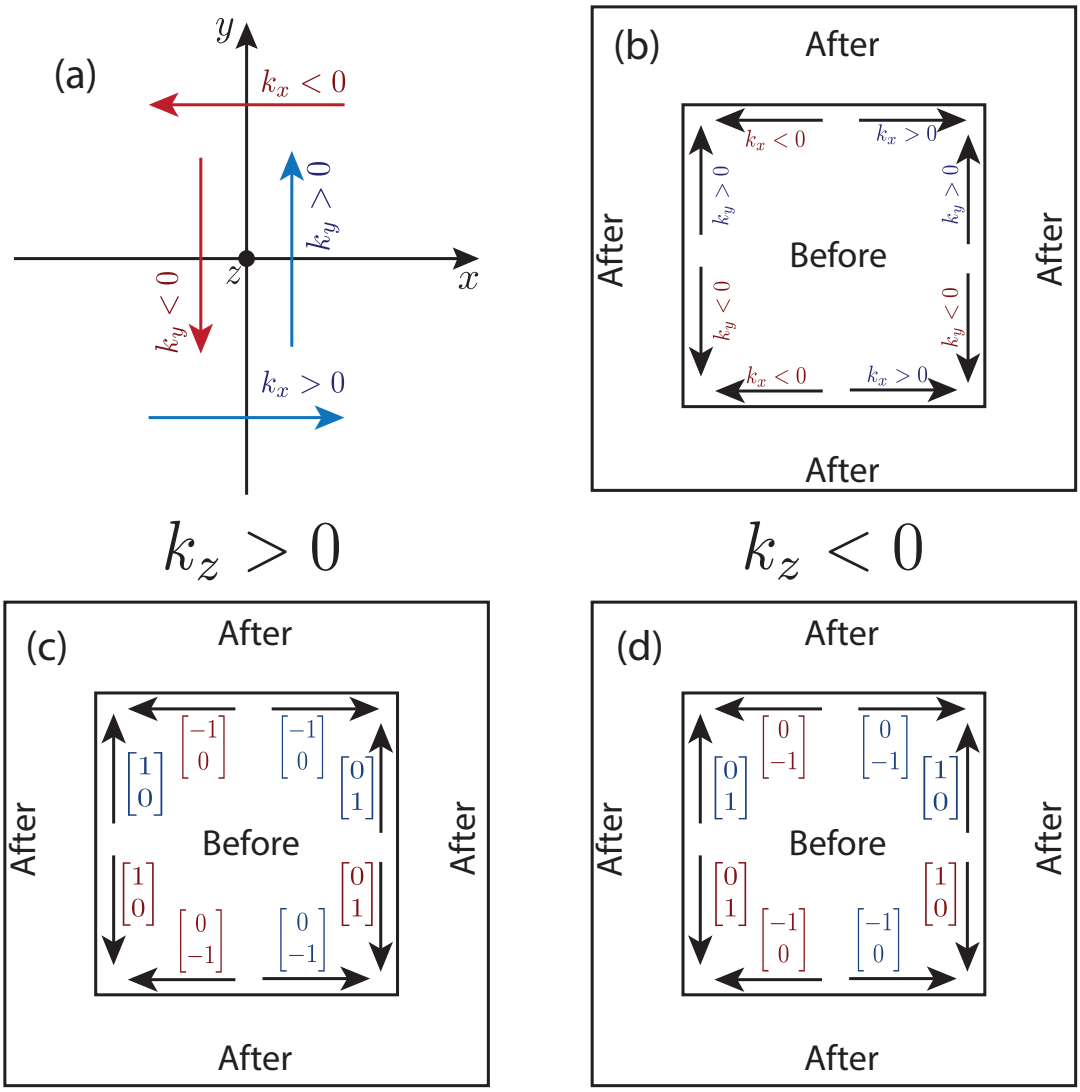

FIGURE 4.10: (a) Coordination of real space. Assuming that light propagating forward and backward x/y directions will have positive and negative $k_x/\ k_y$, respectively. (b) Schematic of light propagating to the hinges from two surfaces. (c) $\begin{bmatrix}L\\R\end{bmatrix}$ matrix of each interface when $k_z > 0$. (d) $\begin{bmatrix}L\\R\end{bmatrix}$ matrix of each interface when $k_z < 0$. In both (c) and (d), the matrices are for band 1.

that the product of $\begin{bmatrix}L\\R\end{bmatrix}$ matrices of two interface forming the hinges is equal to 0. To make this statement more coherent, we also present another case, where light is injected to the hinge from one interface, then reflected to other hinge as shown in Fig. 4.11.

Similar to the previous case, we also assume that the wave vector is positive or negative when the propagation direction of EM wave is forward or backward each axis as shown in Fig. 4.11(a). The schematic of propagation direction of EM wave at each hinge are shown in Fig. 4.11(b). We also point out the $\begin{bmatrix}L\\R\end{bmatrix}$ matrix of band 1 for each interface where $k_z > 0$ (Fig. 4.11(c)) and $k_z < 0$ (Fig. 4.11(d)). The product

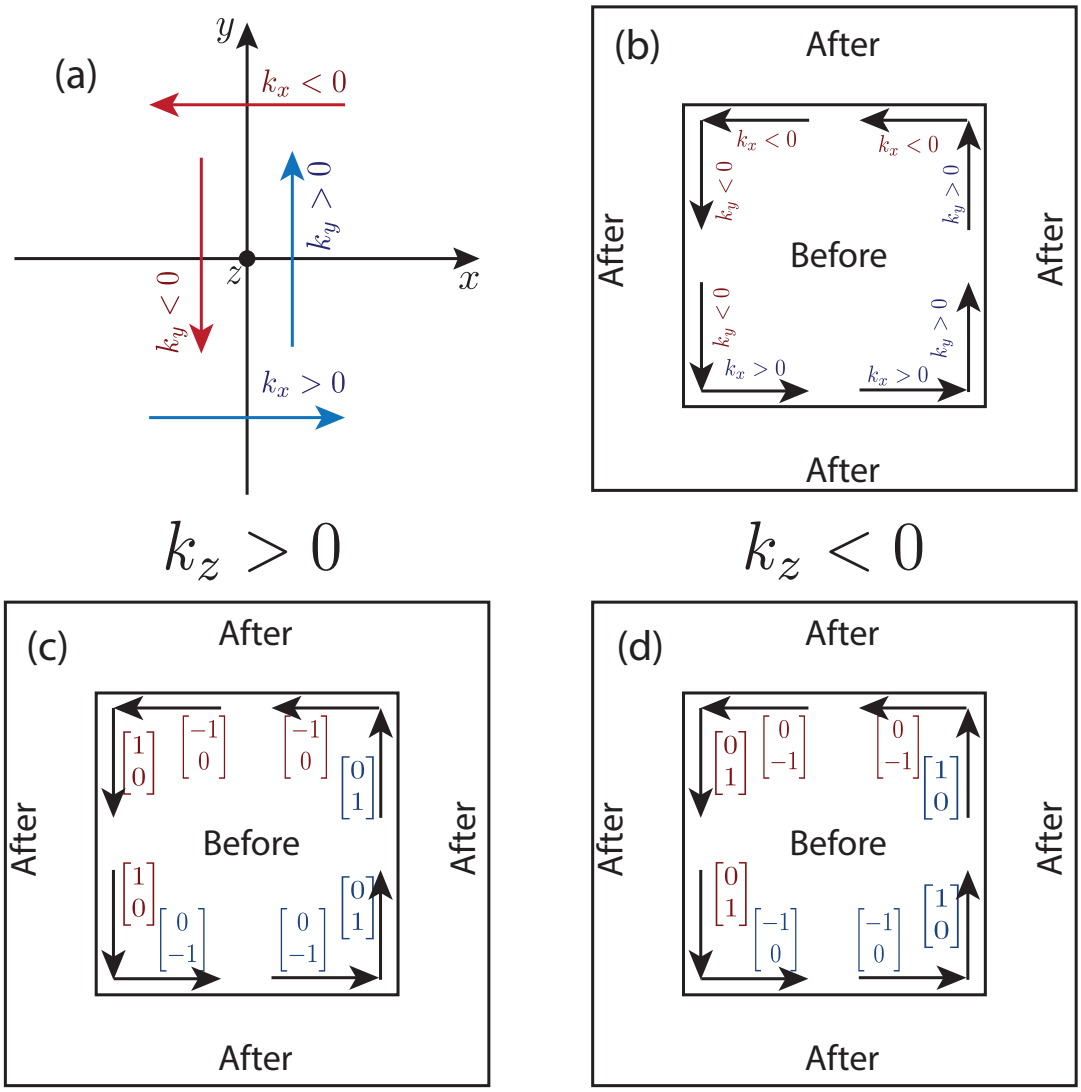

FIGURE 4.11: (a) Coordination of real space. Assuming that light propagating forward and backward x/y directions will have positive and negative $k_x/\ k_y$, respectively. (b) Schematic of light propagating to the hinges from one surface then reflected to other surface. (c) $\begin{bmatrix} L \\ R \end{bmatrix}$ matrix of each interface when $k_z > 0$. (d) $\begin{bmatrix} L \\ R \end{bmatrix}$ matrix of each interface when $k_z < 0$. In both (c) and (d), the matrices are for band 1.

of two $\begin{bmatrix} L \\ R \end{bmatrix}$ matrices which form the hinges are also 0 for upper right, lower left hinges and non-zero for upper left, lower right hinges. Therefore, the condition for the emergence of hinge states is similar to the previous case.

For both two case in Fig. 4.10 and Fig. 4.11, we obtain the same selection rule for the hinge states. When the product of $\begin{bmatrix} L \\ R \end{bmatrix}$ matrices is 0, hinge states appear. When it is non-zero, hinge states are absence. Considering the dot products, if it is 0, for example

$$\begin{bmatrix} 0 \\ -1 \end{bmatrix} \cdot \begin{bmatrix} 1 \\ 0 \end{bmatrix} = 0 * 1 + (-1) * 0 = 0 \tag{4.7}$$

it indicates the boundary between a topological interface (winding number is $1/-1$) and a trivial interface (winding number is 0). On the other hand, if the products is non-zero, for example,

$$\begin{bmatrix} 0 \\ -1 \end{bmatrix} \cdot \begin{bmatrix} 0 \\ 1 \end{bmatrix} = 0 * 0 + (-1) * 1 = -1 \tag{4.8}$$

it denotes the boundary between two topological interface (winding number 1 and -1) or two trivial interface (winding number 0).

We have presented the conditions for the emergence of hinge states in band 1. In band 2, doing similar manners, we also got the same conditions as in band 1.

4.6 Summary and Discussion

In this Chapter, we have numerically studied EM wave states in 3D woodpile PhC by using FEM and FDM. The systems contains dielectric blocks and air, which follows the diamond cubic lattice. TRS is preserved in this photonic structure. However, IS is broken. We obtain a large complete band gap in this woodpile PhC, which is around the normalized frequency 0.38. Below the complete band gap, there are 8 connected photonic bands for conventional unit cell and there are 2 connected photonic bands for primitive unit cell. This is because the volume of conventional unit cell is 4 times bigger than the volume of primitive unit cell.

We used the primitive unit cell to numerically calculate Wilson loop on different 2D surfaces of woodpile PhC. Compared with simple cubic PhC, woodpile PhC's primitive unit cell is not a cubic or rectangle. Three primitive vectors are not orthogonal to each other. Therefore, the original first BZ can not be used to determined Wilson loop. A new BZ is redefined to calculate Wilson loop for each band of woodpile PhC. Since IS is broken in this structure, Wilson loop is varied from $-\pi$ to π, forming the winding number. For both types of unit cell, Wilson loop on $k_y k_z$ surface of each band is different in each part of the 2D BZ. This causes the topological transition at the interface between two types of unit cell.

Topological interface states is observed in the complete band gap of woodpile PhC. The number of interface states is explained by the winding number of each photonic band. We also obtain a complete band gap in between the interface states of bulk-interface correspondence. Topological hinge states in z direction is observed in the gap between interface states. These hinge is formed by an interface paralleled to yz surface and an interface paralleled to xz surface. Wilson loop on xz surface is also involved in the formation of topological hinge states.

The selection rule for topological hinge states is pointed out by a mathematical representation of each interface. Hinge states emerge when the product of 2 matrices represented for two interfaces which form the hinge is 0. If the product of these two matrices is non-zero, topological hinge states are absent. These topological hinge states are isolated from other states and inside the band gap between interface states.

Our numerical results of wave propagation in 3D woodpile PhC are essential and put a step toward the experimental realization of topological waveguide in 3D PhCs. They are applicable in the communication technology.

Chapter 5

Conclusions and Outlooks

Crystals are an important class of natural or artificial materials that can be utilized to manipulate variety of physical waves by their interference in periodic structures. In crystals, waves can propagate through, be reflected, confined or guided in specific ways. The behaviours of waves, therefore, are very complicated. There are still many queries about the topic of wave in crystals that remain unanswered. In this doctoral thesis, we numerically and theoretically analyze the propagation and confinement of EM waves in PhC structure, which allow us to better understand about waves behaviour in crystals. Although our results are illustrated on and applied for EM wave in specific 2D and 3D PhCs, many of them are applicable for other types of wave in general crystals. Here I make a summary, present the conclusions for this thesis and outlooks for future studies.

In chapter 1, we introduce the topic of EM wave propagation in PhC and the mathematical demonstration of EM waves in PhC. We also make a brief review of photonic band structure and photonic band gaps. We conclude this chapter by explaining the numerical methods which are used to determine propagation of EM wave in PhC.

In chapter 2, we introduce about the mathematical concept of "topology" and the application of "topology" in physics. The topological invariants are mentioned in this chapter, which are the essential physical quantities to examine topological properties of systems. In the end of this chapter, we examine a 2D topological PhC following BPN network structure. The topological edge states and topological corner states are found in this BPN PhC due to the non-trivial Zak phase. To our knowledge, the topological edge states surpass any other candidates in the application to waveguide devices by their low-loss energy property. The topological confinement of EM wave at corners is also a strong candidate among many wave confinements methods. By examining different corner structures in BPN PhC, we point out the condition for the emergence of topological corner states based on Zak phase and the frequency range of topological edge states. Compared the results with graphene-like PhCs, our PhC structure can exhibit topological properties without breaking the IS.

In chapter 3, we extend our studies to a 3D simple cubic PhC, which is in the presence of TRS and IS. A numerical methods for calculating Zak phase in 3D PhC is introduced in this chapter. The numerical results are consistent with the polarization of EM wave in the crystal. Due to non-trivial Zak phase, we examined and obtained 2D topological interface states in simple cubic PhC. The second order topological states as hinge states are also numerically observed in this structure. The numerical method that we develop for calculating Zak phase is a priori not restricted for only photonic systems, but it can also be applied for other systems. Our calculation will also help us deeply under stand the topological invariants in 3D systems. Because this simple cubic structure is highly symmetric, the third order topological states as the 0D corner states are expected to be observed. However, since the frequency

ranges for bulk and interface states almost overlap the complete band gap, hinge states are found to be mixed with other states. The 0D corner states are also be mixed with other states, which are very difficult to be detected by numerical calculation.

Chapter 4 is spent for the studies of topological states in 3D woodpile PhC, where TRS is preserved but IS is broken. Unlike simple cubic lattice, Zak phase in woodpile PhC is not quantized to π and 0, it is varied from $-\pi$ to π and exhibit winding properties. Therefore, the topological invariants in this structure is not Zak phase, it is winding number, which can be determined via Wilson loop. When winding number is 0 or non-zero, the systems is topologically trivial or non-trivial, respectively. The topological interface states are numerically observed in woodpile PhC due to the finite difference in winding number. In the end of this chapter, we present the numerical observation of second order topological states as hinge states in woodpile PhC. Because the IS is absence, there is a selection rule for the emergence of topological hinge states in this structure. We pointed out this selection rule by a mathematical description. The 0D corner states in this woodpile PhC are not found in this woodpile structure due to the non-equivalent of hinges in 3 directions.

We have several propositions for extension and continuation of our studies. It would be very interesting if we can apply our Zak phase calculation method to a continuum media instead of periodic structure. From this point of view, we can examine the topological wave confinement in the continuum media.

For the BPN PhC, there are several ways to modify the original BPN structure. We have examined one of them in this thesis and obtained topological edge states in several ribbon structures. It is possible to try other modification ways. We may obtained topological waveguide in other ribbon structures. This will be very useful for guiding light in several directions.

It will be interesting if we can observe 0D corner states in 3D PhCs. An obvious extension here is to optimize the 3D simple cubic structure to look for the 0D corner states. Beyond that, we will also investigate other PhC structure in the same manner as we did for simple cubic and woodpile PhCs.

Beside the studies of topological wave functions we did in this thesis, the topological properties of complex eigenvalues can also be studied in non-hermitian systems. The complex eigenvalues indicate gain and loss of the systems. By studying the topological properties of complex eigenvalues, we can pave the way to the optical devices where the gain and loss are controllable.

Appendix A

Zak phase of 1D Photonic Crystal

A.1 One-dimensional Photonic Crystal

A.1.1 Eigenvalue problem in 1D photonic crystal

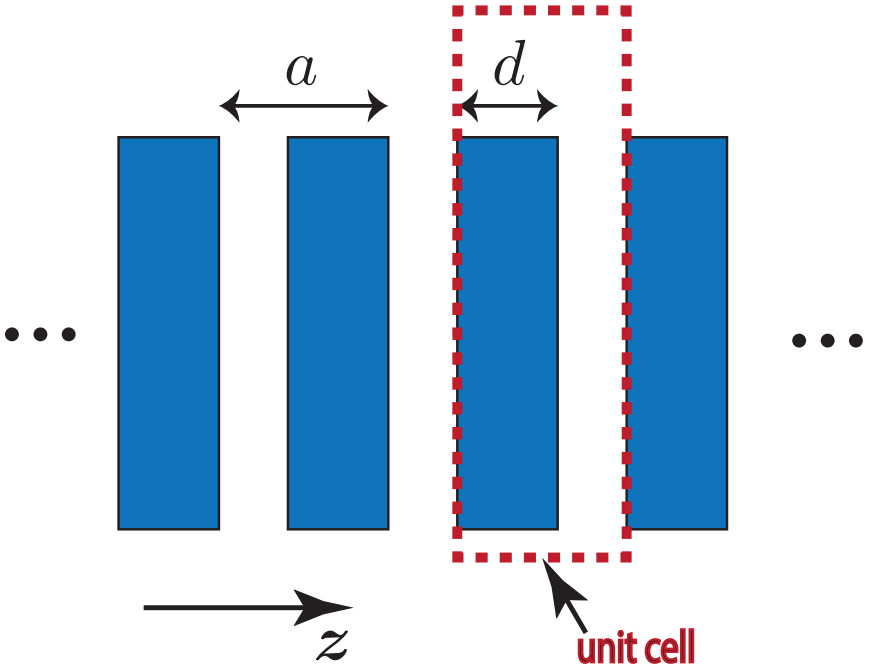

FIGURE A.1: One-dimensional photonic crystal. Dielectric slabs are arranged periodically along z direction. Width of each slab is d, lattice constant is a. The red dash line denote a unit cell.

The simplest example of PhCs is an 1D dielectric slabs penetrating in air background, where electromagnetic waves are assumed to propagate along z-axis. We consider that electric field and magnetic field are polarized along x and y direction, respectively. There are two basic polarizations, in this case, transverse electric (TE) modes and transverse magnetic (TM) modes become essentially identical.

Figure 1.4 is the schematic of one-dimensional photonic crystal. Dielectric slabs with $\varepsilon > 1$ and air slabs with $\varepsilon = 1$ are arranged periodically in z direction. In x and y direction, dielectric constant is homogeneous. Lattice constant is a, air slab width is d, dielectric slab width is $a - d$. Electric field propagates along z direction.

From Eq. (1.11), and the use of the relationship

$$\nabla \times \nabla \times \boldsymbol{E}(\boldsymbol{r}) = \nabla (\nabla \cdot \boldsymbol{E}(\boldsymbol{r})) - \nabla^2 \boldsymbol{E}(\boldsymbol{r}), \tag{A.1}$$

we obtain wave equation for transverse magnetic field as follow

$$-\frac{1}{\varepsilon(\boldsymbol{r})}\boldsymbol{\nabla^2}\boldsymbol{E}(\boldsymbol{r})=\frac{\omega^2}{c^2}\boldsymbol{E}(\boldsymbol{r}). \tag{A.2}$$

Especially, for 1D PhCs

$$-\frac{1}{\varepsilon(z)}\frac{\partial^2}{\partial z^2}E(z)=\frac{\omega^2}{c^2}E(z), \tag{A.3}$$

Similarly, the eigenvalue equation for magnetic field of 1D PhC can be derive from Eq. (1.12) and be written as

$$\left(\frac{\partial}{\partial z}\frac{1}{\varepsilon(z)}\right)\left(-\frac{\partial}{\partial z}H(z)\right)-\frac{1}{\varepsilon(z)}\frac{\partial^2}{\partial z^2}H(z)=\frac{\omega^2}{c^2}H(z) \tag{A.4}$$

with z is propagating direction.

Now, we apply Fourier series expansion and Bloch theorem for wave function and dielectric constant.

$$E_{k_z}(z)=\sum_{n=-\infty}^{\infty}\kappa_n^e e^{i\frac{2\pi n}{a}z}e^{ik_z z}, \tag{A.5}$$

$$\frac{1}{\varepsilon(z)}=\sum_{m=-\infty}^{\infty}\kappa_m^\varepsilon e^{i\frac{2\pi m}{a}z}. \tag{A.6}$$

After Fourier expansion, we substitute the above two equations back to Eq. (A.3)

$$\sum_{n=-\infty}^{\infty}\sum_{m=-\infty}^{\infty}\left(k_z+\frac{2\pi n}{a}\right)^2\kappa_n^e\kappa_m^\varepsilon e^{i\frac{2\pi m}{a}z}e^{i\frac{2\pi n}{a}z}e^{ik_z z}=\frac{\omega^2}{c^2}\sum_{n=-\infty}^{\infty}\kappa_n^e e^{i\frac{2\pi n}{a}z}e^{ik_z z}, \tag{A.7}$$

To simplify, both sides of above equation are divided by $e^{ik_z z}$ then multiplied with the orthogonal function $e^{-i\frac{2\pi p}{a}z}$ and integrated over the whole unit cell $\int_{-a/2}^{a/2}dz$.

$$\sum_{n=-\infty}^{\infty}\sum_{m=-\infty}^{\infty}\left(k_z+\frac{2\pi n}{a}\right)^2\kappa_n^e\kappa_m^\varepsilon e^{i\frac{2\pi m}{a}z}e^{i\frac{2\pi n}{a}z}e^{-i\frac{2\pi p}{a}z}=\frac{\omega^2}{c^2}\sum_{n=-\infty}^{\infty}\kappa_n^e e^{i\frac{2\pi n}{a}z}e^{-i\frac{2\pi p}{a}z} \tag{A.8}$$

$$\sum_{n=-\infty}^{\infty}\sum_{m=-\infty}^{\infty}\left(k_z+\frac{2\pi n}{a}\right)^2\kappa_n^e\kappa_m^\varepsilon e^{-i\frac{2\pi(p-n-m)}{a}z}=\frac{\omega^2}{c^2}\sum_{n=-\infty}^{\infty}\kappa_n^e e^{-i\frac{2\pi(p-n)}{a}z} \tag{A.9}$$

$$\sum_{n=-\infty}^{\infty}\sum_{m=-\infty}^{\infty}\left(k_z+\frac{2\pi n}{a}\right)^2\kappa_n^e\kappa_m^\varepsilon\delta_{p-n-m=0}=\frac{\omega^2}{c^2}\sum_{n=-\infty}^{\infty}\kappa_n^e\delta_{p-n=0} \tag{A.10}$$

$$\sum_{n=-\infty}^{\infty}\left(k_z+\frac{2\pi n}{a}\right)^2\kappa_{p-n}^\varepsilon\kappa_n^e=\frac{\omega^2}{c^2}\kappa_p^e, \tag{A.11}$$

We define a matrix M by

$$M_{pn} = \sum_{n=-\infty}^{\infty} \left(k_z + \frac{2\pi n}{a}\right)^2 \kappa^{\varepsilon}_{p-n}. \tag{A.12}$$

This matrix is Hermitian:

$$M_{pn} = M^*_{pn}. \tag{A.13}$$

The eigenvalue equation takes the final form of Eq. (A.11). Both indices p, n can be positive or negative integers. To solve this eigenvalue equation, we need to know Fourier expansion coefficients of dielectric constant κ^{ε}_m.

The dielectric function for 1D PhC is

$$\varepsilon(z) = \begin{cases} 1 & |z| < d/2, \\ \varepsilon_1 & d/2 < |z| < a/2. \end{cases} \tag{A.14}$$

To calculate Fourier expansion coefficients of dielectric constant, we divide the unit cell into three parts. From $-a/2$ to $-d/2$, $\varepsilon = \varepsilon_1 > 1$; from $-d/2$ to $d/2$, $\varepsilon = \varepsilon_0 = 1$; from $d/2$ to $a/2$, $\varepsilon = \varepsilon_1 > 1$. Depending on where we define $z = 0$, the result is a little bit different, but the difference has no effect on energy dispersion. By using inverse Fourier transform, we obtained coefficients κ^{ε}_m as following

$$\begin{aligned}
\kappa^{\varepsilon}_m &= \frac{1}{a}\int_{-a/2}^{a/2} \frac{1}{\varepsilon(z)} e^{-i\frac{2\pi m}{a}z} dz \\
&= \frac{1}{a}\int_{-a/2}^{-d/2} \frac{1}{\varepsilon(z)} e^{-i\frac{2\pi m}{a}z} dz + \frac{1}{a}\int_{-d/2}^{d/2} \frac{1}{\varepsilon(z)} e^{-i\frac{2\pi m}{a}z} dz + \frac{1}{a}\int_{d/2}^{a/2} \frac{1}{\varepsilon(z)} e^{-i\frac{2\pi m}{a}z} dz \\
&= \frac{1}{a}\frac{-a}{i2\pi m}\left(\frac{1}{\varepsilon_1} e^{-i\frac{2\pi m}{a}z}\Big|_{-a/2}^{-d/2} + e^{-i\frac{2\pi m}{a}z}\Big|_{-d/2}^{d/2} + \frac{1}{\varepsilon_1} e^{-i\frac{2\pi m}{a}z}\Big|_{d/2}^{a/2}\right) \\
&= \frac{1}{a}\frac{-a}{i2\pi m}\left(\frac{1}{\varepsilon_1} e^{i\frac{\pi m d}{a}} - \frac{1}{\varepsilon_1} e^{i\pi m} + e^{-i\frac{\pi m d}{a}} - e^{i\frac{\pi m d}{a}} + \frac{1}{\varepsilon_1} e^{-i\pi m} - \frac{1}{\varepsilon_1} e^{-i\frac{\pi m d}{a}}\right) \\
&= \frac{1}{a}\frac{a}{i2\pi m}\left[\frac{1}{\varepsilon_1}\left(e^{-i\frac{\pi m d}{a}} - e^{i\frac{\pi m d}{a}}\right) - \frac{1}{\varepsilon_1}\left(e^{-i\pi m} - e^{i\pi m}\right) + \left(e^{i\frac{\pi m d}{a}} - e^{-i\frac{\pi m d}{a}}\right)\right] \\
&= \frac{1}{a}\frac{a}{i2\pi m}\left[-2i\frac{1}{\varepsilon_1}\sin\frac{\pi m d}{a} + 2i\frac{1}{\varepsilon_1}\sin(\pi m) + 2i\sin\frac{\pi m d}{a}\right] \\
&= \frac{1}{\pi m}\left[-\frac{1}{\varepsilon_1}\sin\frac{\pi m d}{a} + \frac{1}{\varepsilon_1}\sin(\pi m) + \sin\frac{\pi m d}{a}\right] \\
&= \frac{1}{\varepsilon_1} sinc(\pi m) + \left(1 - \frac{1}{\varepsilon_1}\right)\frac{d}{a} sinc\frac{\pi m d}{a} \\
&= \frac{1}{\varepsilon_1}\delta_{m,0} + \left(1 - \frac{1}{\varepsilon_1}\right)\frac{d}{a} sinc\frac{\pi m d}{a},
\end{aligned}$$

where $sinc(x) = \frac{\sin(x)}{x}$.

Now we have enough information to diagonalize matrix M numerically. After diagonalization, the eigenvalue $\frac{\omega^2}{c^2}$ and the eigenvectors κ^e_n can be known. The squared root of eigenvalues give the information about energy dispersion, eigenvectors give information about field distribution in the PhC. The calculation here was

done by using plane wave expansion method and the computational language used is Python.

A.1.2 Numerical results

The result of solving eigenvalue equation (A.11) is shown as photonic band structure as in Fig. A.2(b) with $d = 0.2a$, $\varepsilon_1 = 12.25$. x-axis is wave vector k, y-axis is frequency $\frac{\omega a}{2\pi c}$. This frequency is called normalized frequency because it is only depend on the period of structure. As a results, it remains unchanged if we change the scale of PhC.

If a 1D homogeneous structure is considered, the result for eigenfrequencies is ck as shown in Fig. A.2(a). Eigenfrequencies fill from 0 and there is no band gap for this structure. However, it can be easily see that eigenfrequencies of 1D PhC also starts from 0 at $k = 0$, the bands and band gaps appear alternately. Wave can not propagate into the PhC in the frequency range of band gap.

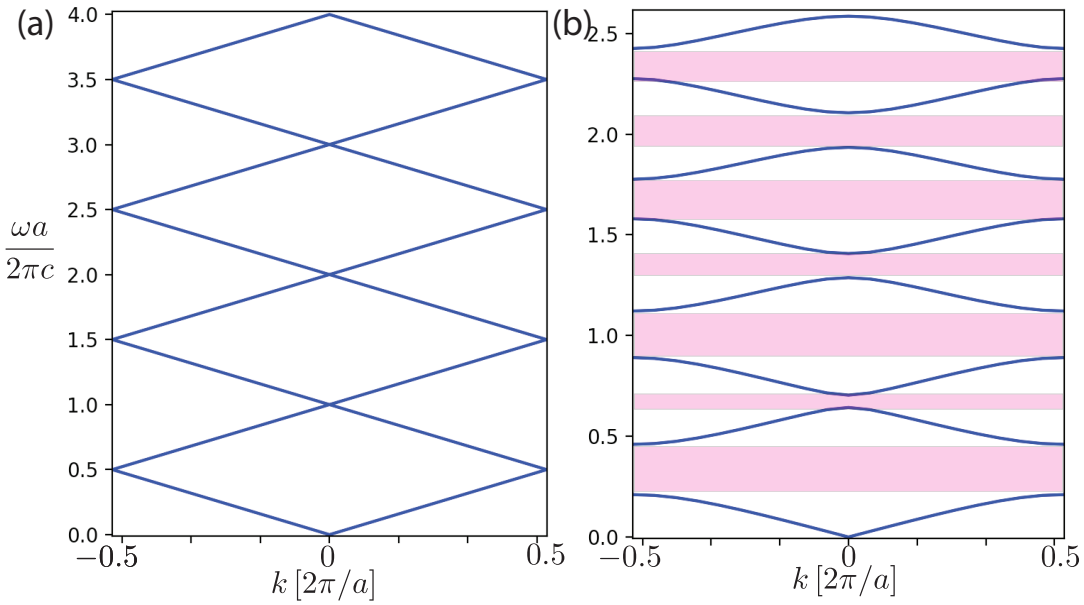

FIGURE A.2: Photonic band structure for wave propagate in uniform material $\varepsilon = 1$ (a) and in a 1D PhC with $d/a = 0.2$ (b) in the first BZ. The shaded regions are band gap.

A.2 Zak Phase of 1D Photonic Crystal

In 1D PhC, Zak phase is determined for each individual band by integrating Berry connection over the first BZ. In this section, we show the numerical calculation results for Zak phase of 1D PhC, which is mentioned in previous section.

In Fig. A.3, Zak phase for eight lowest bands of 1D PhC are labeled green. They are quantized to π and 0 because IS is preserved in this PhC structure [26]. π values indicate topologically non-trivial bands. 0 values mean that photonic bands are topologically trivial.

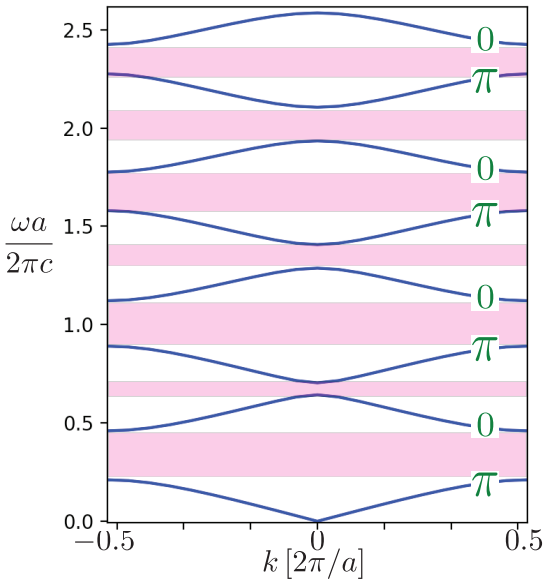

FIGURE A.3: Zak phase of 1D PhC, where $d/a = 0.2$, $\varepsilon = 12.25$, are shown by green text in each band.

Appendix B

Topological States of Honeycomb Photonic Crystal

In this appendix we will consider a photonic structure following honeycomb lattice where IS is broken. We examine two inversed structures where their topological invariants are opposite. Then we numerically examine topological interface states which emerge at the boundary between two inversed structures.

B.1 Honeycomb Photonic Crystal and Berry Curvature

Figure B.1 shows a example of 2D honeycomb PhC with broken inversion symmetry, where two dielectric rods in unit cells (call rod A and rod B) have different radii. We assume that the rods are made of YIG, i.e., the dielectric constant is $\varepsilon = 15$. The lattice constant is $a_0 = 500nm$ and radius size is $r_A = 0.1a_0$ and $r_B = 0.0825a_0$, respectively.

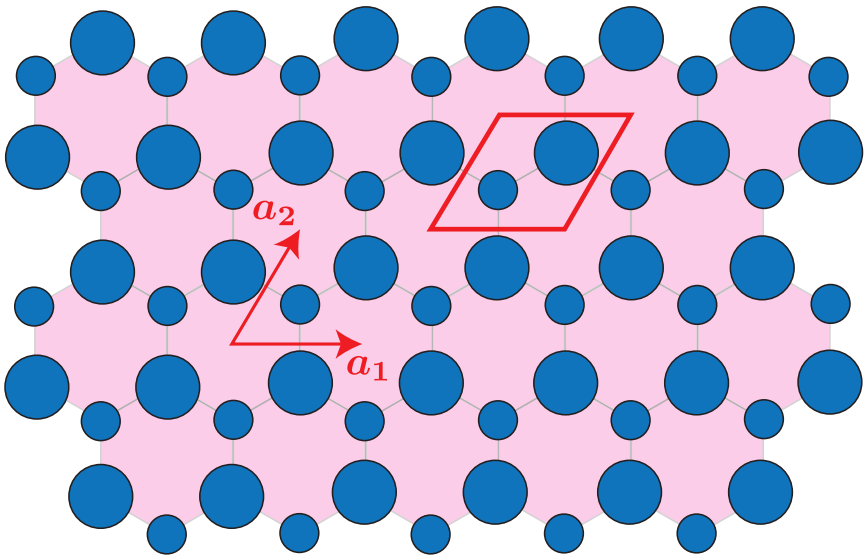

FIGURE B.1: 2D honeycomb PhC with broken inversion symmetry, where two rods in unit cells have the different radii.

The eigenvalue equation for TM modes is calculated by using COMSOL Multiphysics and the results of photonic band structure is shown in Fig. B.2(b). Compared to photonic band structure of the normal honeycomb PhC in Fig. B.2(a) where IS is preserved, it is found that the degeneracies of Dirac cones at K and K' points are lifted owing to the broken inversion symmetry. Thus, a photonic band gap between the first and the second band is opened around normalized frequency 0.4 together

with some gaps at higher frequency of 0.58, 0.80 and 0.96. In this part, we will focus on the properties of lifting the Dirac cones at two valleys K and K'.

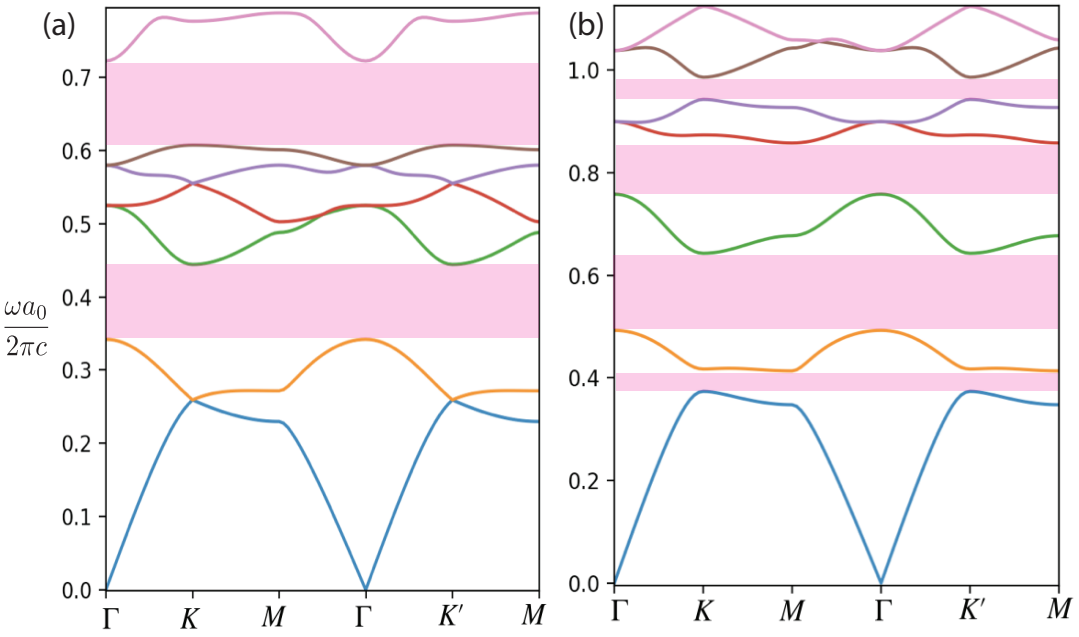

FIGURE B.2: (a) Photonic band structure for honeycomb PhC, where IS is preserved. (b)Photonic band structure for honeycomb PhC in broken IS with parameters $r_A = 0.1a_0$, $r_B = 0.0825a_0$, $\varepsilon = 15$.

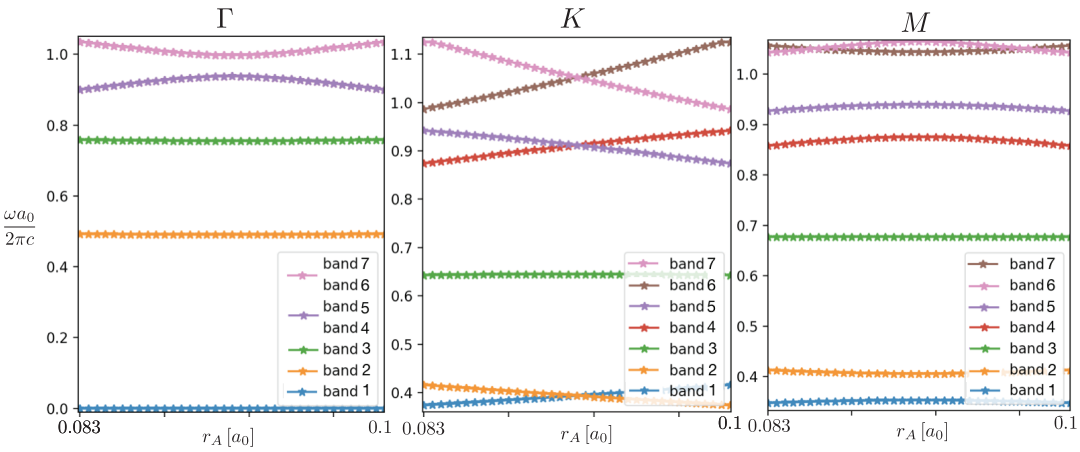

FIGURE B.3: The radius size dependence of eigenfrequency for the 7 lowest EM modes at high symmetric points.

To examine the first band gap, we will determine how the band structure change when the rods size r_A and r_B are tuned. Fig. B.3 shows the radius size dependence of eigenfrequency for the 7 lowest EM modes at high symmetric points Γ, K, M, where the summation of r_A and r_B is kept constant $r_A + r_B = 0.183$. When $r_A = r_B$, band inversion appears at K point. We can also confirm from Fig. B.3 that if r_A and r_B value are interchanged, photonic band structure remains unchanged but some states at K point are interchanged due to the band inversion. Because of this property, we consider two inverted PhC structures, which have the unit cell as shown in Fig. B.4(a). PhC1 has two rods in each unit cell with radii size r_A and r_B placed in

the air medium. PhC2 can be obtained by interchanging the position of two dielectric rods in PhC1. These two PhC structures share the same photonic band structure given in Fig. B.2(b).

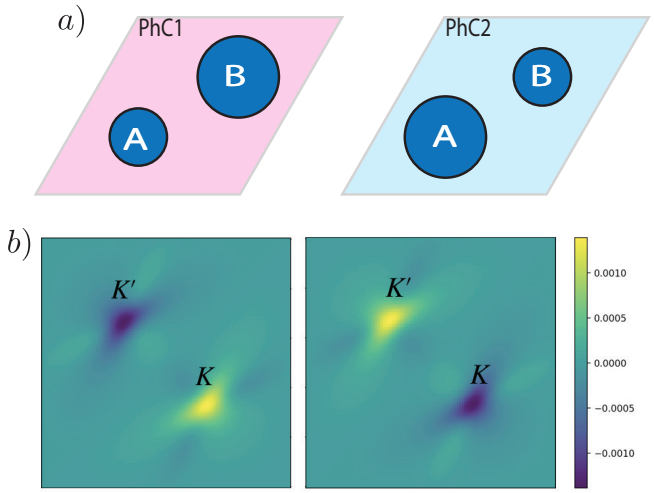

FIGURE B.4: Two inverted photonic structure which share the same photonic band structure in Fig. B.2(b).

Fig. B.4(b) gives the Berry curvature distribution in the first BZ of PhC1 and PhC2. Due to the broken inversion symmetry, the Berry curvature around two valleys K and K' have different distribution. For PhC1, Berry curvature distribution around K point have positive value, that around K' point have the same magnitude but opposite sign. PhC2 has reversed Berry curvature distribution compared to PhC1.

B.2 Topological Interface States

Total Chern number of the first band of the two PhCs is 0 because of preserved time reversal symmetry. We can also calculate valley-Chern number around K and K' point by integrating Berry curvature over one half of BZ around each point. The valley-Chern number C of PhC1 for two valleys are $C^1_K = 1/2$, $C^1_{K'} = -1/2$, while for PhC2, $C^2_K = -1/2$, $C^2_{K'} = 1/2$. Because of this property, it will promise a phase transition at the interface between PhC1 and PhC2 when we make a connection between them.

The valley-Chern number difference at the interface is quantized as

$$\Delta C_{K_{1\to2}} = 1/2 - (-1/2) = 1, \tag{B.1}$$
$$\Delta C_{K'_{1\to2}} = -1/2 - 1/2 = -1, \tag{B.2}$$
$$\Delta C_{K_{2\to1}} = -1/2 - 1/2 = -1, \tag{B.3}$$
$$\Delta C_{K'_{2\to1}} = 1/2 - (-1/2) = 1. \tag{B.4}$$

where $\Delta C_{K_{1\to2}}$ or $\Delta C_{K_{2\to1}}$ indicate the interface formed by PhC1 stands below or above PhC2. As a result of quantized Chern number, phase transition occurs at the interface between two PhCs leading to the highly localization of electric field at the domain wall. This is called the interface states with frequencies in the common gap region. How the electric field distribute at the domain wall depends on the interface structure. There are two possible zigzag interface structure. As can be seen

in Fig. B.5(b), interface type 1 is defined as big dielectric rods couple together at the interface. Interface type 2 is the structure where small dielectric rods couple together at the domain wall.

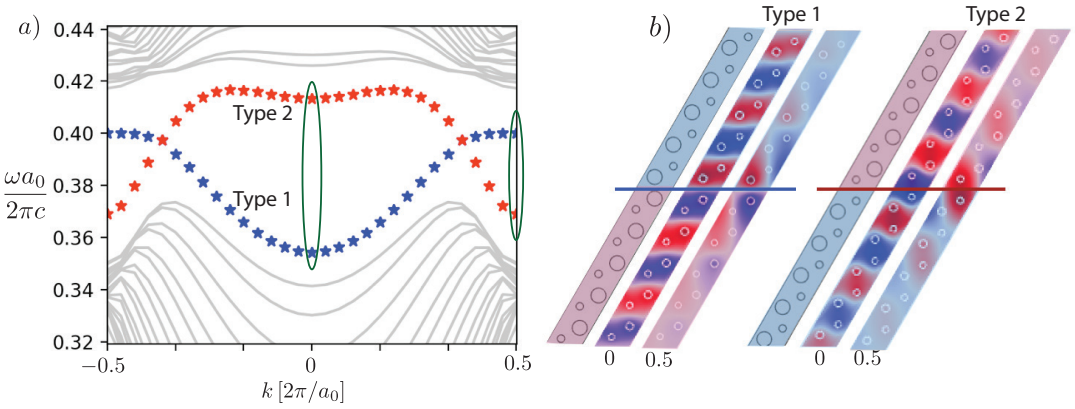

FIGURE B.5: (a) Bulk-edge correspondence around the first band gap of interface structure. The blue dot line is the interface states for the supercell structure where PhC1 is placed under PhC2 (interface type 1). The red dot line is the interface states for the supercell structure where PhC2 is placed under PhC1 (interface type 2). (b)Two interface structures and their corresponding field distribution at the middle and the edge of first BZ.

Figure B.5(a) shows bulk-edge correspondence of the supercell structure containing both PhC1 and PhC2 as indicated in Fig. B.5(b), which is calculated for zigzag edge. The structure is periodic in both $\boldsymbol{a_1}$ and $\boldsymbol{a_2}$ directions. Grey lines represent bulk states around the gap between the first and the second band. The blue dot line is the interface states for the interface structure type 1. On the other hand, the red dot line is the interface states for the interface structure type 2. Electric field is highly localized at the domain wall between two PhCs at $k = \frac{\pi}{a_0}$ and much more penetrate into the bulk at $k = 0$ as shown in Fig. B.5(b).While in the former case, electric field profile expresses as a node at the interface, the latter case's electric field profile manifests as an anti-node.

B.3 Topological Corner States

In Fig. B.5(b), we indicate that the interface is parallel to $\boldsymbol{a_1}$. If we rearrange the supercell structure as PhC1 or PhC2 is on the left side and the remaining PhC is on the right side, the interface becomes parallel to $\boldsymbol{a_2}$. The black bold lines in Fig. B.6 indicate the 1D first BZ in each direction. As can be seen in Fig. B.6(a), for the interface type 1, if we project all the k-points to the first BZ, at the side of negative k-value, valley K is projected (blue dot) leading to Chern number for this side is 1, while at opposite side, valley K' is projected (red dot) and the corresponding Chern number is -1. Similarly, if the interface is parallel to $\boldsymbol{a_2}$ axis, as shown in Fig. B.6(b), the projection of K (blue dot) and $K\prime$ points (red dot) are at positive and negative k value, respectively. Therefore, Chern number for the negative and positive side is -1 and 1, respectively. For interface type 2, the explanation is similar to for interface type 1.

The two interfaces in Fig. B.6 can formed two types of corner, which are 60° corner and 120° corner. For the 60° corner, two interfaces have opposite Chern number.

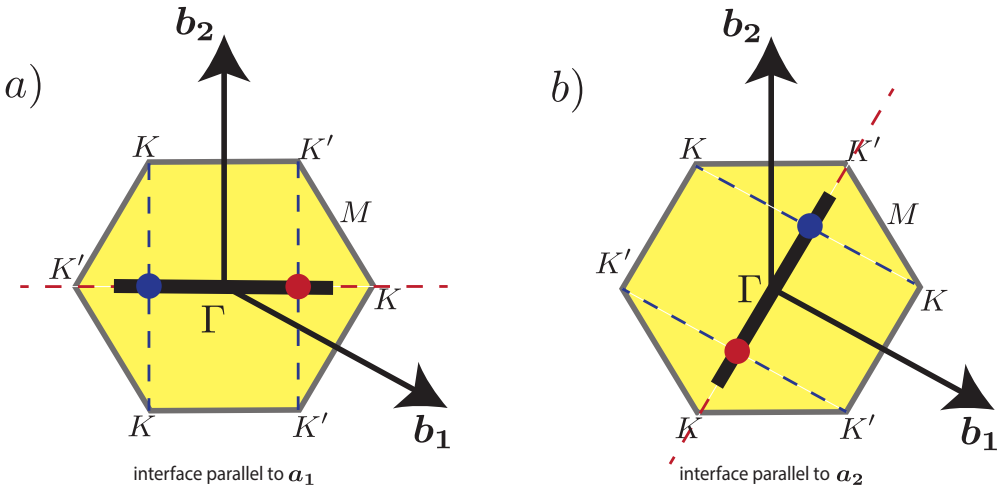

FIGURE B.6: If the common interface of two PhCs is parallel to a_i direction ($i = 1, 2$), the first BZ of the interface structure will parallel to a_i. (a) interface direction is parallel to a_1. (b) interface direction is parallel to a_2. In both (a) and (b), the 1D first BZ is described by black bold line, blue (red) dots indicate the projection of $K(K')$ points on to the first BZ.

For the 120° corner, two interface have the same Chern number. Because of the finite difference in Chern number between two interface, we expect the emergence of topological corner states in 60° corner.

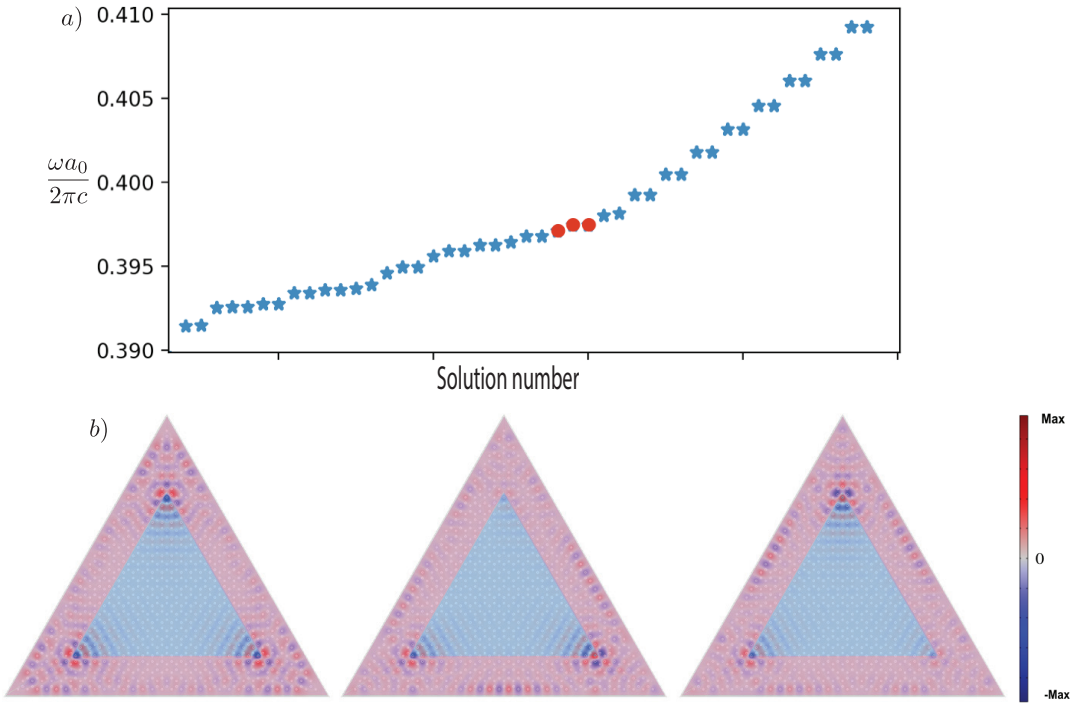

FIGURE B.7: (a) Frequency spectrum for the case of PhC2 surrounded by PhC1. The red dots indicate frequencies for corner states. (b) Field distribution in the three 60° corner states.

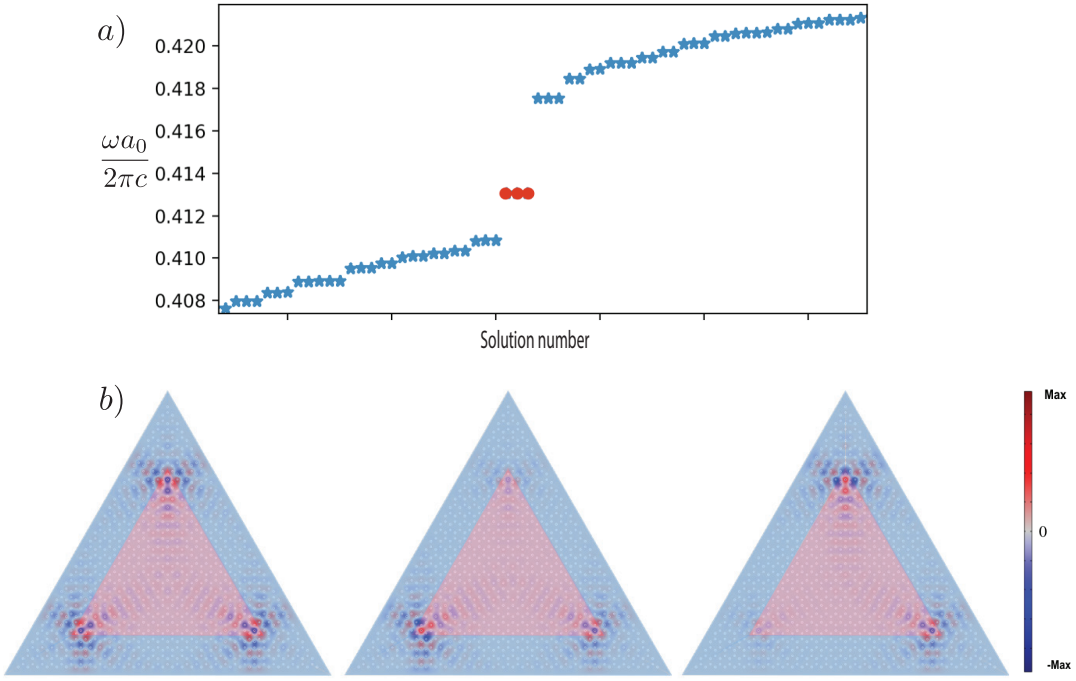

FIGURE B.8: (a) Frequency spectrum for the case of PhC1 surrounded by PhC2. The red dots indicate frequencies for corner states. (b) Field distribution in the three 60° corner states.

Here we propose a PhC structure where the triangular shape of PhC1 is surrounded by PhC2 and vice versa. These structure have three 60° corners and three common interfaces.

The two figures above are frequency spectrum and field profile for the corner states. Fig. B.7 shows the corner states for PhC structure where three type 1 interfaces form equilateral triangle. Three corner states were observed with their frequencies in the gap region. Electric field in each state is localized at the sub-lattice at the corner then decay exponentially. On the contrary, when PhC1 is surrounded by PhC2, the interface is type 2 as shown in Fig. B.8. The number of corner state is the same as the former case and their frequencies are also in the gap. However, electric field now is localized at the sub-lattice next to the corner then also exponentially decay.

We have numerically observed topological corner states at 60° corner for two types of structure. These states are useful for the confinement of EM wave.

References

[1] W. H. BRAGG. "X-rays and Crystals". In: *Nature* 90.2243 (1912), pp. 219–219. DOI: 10.1038/090219a0. URL: https://doi.org/10.1038/090219a0.

[2] William Henry Bragg and William Lawrence Bragg. "The reflection of X-rays by crystals". In: *Proceedings of the Royal Society of London. Series A, Containing Papers of a Mathematical and Physical Character* 88.605 (1913), pp. 428–438. DOI: 10.1098/rspa.1913.0040. eprint: https://royalsocietypublishing.org/doi/pdf/10.1098/rspa.1913.0040. URL: https://royalsocietypublishing.org/doi/abs/10.1098/rspa.1913.0040.

[3] Eli Yablonovitch. "Inhibited Spontaneous Emission in Solid-State Physics and Electronics". In: *Phys. Rev. Lett.* 58 (20 May 1987), pp. 2059–2062. DOI: 10.1103/PhysRevLett.58.2059. URL: https://link.aps.org/doi/10.1103/PhysRevLett.58.2059.

[4] Sajeev John. "Strong localization of photons in certain disordered dielectric superlattices". In: *Phys. Rev. Lett.* 58 (23 June 1987), pp. 2486–2489. DOI: 10.1103/PhysRevLett.58.2486. URL: https://link.aps.org/doi/10.1103/PhysRevLett.58.2486.

[5] J.D. Joannopoulos et al. *Photonic Crystals: Molding the Flow of Light (Second Edition)*. Princeton University Press, 2011. ISBN: 9781400828241. URL: https://books.google.co.jp/books?id=QrTNslcjlZEC.

[6] Lord Rayleigh Sec. R. S. "XVII. On the maintenance of vibrations by forces of double frequency, and on the propagation of waves through a medium endowed with a periodic structure". In: *The London, Edinburgh, and Dublin Philosophical Magazine and Journal of Science* 24.147 (1887), pp. 145–159. DOI: 10.1080/14786448708628074. eprint: https://doi.org/10.1080/14786448708628074. URL: https://doi.org/10.1080/14786448708628074.

[7] E. Yablonovitch, T. J. Gmitter, and K. M. Leung. "Photonic band structure: The face-centered-cubic case employing nonspherical atoms". In: *Phys. Rev. Lett.* 67 (17 Oct. 1991), pp. 2295–2298. DOI: 10.1103/PhysRevLett.67.2295. URL: https://link.aps.org/doi/10.1103/PhysRevLett.67.2295.

[8] N. David Mermin Neil W. Ashcroft. *Solid State Physics*. New York: Holt, Rinehart and Winston, 1976. ISBN: 978-0-03-083993-1. URL: https://books.google.co.jp/books/about/Solid_State_Physics.html?id=1C9HAQAAIAAJ&redir_esc=y.

[9] John David Jackson. *Classical Electrodynamics, 3rd edition*. New York: Wiley, 1998. ISBN: 978-0-471-30932-1. URL: https://books.google.co.jp/books/about/Classical_Electrodynamics.html?id=FOBBEAAAQBAJ&redir_esc=y.

[10] Felix Bloch. "Über die Quantenmechanik der Elektronen in Kristallgittern". In: *Zeitschrift für Physik* 52.7 (1929), pp. 555–600. DOI: 10.1007/BF01339455. URL: https://doi.org/10.1007/BF01339455.

[11] COMSOL, Inc. *COMSOL Multiphysics*. Version version 6.1. URL: www.comsol.com.

[12] Steven G. Johnson and J. D. Joannopoulos. "Block-iterative frequency-domain methods for Maxwell's equations in a planewave basis". In: *Opt. Express* 8.3 (2001), pp. 173–190. URL: http://www.opticsexpress.org/abstract.cfm?URI=OPEX-8-3-173.

[13] N.F. Mott and H. Jones. *The theory of the properties of metals and alloys. 2nd edition*. Oxford University Press, 1958.

[14] A. Bansil, Hsin Lin, and Tanmoy Das. "*Colloquium* : Topological band theory". In: *Rev. Mod. Phys.* 88 (2 June 2016), p. 021004. DOI: 10.1103/RevModPhys.88.021004. URL: http://link.aps.org/doi/10.1103/RevModPhys.88.021004.

[15] M. Z. Hasan and C. L. Kane. "*Colloquium* : Topological insulators". In: *Rev. Mod. Phys.* 82 (4 Nov. 2010), pp. 3045–3067. DOI: 10.1103/RevModPhys.82.3045. URL: http://link.aps.org/doi/10.1103/RevModPhys.82.3045.

[16] Xiao-Liang Qi and Shou-Cheng Zhang. "Topological insulators and superconductors". In: *Rev. Mod. Phys.* 83 (4 Oct. 2011), pp. 1057–1110. DOI: 10.1103/RevModPhys.83.1057. URL: http://link.aps.org/doi/10.1103/RevModPhys.83.1057.

[17] Yoichi Ando. "Topological Insulator Materials". In: *Journal of the Physical Society of Japan* 82.10 (2013), p. 102001. DOI: 10.7566/JPSJ.82.102001. eprint: https://doi.org/10.7566/JPSJ.82.102001. URL: https://doi.org/10.7566/JPSJ.82.102001.

[18] S. Raghu and F. D. M. Haldane. "Analogs of quantum-Hall-effect edge states in photonic crystals". In: *Phys. Rev. A* 78 (3 Sept. 2008), p. 033834. DOI: 10.1103/PhysRevA.78.033834. URL: https://link.aps.org/doi/10.1103/PhysRevA.78.033834.

[19] Zheng Wang et al. "Reflection-free one-way edge modes in a gyromagnetic photonic crystal." In: *Phys. Rev. Lett.* 100.1 (Jan. 2008), p. 013905. ISSN: 0031-9007. DOI: 10.1103/PhysRevLett.100.013905. URL: http://journals.aps.org/prl/abstract/10.1103/PhysRevLett.100.013905.

[20] Zheng Wang et al. "Observation of unidirectional backscattering-immune topological electromagnetic states." In: *Nature* 461.7265 (Oct. 2009), pp. 772–5. ISSN: 1476-4687. DOI: 10.1038/nature08293. URL: http://dx.doi.org/10.1038/nature08293.

[21] Mohammad Hafezi et al. "Robust optical delay lines with topological protection". In: *Nature Phys.* 7.11 (Aug. 2011), pp. 907–912. ISSN: 1745-2473. DOI: 10.1038/nphys2063. URL: http://dx.doi.org/10.1038/nphys2063.

[22] Alexander B Khanikaev et al. "Photonic topological insulators." In: *Nature Mater.* 12.3 (Mar. 2013), pp. 233–9. ISSN: 1476-1122. DOI: 10.1038/nmat3520. URL: http://dx.doi.org/10.1038/nmat3520.

[23] Scott A. Skirlo, Ling Lu, and Marin Soljačić. "Multimode One-Way Waveguides of Large Chern Numbers". In: *Phys. Rev. Lett.* 113.11 (Sept. 2014), p. 113904. ISSN: 0031-9007. DOI: 10.1103/PhysRevLett.113.113904. URL: http://journals.aps.org/prl/abstract/10.1103/PhysRevLett.113.113904.

[24] Mikael C. Rechtsman et al. "Photonic Floquet topological insulators". In: *Nature* 496.7444 (Apr. 2013), pp. 196–200. ISSN: 0028-0836. URL: http://dx.doi.org/10.1038/nature12066.

[25] M. Hafezi et al. "Imaging topological edge states in silicon photonics". In: *Nature Photon.* 7.12 (Oct. 2013), pp. 1001–1005. ISSN: 1749-4885. DOI: 10.1038/nphoton.2013.274. URL: http://dx.doi.org/10.1038/nphoton.2013.274.

[26] J. Zak. "Berry's phase for energy bands in solids". In: *Phys. Rev. Lett.* 62 (23 June 1989), pp. 2747–2750. DOI: 10.1103/PhysRevLett.62.2747. URL: http://link.aps.org/doi/10.1103/PhysRevLett.62.2747.

[27] P. Delplace, D. Ullmo, and G. Montambaux. "Zak phase and the existence of edge states in graphene". In: *Phys. Rev. B* 84 (19 Nov. 2011), p. 195452. DOI: 10.1103/PhysRevB.84.195452. URL: https://link.aps.org/doi/10.1103/PhysRevB.84.195452.

[28] Yasutomo Ota et al. "Photonic crystal nanocavity based on a topological corner state". In: *Optica* 6.6 (June 2019), pp. 786–789. DOI: 10.1364/OPTICA.6.000786. URL: http://www.osapublishing.org/optica/abstract.cfm?URI=optica-6-6-786.

[29] Feng Liu, Hai-Yao Deng, and Katsunori Wakabayashi. "Topological photonic crystals with zero Berry curvature". In: *Phys. Rev. B* 97 (3 Jan. 2018), p. 035442. DOI: 10.1103/PhysRevB.97.035442. URL: https://link.aps.org/doi/10.1103/PhysRevB.97.035442.

[30] Feng Liu, Hai-Yao Deng, and Katsunori Wakabayashi. "Helical Topological Edge States in a Quadrupole Phase". In: *Phys. Rev. Lett.* 122 (8 Mar. 2019), p. 086804. DOI: 10.1103/PhysRevLett.122.086804. URL: https://link.aps.org/doi/10.1103/PhysRevLett.122.086804.

[31] Shiing-shen Chern. "Characteristic Classes of Hermitian Manifolds". In: *Annals of Mathematics* 47.1 (1946), pp. 85–121. ISSN: 0003486X. URL: http://www.jstor.org/stable/1969037.

[32] D. J. Thouless et al. "Quantized Hall Conductance in a Two-Dimensional Periodic Potential". In: *Phys. Rev. Lett.* 49 (6 Aug. 1982), pp. 405–408. DOI: 10.1103/PhysRevLett.49.405. URL: http://link.aps.org/doi/10.1103/PhysRevLett.49.405.

[33] Xiao-Dong Chen et al. "Valley-contrasting physics in all-dielectric photonic crystals: Orbital angular momentum and topological propagation". In: *Phys. Rev. B* 96 (2 July 2017), p. 020202. DOI: 10.1103/PhysRevB.96.020202. URL: https://link.aps.org/doi/10.1103/PhysRevB.96.020202.

[34] Huyen Thanh Phan, Feng Liu, and Katsunori Wakabayashi. "Valley-dependent corner states in honeycomb photonic crystals without inversion symmetry". In: *Opt. Express* 29.12 (June 2021), pp. 18277–18290. DOI: 10.1364/OE.427222. URL: http://opg.optica.org/oe/abstract.cfm?URI=oe-29-12-18277.

[35] Qitang Fan et al. "Biphenylene network: A nonbenzenoid carbon allotrope." eng. In: *Science* 372.6544 (May 2021), pp. 852–856. ISSN: 1095-9203 (Electronic); 0036-8075 (Linking). DOI: 10.1126/science.abg4509.

[36] A Bafekry et al. "Biphenylene monolayer as a two-dimensional nonbenzenoid carbon allotrope: a first-principles study". In: *Journal of Physics: Condensed Matter* 34.1 (Oct. 2021), p. 015001. DOI: 10.1088/1361-648x/ac2a7b. URL: https://doi.org/10.1088/1361-648x/ac2a7b.

[37] Barry Bradlyn and Mikel Iraola. "Lecture notes on Berry phases and topology". In: *SciPost Phys. Lect. Notes* (2022), p. 51. DOI: 10.21468/SciPostPhysLectNotes.51. URL: https://scipost.org/10.21468/SciPostPhysLectNotes.51.